

Comprehensive Characterization of Palygorskite from Torrejón el Rubio (Spain) Based on Experimental Techniques and Theoretical DFT Studies

A. M. Fernández
V. Timón
J.J. Cubero
D.M. Sánchez-Ledesma
L. Gutiérrez-Nebot
J.J. Martínez
C. Romero
M. Labajo
A. Melón
I. Barrios



Comprehensive Characterization of Palygorskite from Torrejón el Rubio (Spain) Based on Experimental Techniques and Theoretical DFT Studies

A. M. Fernández^a

V. Timón^b

J.J. Cubero^c

D.M. Sánchez-Ledesma^a

L. Gutiérrez-Nebot^a

J.J. Martínez^a

C. Romero^a

M. Labajo^a

A. Melón^a

I. Barrios^a

^a CIEMAT, Avda. Complutense 22, 28040, Madrid, Spain

^b Instituto de Estructura de la Materia, Serrano 123, 28006 Madrid, Spain

^c Departamento de Minas, Junta de Extremadura, Spain

Departamento de Medio Ambiente

Toda correspondencia en relación con este trabajo debe dirigirse al Servicio de Información y Documentación, Centro de Investigaciones Energéticas, Medioambientales y Tecnológicas, Ciudad Universitaria, 28040-MADRID, ESPAÑA.

Las solicitudes de ejemplares deben dirigirse a este mismo Servicio.

Los descriptores se han seleccionado del Thesaurus del DOE para describir las materias que contiene este informe con vistas a su recuperación. La catalogación se ha hecho utilizando el documento DOE/TIC-4602 (Rev. 1) Descriptive Cataloguing On-Line, y la clasificación de acuerdo con el documento DOE/TIC.4584-R7 Subject Categories and Scope publicados por el Office of Scientific and Technical Information del Departamento de Energía de los Estados Unidos.

Se autoriza la reproducción de los resúmenes analíticos que aparecen en esta publicación.

Catálogo general de publicaciones oficiales
<http://www.060.es>

Depósito Legal: M -26385-2011

ISSN: 1135 - 9420

NIPO: 721-13-040-7

Editorial CIEMAT

CLASIFICACIÓN DOE Y DESCRIPTORES

S58

PHYSICAL PROPERTIES, CHEMICAL PROPERTIES, CLAYS, MINERALS,
GEOCHEMICAL SURVEYS, SPAIN

Comprehensive Characterization of Palygorskite from Torrejón el Rubio (Spain) Based on Experimental Techniques and Theoretical DFT Studies

Fernández, A. M.; Timón, V.; Cubero, J.J.; Sánchez-Ledesma, D.M.; Gutiérrez-Nebot, L.; Martínez, J.J.; Romero, C.; Labajo, M.; Melón, A.; Barrios, I.

74 pp., 27 figs., 135 refs.

Abstract:

New data about the physico-chemical, microstructural and crystal-chemical properties of the mineral palygorskite from Torrejón el Rubio (Cáceres, Spain) were obtained by a combination of experimental techniques (XRD, FRX, FTIR, TG-DSC, SEM and chemical analyses), as well as geometry optimization by means of the Density Functional Theory (DFT).

This study demonstrates the applicability of the mixed theoretical-experimental work to characterize and understand the properties of clay minerals used in technological applications and environmental remediation.

Caracterización Exhaustiva de la Palygorskita de Torrejón el Rubio (Spain) Basada en Técnicas Experimentales y Estudios teóricos DFT

Fernández, A. M.; Timón, V.; Cubero, J.J.; Sánchez-Ledesma, D.M.; Gutiérrez-Nebot, L.; Martínez, J.J.; Romero, C.; Labajo, M.; Melón, A.; Barrios, I.

74 pp., 27 figs., 135 refs.

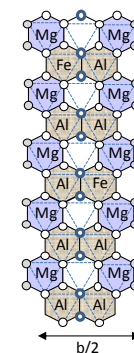
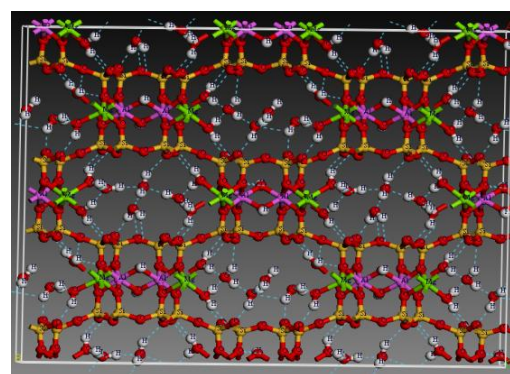
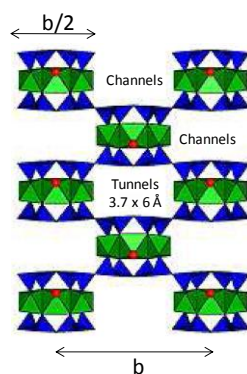
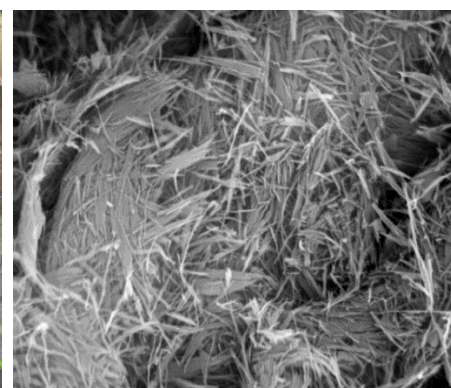
Resumen:

Se han obtenido nuevos datos sobre las propiedades fisico-químicas, microestructurales y cristal-químicas del mineral palygorskita de Torrejón el Rubio (Cáceres, Spain) mediante una combinación de técnicas experimentales (XRD, FRX, FTIR, TG-DSC, SEM y análisis químico), así como mediante la optimización geométrica por la Teoría de Densidad Funcional (DFT).

Este estudio demuestra la aplicabilidad de la combinación del trabajo experimental y teórico para caracterizar y entender las propiedades de los minerales de la arcilla utilizados en aplicaciones tecnológicas y remediación medioambiental.

Comprehensive characterization of palygorskite from Torrejón el Rubio (Spain) based on experimental techniques and theoretical DFT studies

A. M. Fernández
V. Timón
J.J. Cubero
D.M. Sánchez-Ledesma
L. Gutierrez-Nebot
J.J. Martínez
C. Romero
M. Labajo
A. Melón
I. Barrios



**COMPREHENSIVE CHARACTERIZATION OF
PALYGORSKITE FROM TORREJÓN EL RUBIO (SPAIN)
BASED ON EXPERIMENTAL TECHNIQUES
AND THEORETICAL DFT STUDIES**

A. M. Fernández^a, V. Timón^b, J.J. Cubero^c, D.M. Sánchez-Ledesma^a, L. Gutierrez-Nebot^a,
J.J. Martínez^a, C. Romero^a, M. Labajo^a, A. Melón^a, I. Barrios^a

^a CIEMAT, Avda. Complutense 22, 28040, Madrid, Spain

^b Instituto de Estructura de la Materia, Serrano 123, 28006 Madrid, Spain

^c Departamento de Minas, Junta de Extremadura, Spain

**Informe preparado en el contexto de la
Jornada Científica de la Sociedad Española de Arcillas (SEA)
en memoria del Profesor Jose María Serratorra (15 noviembre 2013)**

Departamento de Medio Ambiente

Table of Contents

1	Introduction	13
2	Materials.....	24
2.1	Geological setting.....	24
2.2	Palygorskite sample selection	28
3	Methodology	29
3.1	Experimental methodology	29
3.2	Crystal simulation methodology: Density Functional Theory (DFT)	32
4	Results and Discussion.....	33
4.1	Physico-Chemical Characterization and Textural properties	33
4.2	Mineralogical analysis and Crystallographic structure by XRD	40
4.3	Microstructural Analysis (SEM analyses).....	43
4.4	Chemical analysis by FRX and SEM-EDAX analysis.....	43
4.5	Thermal and calorimetric analysis.....	48
4.6	Octahedral sheet composition by FTIR analysis	53
4.7	Crystal unit cell structural DFT simulations and X-Ray powder patterns analysis.....	58
4.8	Infrared spectra: Theoretical analysis of the vibrational modes.....	62
5	Conclusions	65
6	Acknowledgments.....	67
7	References	69

LIST OF TABLES

Table 1. Mineralogical composition and physico-chemical properties of the palygorskite from La Cierva deposit (Torrejón el Rubio, Cáceres)

Table 2. Parameters deduced from BET and t-plot treatment on the adsorption of N₂ at 77K

Table 3. Chemical composition of palygorskite from Torrejón el Rubio (Cáceres) obtained by FRX and SEM-EDX analyses and their comparison with other data obtained in the literature

Table 4. Structural formulae of palygorskite samples from Torrejón el Rubio (Cáceres) obtained by FRX and SEM-EDX analyses and their comparison with other data obtained in the literature

Table 5. Water losses (%) of the Palygorskite from Torrejón el Rubio (Cáceres) compared with those from Attapulgi (USA) and an ideal palygorskite

Table 6. Temperature ranges for the types of water in the Palygorskite from Torrejón el Rubio (Cáceres)

Table 7. Theoretical crystal parameters for all the hydrated and non-hydrated palygorskite systems analysed

Table 8. Comparison of the theoretical and experimental intensities in each hkl atomic planes (in Å)

Table 9. Summary of the theoretical and experimental mid-infrared assignments

LIST OF FIGURES

Figure 1. Schematic representation of various structures. T: Tetrahedral sheet, M: Octahedral sheet, O_a: apical oxygens, O_b: basal oxygens, O_{oct}: octahedral anionic position (OH⁻, F⁻, Cl⁻, O²⁻) and not shared with the tetrahedral. In 1:1 layer structure the unit cell includes six octahedral sites (four cis- and two trans-oriented octahedral) and four tetrahedral sites. In 2:1 layer structure the unit cell includes six octahedral sites and eight tetrahedral sites (after Brigatti et al., 2006)

Figure 2. a) Trioctahedral sheet, b) dioctahedral sheet, and c) trans- and cis- octahedral sites in structures of 2:1 dioctahedral phyllosilicates. O_a represents the apical oxygen atoms shared with tetrahedral, O_{oct} is the anionic site shared between the adjacent octahedral, and a and b are unit-cell parameters (Brigatti et al., 2006; Meunier, 2005)

Figure 3. Trans-vacant (tv: opposite site) and cis-vacant (cv: same site) octahedral sites in structures of 2:1 dioctahedral phyllosilicates

Figure 4. a) Structure of the palygorskite from Bradley (1940) projected in the [001] plane: 2[(OH)₂ (Mg, Al, Fe)₅(OH)₂ Si₈O₂₀] 4H₂O. Monoclinic a₀ sin β = 12.9 Å, b₀ = 18.0 Å, c₀ = 5.2 Å (after Haden and Schwint, 1967); b) Configuration of the octahedral ribbons in the palygorskite structure having M1, M2, and M3 octahedral sites. The a-axis of palygorskites corresponds to c-axis of the micas (from Güven et al., 1992)

Figure 5. Schematic representation of palygorskite structure: a) Modular structure of palygorskite along the c-axis and overview of polysomes (2:1 TOT ribbons), channels and tunnels, b) overview of fibrous morphology, the presence of channels and the formation of discontinuous ribbons, c) projection on (001) plane (c-axis), d) projection on 010 plane showing an octahedral ribbon with the M1, M2 and M3 sites as well as structural hydroxyls, coordinated and zeolitic water (after Suárez and Garcia-Romero, 2006; and Krekeler and Guggenheim, 2008)

Figure 6. a) Folded structure after heating the palygorskite viewed along the monoclinic c-axis [001] (from Post and Heaney, 2008), b) Sepiolite anhydride (Serratos, 1979)

Figure 7. Development of optimal properties of palygorskites by thermal activation (heating) showed on a differential thermal (DTA) curve (Haden and Schiwint, 1967)

Figure 8. Schematic representation of the hierarchical distribution of pores in palygorskite from the intracrystalline and structural microporosity to the textural mesoporosity and macroporosity caused by the aggregation of bundles of fibres (after Suárez and García Romero, 2012)

Figure 9. Geographical and geological setting of the Talaván – Torrejón el Rubio Basin (after Galán and Pozo, 2011 and Fernández-Macarro and Blanco-Sánchez, 1990)

Figure 10. a) Geological map and correlation of cores from the Torrejón el Rubio Basin according to Galán and Castillo (1984); b) Schematic representation of Torrejón El Rubio palygorskite deposit (1: weathering substrate, 2: clayey sand sedimentation and early diagenetic (vadose) magnesium-rich attapulgite, probably related to sedimentation, 3: silting up sedimentation, 4: alluvial fan or “raña” deposits, 5: fluvial network trenching (Galán and Castillo, 1984)

Figure 11. a) La Cierva Palygorskite deposit from Torrejón el Rubio (Cáceres), b) Detail of the palygorskite sample collection

Figure 12. BET surface areas obtained from palygorskite samples as a function of temperature obtained at different experimental conditions (outgassing or drying temperature). After Serratos et al. (1979)

Figure 13. a) Nitrogen adsorption/desorption isotherms at 77 K on palygorskite sample from Torrejón El Rubio (Cáceres), and b) t-plot treatment of the adsorption branch

Figure 14. Pore size distribution obtained by the BJH method for macro- and mesopores and by the DFT method (Tarazona model) for micropores in palygorskite sample from Torrejón el Rubio (Cáceres)

Figure 15. Pore size distribution obtained by the DFT method for micropores in palygorskite sample from Torrejón el Rubio (Cáceres) according to the Cylinder Tarazona NLDFT and the Infinite Slit NLDFT models

Figure 16. XRD pattern of the raw clay mineral from La Cierva deposit (Torrejón el Rubio, Cáceres). (Pal: palygorskite, I/Mu: illite/muscovite, Cris: cristobalite, An: anorthite, Chl: chlorite, Qz: quartz, Cor: corundum, Ba: Barite)

Figure 17. XRD patterns of the < 2 µm clay mineral fraction (AO: orientated aggregate; EG: ethylene glycolated; 550°C: heated at 550°C) from palygorskite from Torrejón el Rubio (Cáceres). d_{hkl} reflexions of palygorskite are shown; Cr: cristobalite, Chl: chlorite, Mu: Illite/muscovite

Figure 18. Scanning electron micrograph showing aggregates of palygorskite fibres

Figure 19. Different schematic distributions of cations in the octahedral sheet of palygorskite from Torrejón el Rubio based on: ten half unit cells (1 and 2); 20 half units cells (3); or of five half unit cells (a, b and c) (projection on the (010) plane), the distributions 3) and a) being possibly the most energetically favorable. Idealized structural formula for distributions 1 and 2): $(\text{Mg}_{2.00}\text{Al}_{1.60}\text{Fe}^{3+}_{0.20}\text{Fe}^{2+}_{0.10}\text{Ti}_{0.10}\square_1)(\text{Si}_{7.90}\text{Al}_{0.10})\text{K}_{0.10}\text{O}_{21}$;

Figure 20. TG and DTG curves of palygorskite performed on the total and < 2 μm fractions

Figure 21. Differential Scanning calorimetric (DSC) curves of palygorskite performed on the total and < 2 μm fractions

Figure 22. NIR spectra of the palygorskite from Torrejón el Rubio (Cáceres) and its second derivative calculated with the Savitzky-Golay algorithm with 15-point smoothing

Figure 23. MIR spectra of the palygorskite from Torrejón el Rubio (Cáceres) and its second derivative calculated with the Savitzky-Golay algorithm with 15-point smoothing

Figure 24. Atomic hydrated and non-hydrated palygorskite optimized structure

Figure 25. Atomic hydrated Pw16 palygorskite optimized structure. A 2x2 supercell it is shown for clarity

Figure 26. X-ray diffraction patterns of palygorskite total fraction sample from Torrejón el Rubio (Cáceres) and the simulated one

Figure 27. Comparison of the mid-infrared experimental spectra of the palygorskite from Torrejón el Rubio (Cáceres) with the simulated one

COMPREHENSIVE CHARACTERIZATION OF PALYGORSKITE FROM TORREJÓN EL RUBIO (SPAIN) BASED ON EXPERIMENTAL TECHNIQUES AND THEORETICAL DFT STUDIES

Abstract

New data about the physico-chemical, microstructural and crystal-chemical properties of the mineral palygorskite from Torrejón el Rubio (Cáceres, Spain) were obtained by a combination of experimental techniques (XRD, FRX, FTIR, TG-DSC, SEM and chemical analyses), as well as geometry optimization by means of the Density Functional Theory (DFT).

This palygorskite has a dioctahedral character and can be defined as a Type II common palygorskite. The total amount of phyllosilicates in the bulk sample is 60 wt.%, being the clay mineral fraction composed by palygorskite (97 wt.%), muscovite/illite (2 wt.%) and chlorite (1 wt.%). The remaining minerals on the total fraction are quartz, cristobalite, K-feldspar, barite and ilmenite. No carbonates were found. The XRD patterns show that the mineral fits better to an orthorhombic structure and after unit cell refinements the calculated parameters were $a = 12.7763 \pm 0.0276 \text{ \AA}$, $b = 17.9211 \pm 0.0441 \text{ \AA}$ and $c = 5.2013 \pm 0.0161 \text{ \AA}$, with $\alpha = \beta = \gamma = 90^\circ$ and a volume cell of $1190.92 \pm 4.48 \text{ cm}^3$. These parameters that fit well with those calculated by DFT periodic planewave pseudopotential studies employed that are used to provide first-principles predictions of local structural relaxation, atomic ordering and site preference of water molecules inside the palygorskite channels. According to FTIR and chemical formula calculations, Mg^{2+} atoms at octahedral sites are substituted by Al, Fe and Ti; and silica at tetrahedral sheets is substituted by $^{\text{IV}}\text{Al}$. The excess of negative charge on both sheets is compensated by K, Ca and Na interlayer cations: from +0.05 to +0.14 e/hfuc, which correspond to a CEC between 7 and 20 meq/100g depending on the average tetrahedral substitutions. For the five octahedral positions per half unit cell (phuc), one octahedral site is vacant and 1.56-1.60 is occupied by $^{\text{VI}}\text{Al}$. The half unit cell formula for its dehydrated form determined on the basis of 21 oxygens is $(\text{Mg}_{2.00}\text{Al}_{1.57}\text{Fe}^{3+}_{0.39}\text{Ti}_{0.04}\square_1)(\text{Si}_{7.90}\text{Al}_{0.10})\text{K}_{0.14}\text{O}_{21}$. Inside the octahedral sheet, the inner M1 sites are occupied by vacants, whereas the M2 sites are occupied at 98% by trivalent cations (78.5% Al^{3+} and 19.5% Fe^{3+}) and at 2.0% by tetravalent cations Ti^{4+} , all of them linked to structural 2.0 structural hydroxyls. The two remaining Mg^{2+} per hfuc occupy edge M3 sites and are coordinated to 2.0 molecules of OH_2 . Channels of this palygorskite are deficient in zeolitic H_2O since they contain only 1.69 water molecules. The R^3/R^2 ratio is around 1.01 (Al/Mg ratio of 0.83) indicating the pronounced dioctahedral character, which was confirmed by

the well-resolved FTIR bands of AlAlOH, FeFeOH and AlFeOH in the MIR and NIR ranges. No signals of Mg₃OH and Si-OH (silanol groups) characteristics of a trioctahedral character and of broken edge surfaces at tetrahedral sheets, respectively, were found in the spectra. The TG-DSC curves show that zeolitic water is lost up to 114°C and the hydroxyl water at M2 sites is lost between 468 and 568°C. The coordinated water at M3 sites is liberated in two different stages: one half of coordinated water is lost from 114 to 235°C and the second half of coordinated water between 235 and 468°C, this latter water being vanished slower due to the hindrance of the folded channels on the diffusion process. 0.3 water molecules are lost between 600 to 900°C due to the elimination of water from Si-OH generated during the thermal treatment in the TG-DSC test. The microstructural and textural properties of the palygorskite were also determined. Palygorskite samples show a fibrous morphology (SEM analysis) with a variable size ranging from 1 to 10 µm length and 10 to 250 nm thick, fibers occurring as bundles of rods or as aggregates displaying a meso- and macroporous bird-nest texture. The total surface area of this palygorskite is around 250-350 m²/g, determined both by water adsorption and nitrogen adsorption/desorption isotherms. The textural porosity of this fibrous material is composed by an interfiber microporosity, mesoporosity and macroporosity (calculated from BJH and DFT methods). The main surface area (around 212 m²/g) is developed in the structural or intracrystalline microporosity, which was determined from the microporous Tarazona NLDFT model. The study of the lowest relative pressures (microporous range) was necessary to analyse the adsorption properties of the crystallographic structure and inside the channels of the palygorskites. The external specific surface area developed on surfaces and edges (textural porosity) is between 77 and 104 m²/g.

The data were used to simulate the crystalline structure, calculating the local geometry optimization by means of the Density Functional Theory (DFT) in the Local Density Approximation (LDA) using the gradient corrected LDA developed by Perdew and Wang (GGA). The preliminary simulated structure was compared with the experimental DRX and FTIR spectra and a good agreement was obtained. Modifications on the structure considering a higher amount of unit cells (supercells) and elemental atom changes (Si, Mg, Al, Fe³⁺, Fe²⁺, Ti, etc.) in the octahedral sites should be considered in future works to analyse the most energetic stable configurations. In any case, this study demonstrates the applicability of the mixed theoretical-experimental work to characterize and understand the properties of clay minerals used in technological applications and environmental remediation.

Keywords: Palygorskite, FTIR, TG-DSC, DRX, FRX, SEM, DFT simulations

COMPREHENSIVE CHARACTERIZATION OF PALYGORSKITE FROM TORREJÓN EL RUBIO (SPAIN) BASED ON EXPERIMENTAL TECHNIQUES AND THEORETICAL DFT STUDIES

1 Introduction

Clays have been and continue to be one of the more important industrial raw material, widely used for different technological applications: industrial procedures, catalysts, agriculture, engineering and construction, environmental remediations, geology, etc. (Murray, 2000). Among the most important clay minerals, palygorskites are of interest since decades because of their sorptive, optical, colloidal-rheological and catalytic physico-chemical properties which are based on the fabric, large surface area, microporosity, crystal morphology, fibrous structure and composition (Serratos, 1979; Jones and Galán, 1988; Singer, 1989; Galán, 1996; Rhouta et al., 2013). Palygorskites has been mined for centuries because of its many useful properties and boast more than 100 commercial uses today in the pharmaceutical, fertilizer and pesticide industries (Jones and Galán, 1988; Alvarez et al., 2011; López Galindo et al., 2011; Neaman and Singer, 2011; Ruiz-Hitzky et al., 2011), being employed in paints, adhesives, sealants, bleaching agents, cosmetics, drilling muds (because of its small thixotropic effect), environmental absorbents (chemical and toxic wastes), fertilizer suspensions, catalyst for cracking soils, flexiographic inks, oil-spill and grease cleanup material, etc.

Palygorskite (or attapulgit) is a hydrous aluminum magnesium 2:1 layer silicate clay mineral with a fibrous morphology that typically occurs as fine-grained, poorly crystalline masses. It is found in a wide variety of geological environments (sediments and soils), commonly as felted masses or sheets referred to as mountain leather (Heddle, 1879). However, currently commercial deposits of palygorskite are rare and inhomogeneously distributed, except in arid-climate soils and lacustrine or lagoonal deposits that are hardly older than of Miocene age (25 Ma). The annual world production of palygorskite was estimated to be about 1,300,000 tons, the largest producer being the Unites States (76 % of the world production). Other producers are Guatemala, Senegal, Spain, Greece, Ukraine, Russia, India, China, Queensland and Australia (Murray et al., 2011). From historical and cultural point of view, palygorskite was known by ancient civilizations to manufacture the prominent and mysterious hybrid pigment, called Maya Blue (Van Olphen, 1966; Yacamán et al., 1996; Doménech et al., 2009; Sánchez del Rio et al., 2011).

According to Martín-Vivaldi and Hach-Ali (1970) and Jones and Galán (1988), the name palygorskite was first used by von Ssaftschenkow in 1862, from the name of the mining locality

in the Urals where it was first found, Palygorsk (Russia), but the mineral appears to have been known since the time of Theophrastus, 314 BC (Robertson, 1963); and has been variously called mountain-cork, mountain-leather and mountain-paper, pilolite (Heddle, 1879), lassalite (Friedel, 1901). The group was originally defined by Fersmann (1913), which applied the name palygorskite to a family of fibrous hydrous silicate minerals forming an isomorphous series between two end-members: an aluminum form (called paramontmorillonite), and a magnesium form (called pilolite). The name attapulgite was given by De Lapparent (1935) to a fibrous clay mineral found in Fuller's earths[®] of Attapulgius (large clay mineral deposits of Miocene age formed from the alteration of volcanic tuffs in Georgia and Florida, USA); and in *Terre à foulon* of Mormoiron (France) of alluvial origin. He suggested that attapulgite had the same structure as the fibrous mineral from Palygorsk (Ural, Russia), as described by von Ssaftschenkow (1862) and Fersmann (1913). The name attapulgite, as well as the group name *Hormites* (from the Greek hormathos: chain) formed by sepiolites and palygorskites, were discredited (Bailey et al., 1971), although both names are still commonly used due to the clays from USA have been widely commercialized. Other trade mark names for palygorskite are florindum, florex and florigel, astrangitegel (Russia), Smectagel (Spain), etc.

Regarding its origin and formation, palygorskites occur in sedimentary environments and arid and semiarid soils. Palygorskite is an authigenic clay mineral generally formed in marine, lacustrine-palustrine or edaphic environments. Most references about the distribution and genesis of palygorskite is in association with palaeosols and carbonate crusts (e.g., Galán and Singer, 2011; Leguey et al., 1984; Huertas et al., 1970). The origin of these high-magnesium clays is attributed to: a) hydrothermal activity by alteration of volcanic ash, b) structural transformation of smectite clays, or c) direct crystallization (neo-formation) from lateritic weathering in shallow, marginal seas or lagoons.

The stability diagram and the best conditions favourable to the formation of palygorskite require a particular alkaline medium, either after input by fluids or by degradation of other precursor minerals (mainly phyllosilicates): a high pH (from 9 to 11), high concentration of silica and magnesium, as well as a low aluminium activities in the solutions (Isphording, 1973; Singer and Norrish, 1974, Weaver and Beck, 1977; Singer, 1979). As long as aluminium (and iron) is abundant, it constrains the neoformation conditions towards montmorillonite. When alumina decreases, montmorillonite is replaced by palygorskite. Shallow water and higher than normal temperature might increase the pH (due to photosynthesis) and, consequently the silica solubility and supply, that with Mg is necessary for palygorskite formation (Milot, 1970). On the other hand, attapulgite has not been yet synthesized in laboratory (Martín Vivaldi and Linares, 1962; Mumpton and Roy, 1956).

With respect to the crystal structure, the atomic structure of the clay minerals consists of two basic units, a tetrahedral sheet and an octahedral sheet. In the silica tetrahedral layer silicon atom is equidistant from four oxygens or possibly hydroxyls arranged in the form of a tetrahedron with the silicon atom in the center. These tetrahedrons are arranged to form a hexagonal network repeated infinitively in two horizontal directions to form what is called the tetrahedral sheet (Figure 1). The octahedral sheet is comprised of closely packed oxygens and hydroxyls in which aluminum, iron and magnesium atoms are arranged in octahedral coordination. When Al^{3+} is the cation present in the octahedral sheet, only two-thirds of the possible positions are filled in order to balance the charges, the mineral being termed dioctahedral. When Mg^{2+} is present, all three positions are filled to balance the structure and the mineral is termed trioctahedral (Figure 2).

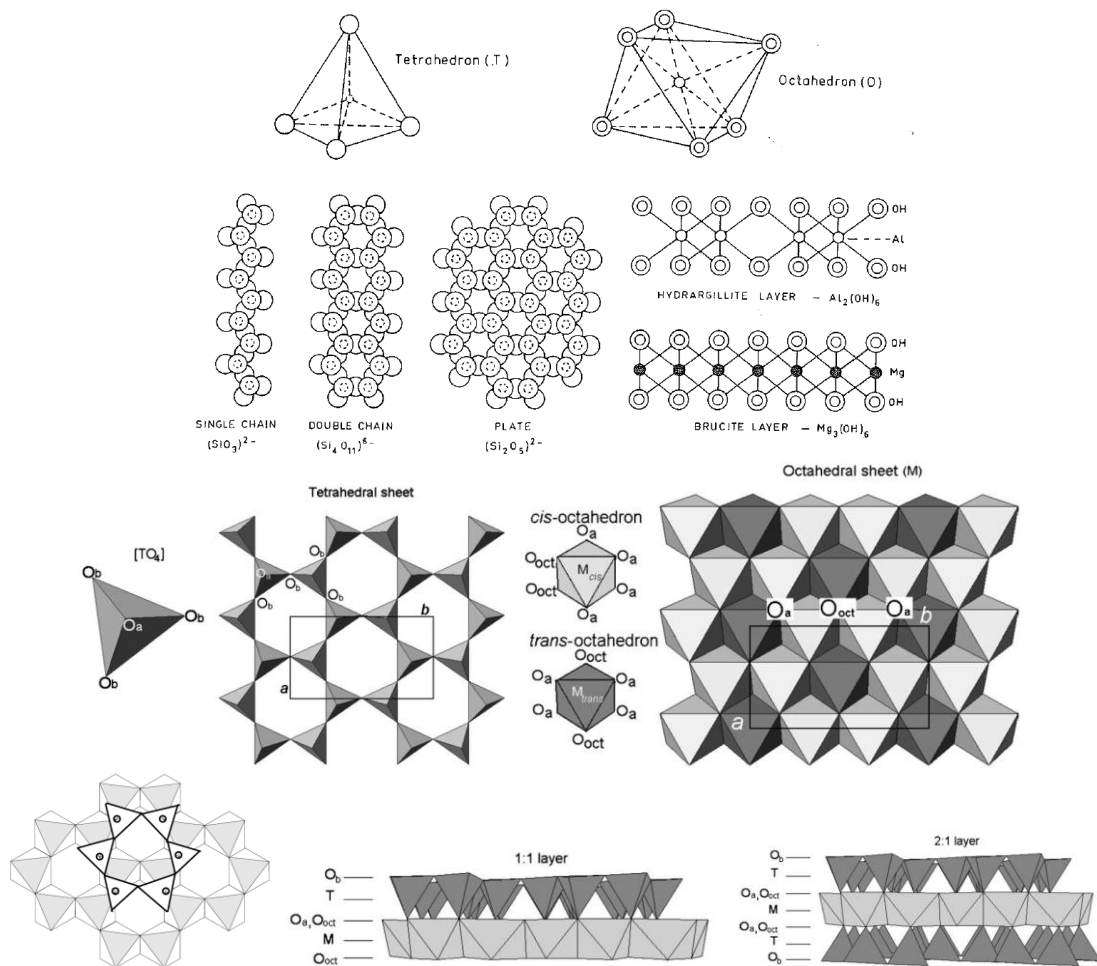


Figure 1. Schematic representation of various structures. T: Tetrahedral sheet, M: Octahedral sheet, O_a : apical oxygens, O_b : basal oxygens, O_{oct} : octahedral anionic position (OH^- , F^- , Cl^- , O^{2-}) and not shared with the tetrahedral. In 1:1 layer structure the unit cell includes six octahedral sites (four cis- and two trans-oriented octahedral) and four tetrahedral sites. In 2:1 layer structure the unit cell includes six octahedral sites and eight tetrahedral sites (after Brigatti et al., 2006)

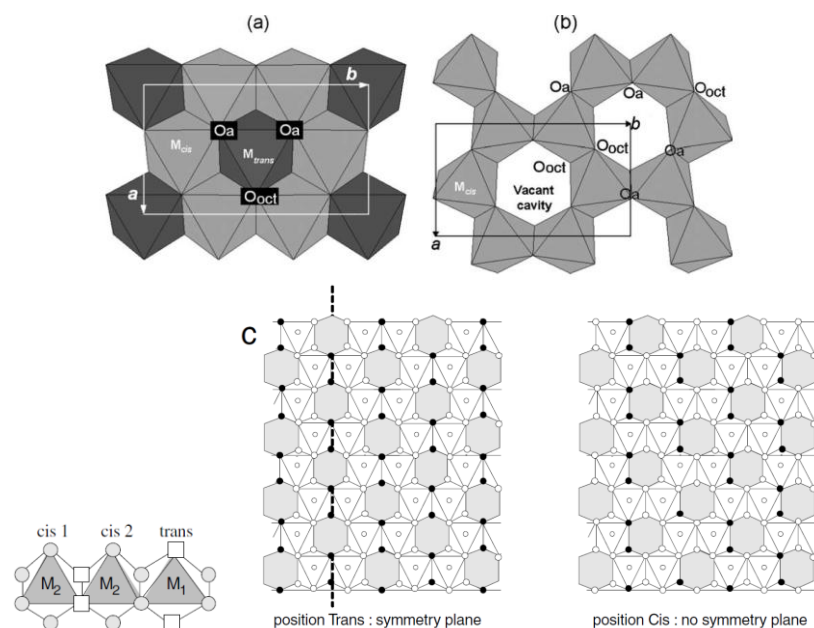


Figure 2. a) Trioctahedral sheet, b) dioctahedral sheet, and c) trans- and cis- octahedral sites in structures of 2:1 dioctahedral phyllosilicates. O_a represents the apical oxygen atoms shared with tetrahedral, O_{oct} is the anionic site shared between the adjacent octahedral, and a and b are unit-cell parameters (Brigatti et al., 2006; Meunier, 2005)

The silica tetrahedral sheet and the octahedral sheet are joined by sharing the apical oxygens or hydroxyls (Figure 1) to form two types of layers: 1:1 clay mineral layer, in which one tetrahedral sheet is bonded to one octahedral sheet (e.g., kaolinite) or the 2:1 clay mineral layer, in which one octahedral sheet is sandwiched between two tetrahedral layers (e.g., illite). The theoretical crystal structures (without deformations) of both types of layers depend on the hexagonal symmetry of the tetrahedral and octahedral sheets which are linked to each other. The apical oxygens of the tetrahedra become the vertices of the octahedra. Thus, the six vertices of the octahedra in a 1:1 layer are formed by 4 OH⁻ radicals and 2 apical oxygens of the tetrahedra. In 2:1 layers, they are formed by 2 OH⁻ radicals only because the other four vertices are the apical oxygens of the two tetrahedral sheets.

The octahedral sheet is formed by two kinds of octahedra: cis-octahedra (2 M_2 sites per half unit cell, hfuc, being based on three octahedral sites) in which OH⁻ groups form one side of a triangular face on the right or on the left, and trans-octahedra (1 M_1 site per hfuc) in which OH⁻ groups are located on the opposite vertices (Figure 2 and Figure 3). Planes defined by the OH⁻ groups when they are in the trans-position become planes of symmetry of the octahedral sheet, but this is not true for the cis-position (Meunier, 2005).

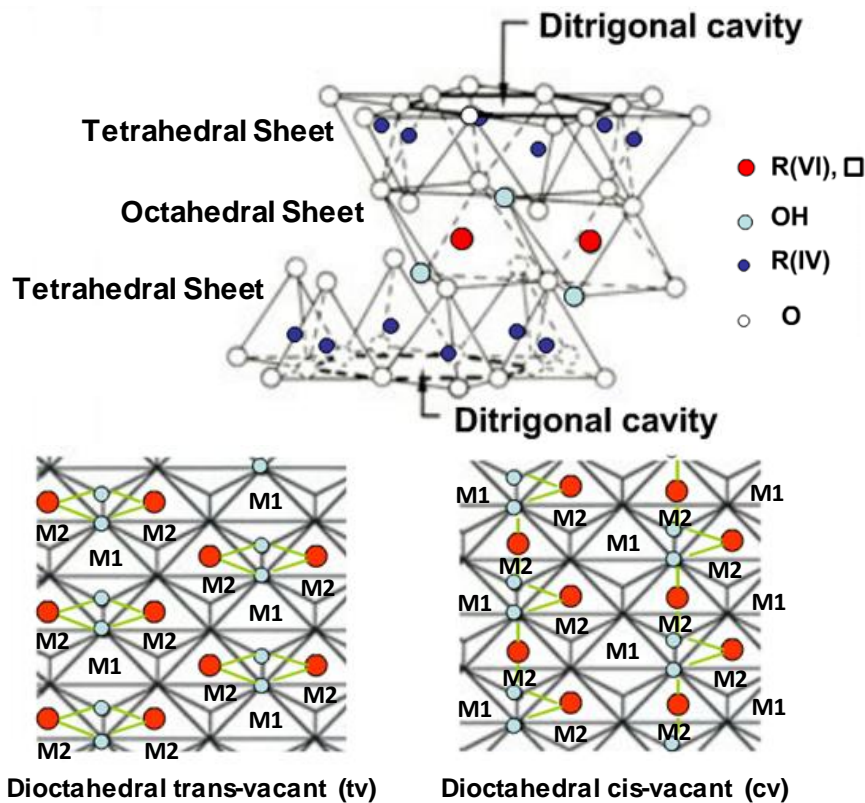


Figure 3. Trans-vacant (tv: opposite site) and cis-vacant (cv: same site) octahedral sites in structures of 2:1 dioctahedral phyllosilicates

Furthermore, the tetrahedral and octahedral sheets exhibit differing a and b dimensions. Thus, their linkage cannot possibly take place without deformation of the angles and lengths of some chemical bonds. These deformations are significant in dioctahedral layers; and minor in trioctahedral layers. In an ideal structure, the displacement of the tetrahedral chains across the octahedral strips is $\pm c/3$. The symmetry group to which phyllosilicates belong depends on the way 1:1 or 2:1 layers are stacked (monoclinic, orthorhombic, triclinic, etc.).

Therefore, the structure and composition of major clays are very different even though they are each comprised of octahedral and tetrahedral sheets as their basic building blocks. The arrangement and composition of the octahedral and tetrahedral sheets account for most of the differences in their physical and chemical properties (Murray, 2006; Brigatti et al., 2006).

The structure of palygorskite was first described by Bradley (1940). Palygorskite is a 2:1 type phyllosilicate (Figure 4) whose structure is derived from talc-like (TOT) ribbons (two tetrahedral silica sheets bond to another central magnesian one in octahedral coordination) that expand along the axis of the fibers (c -axis). Each ribbon is connected to the next by inversion of SiO_4 tetrahedral along a set of Si-O-Si bonds (i.e., $[\text{SiO}_4]^{4-}$ tetrahedral periodically point outward and inward in groups of four), resulting in a continuous two-dimensional tetrahedral

sheet and a discontinuous octahedral sheet. TOT ribbons (or polysomes) extend parallel to the X-axis (a unit cell dimension), and have an average width along Y (b-axis) of two linked pyroxene-like $(\text{SiO}_3)^{2-}$ single chains, like amphibole $(\text{Si}_4\text{O}_{11})^{6-}$. Thus, the periodical $[\text{SiO}_4]^{4-}$ tetrahedral inversion produces each two tetrahedral chains in the [100] direction (b-axis), the tetrahedral sheets being bound to octahedral sheets which are discontinuous in the [010] direction (a-axis), and continuous and elongated in the [001] direction (c-axis), which gives the crystals a fibrous appearance. As consequence, they are disposed according to a chessboard-like arrangement when observed on the (001) plane (Figure 5), linked one another via Si-O-Si bridges, and rectangular channels and tunnel-like nanopores ($3.7 \times 6 \text{ \AA}$ wide in cross-section) are formed between opposing 2:1 ribbons through which water and other fluids can penetrate.

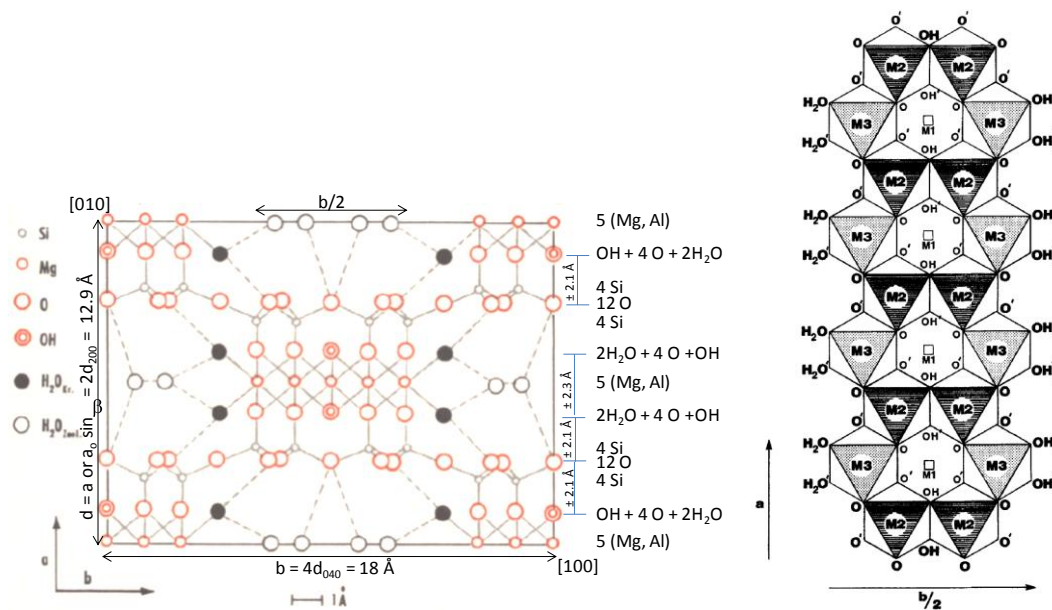


Figure 4. a) Structure of the palygorskite from Bradley (1940) projected in the [001] plane: $2[(\text{OH}_2)_4 (\text{Mg, Al, Fe})_5(\text{OH})_2 \text{Si}_8\text{O}_{20}] 4\text{H}_2\text{O}$. Monoclinic $a_0 \sin \beta = 12.9 \text{ \AA}$, $b_0 = 18.0 \text{ \AA}$, $c_0 \sim 5.2 \text{ \AA}$ (after Haden and Schwint, 1967); b) Configuration of the octahedral ribbons in the palygorskite structure having M1, M2, and M3 octahedral sites. The a-axis of palygorskites corresponds to c-axis of the micas (from Güven et al., 1992)

The octahedral sheet in this structure has a di- and/or tri-octahedral character depending on the divalent/trivalent cation ratio, distribution of cations, and occupancy of the octahedral sites. The half unit cell is made up of five (Mg,Al, Fe)-(O-OH) octahedral strips ordered in such way that the vacant site is at the centre of the chain. There are three octahedral sites M1, M2 and M3 in the structure. The inner octahedral cation is M1 type with a trans-OH configuration and is the vacant octahedral site. The two following ones (M2 type) display a cis-OH configuration, which are coordinated to two hydroxyls shared between two adjacent octahedral. The last two terminal cations located on edges of the octahedral sheet are M3 type, which complete their coordination shells with two molecules of water (structural water). The linked ribbons thus form a continuous

2:1 layer along the c-axis (fiber direction) with a limited extent along the b-axis, with interstices or nanopores among the chains running parallel to the fiber axis and filled at room temperature by zeolitic water molecules that are hydrogen bonded to the structural water. As a result of the discontinuity of the silica sheets, silanol groups (Si-OH) are present at the edges of the channels along the fiber axis (c-axis), which are formed by broken Si-O-Si bonds on the external surfaces balancing their residual charge by accepting either proton or a hydroxyl group to form Si-OH groups. These silanol groups can react with organic reagents to produce covalent bonds that strongly attach the organic substances to the clay (Serratos, 1979).

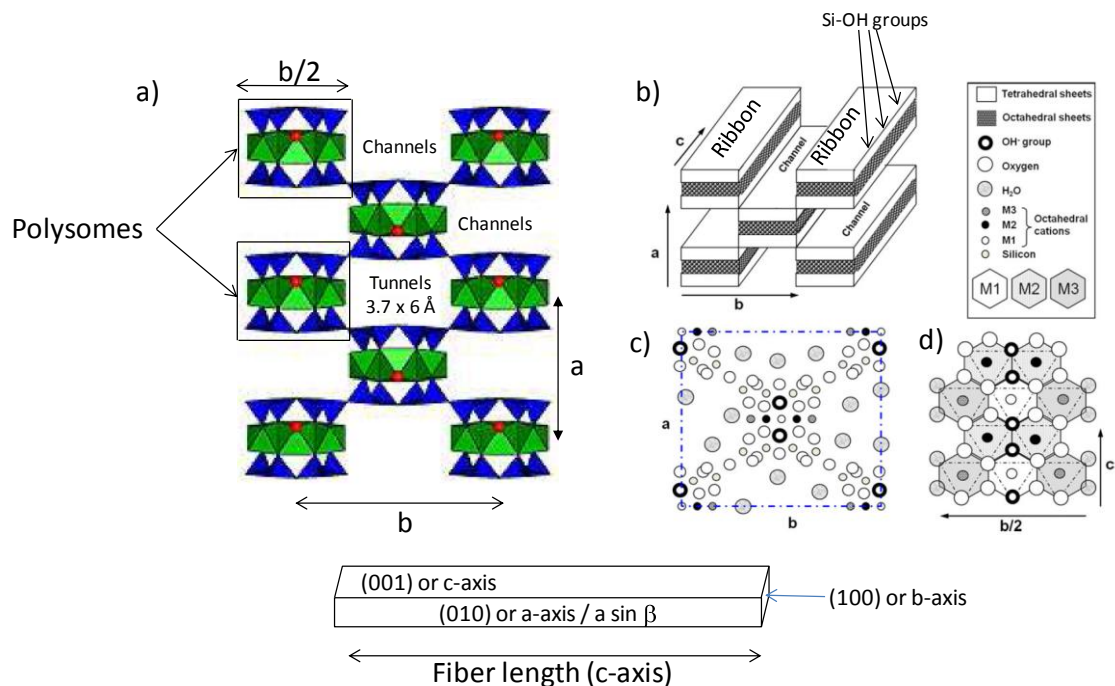


Figure 5. Schematic representation of palygorskite structure: a) Modular structure of palygorskite along the c-axis and overview of polysomes (2:1 TOT ribbons), channels and tunnels, b) overview of fibrous morphology, the presence of channels and the formation of discontinuous ribbons, c) projection on (001) plane (c-axis), d) projection on 010 plane showing an octahedral ribbon with the M1, M2 and M3 sites as well as structural hydroxyls, coordinated and zeolitic water (after Suárez and García-Romero, 2006; and Krekeler and Guggenheim, 2008)

Palygorskite exhibits low amounts of isomorphous tetrahedral substitutions (Al^{3+} for Si^{4+}), but Al^{3+} , Fe^{3+} and to a lesser extent Fe^{2+} ions, frequently substitute for octahedral Mg^{2+} . Thus, a small number of exchangeable compensating Na, K, Ca and Mg cations, zeolitic water and four structural OH_2 molecules per formula unit bonded to M3 sites are contained in the channels (Mifsud et al., 1978; Suárez and García-Romero, 2011; García-Romero et al., 2006; Huang et al., 2007).

Palygorskite has a general formula:



where R^{3+} ions are commonly Al^{3+} and Fe^{3+} , depending on the origin and deposition condition; \Box is the octahedral vacancy. E^{2+} represents the exchangeable cations in the microchannels and its amount $(x-y+2z)/2$ is assumed to be equal to the excess charge for the half unit cell. Therefore, according to the relative displacements of the unit cell, palygorskite crystal structure can be either orthorhombic, space group Pnmb (Bradley, 1940; Preisinger, 1963; Drifts and Sokolova, 1971), or monoclinic, space group C2/m, (Christ et al., 1969; Artioli and Galli, 1994; Giustetto and Chiari, 2004; Bailey, 1980), or a mixture of monoclinic and orthorhombic polymorphs (Christ et al., 1969); and a variable dioctahedral-trioctahedral character can be assigned to palygorskite (Galán and Carretero, 1999; Chachi et al., 2002). The dioctahedral end-member at $y=2$ and $z=1$ ($\text{R}^{2+}/\text{R}^{3+}=1$) is characterized by the formula $(\text{Mg}_2\text{R}^{3+}_2\Box_1)(\text{Si}_{8-x}\text{R}^{3+}_x)\text{O}_{20}(\text{OH})_2(\text{OH}_2)_4(\text{E}^{2+}_{x/2})\cdot 4(\text{H}_2\text{O})$, showing that only four of five octahedral positions available are filled with R^{3+} occupying M2 sites and Mg^{2+} occupying M3 while M1 is vacant, and $x=0.5$. On the other hand, the trioctahedral end-member palygorskite at $y=0$ and $z=0$ is represented by the formula $\text{Mg}_5(\text{Si}_{8-x}\text{R}^{3+}_x)\text{O}_{20}(\text{OH})_2(\text{OH}_2)_4(\text{E}^{2+}_{x/2})\cdot 4(\text{H}_2\text{O})$ for which all the five octahedral positions are filled with Mg^{2+} . Chachi et al. (2002) found evidence of trioctahedral Mg_3OH features (Güven et al., 1992).

Two different types of water residing in the open channels can be identified: crystalline or coordinated water bonds directly to the exposed Mg^{2+} ions (at M3 sites) to fulfill their coordination requirements, whereas zeolitic water interacts with both the coordinated water molecules and the tetrahedral sheet. Besides, dehydroxylation water exists inside the octahedral sites. Therefore, each crystal unit normally contains eight water molecules (Figure 4). Four water molecules are bonded two per two to the first and the fifth Mg^{2+} cations at the both ends of each ribbon and located in nanochannels. These molecules are called bound (structural or crystalline water) water. Furthermore, four water molecules per half-unit cell are located two per two within the nanochannels in the both side of each other ribbon. These water molecules in hydrogen bonded with bound water and each other are called zeolitic water. The zeolitic water is easily lost at a relatively low temperature (lower than 120°C). Finally, one water molecule per half-unit cell of palygorskite formed from two hydroxyls on the third Mg^{2+} cation (at M2 sites) is called dehydroxylation water (Figure 4b). When the zeolitic water is removed, each channel has an estimated free cross-section about 3.7 by 6.0 Å parallel along the X-axis. Preisinger (1963) proposed that loss of the bound H_2O causes a phase change during which the structure folds by rotation of the phyllosilicate ribbons about an axis through the Si-O-Si bonds that link the ribbons. The folded anhydrous structure is shown in Figure 6. The theoretical content of the

zeolitic water (ZW), bound water (BW) and dehydroxylation water (DW) are 8.53, 8.53 and 2.13 %mass, respectively, the molar mass being of 4:4:1 (Martín Vivaldi and Fenoll Hach-Ali, 1970). Moisture water, physically adsorbed at ambient conditions, present in variable quantities and located interparticle, is exchangeable and is not shown in the chemical formula of palygorskite.

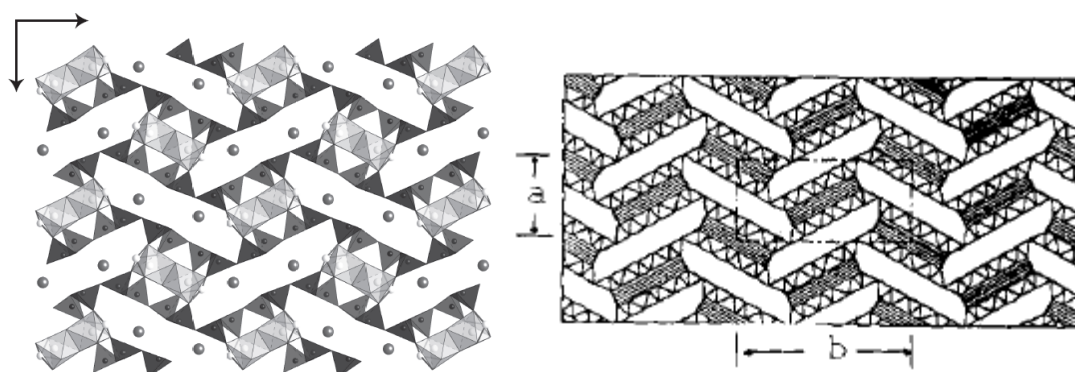


Figure 6. a) Folded structure after heating the palygorskite viewed along the monoclinic c-axis [001] (from Post and Heaney, 2008), b) Sepiolite anhydride (Serratos, 1979)

The 2:1 inverted structure of palygorskites, resulting in parallel channels or tunnels throughout the particles, are responsible for their large specific surface area ($190 \text{ m}^2/\text{g}$) and the excellent sorptive properties, once the zeolitic water has been removed by thermal treatment or thermal activation (Figure 7). This hierarchical distribution causes the high porosity and surface area properties of the palygorskite clay mineral, the pore size distribution being classified in (Cases et al., 1991; Suárez and García-Romero, 2012): intracrystalline or structural microporosity and textural porosity: interfibre microporosity, mesoporosity and macroporosity (Figure 8). This textural porosity is dependent on the arrangement of the fibers and, therefore, each sample has its own characteristic features. Regarding its morphology, palygorskite is an elongate chain in shape ($> 5 \text{ \AA}$) and often occurs as bundles of elongate and lath-like particles. Fiber sizes vary widely but generally range from 100 \AA to $4\text{-}5 \text{ }\mu\text{m}$ in length, 100 \AA to 300 \AA in width, and 50 to 100 \AA in thickness (Galán, 1996). The cation exchange capacity ranges from 4 to 40 meq/100 g, the higher values being probably due to the presence of impurities (e.g., smectites). The high SA and medium exchange capacity give a high capacity to absorb substances and various liquids. The elongate thin particles cause high viscosity when added to any liquid being a very stable as a viscosifier.

The particular structural and textural features of these fibrous clay minerals determine their special behavior in the development of advanced materials. In particular, the presence of structural cavities (tunnels and channels), silanol groups on the external surfaces and of different types of water molecules determines their surface properties and, therefore, their ability to interact with many compounds forming nanostructured materials.

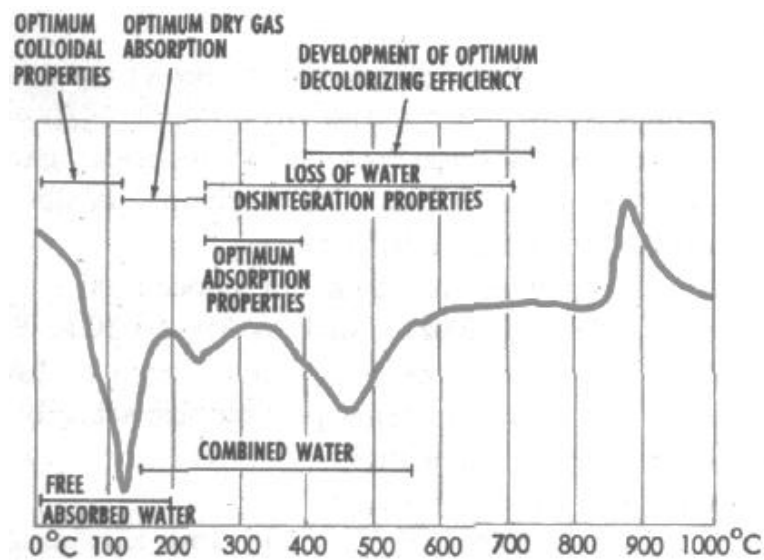


Figure 7. Development of optimal properties of palygorskites by thermal activation (heating) showed on a differential thermal (DTA) curve (Haden and Schiwint, 1967)

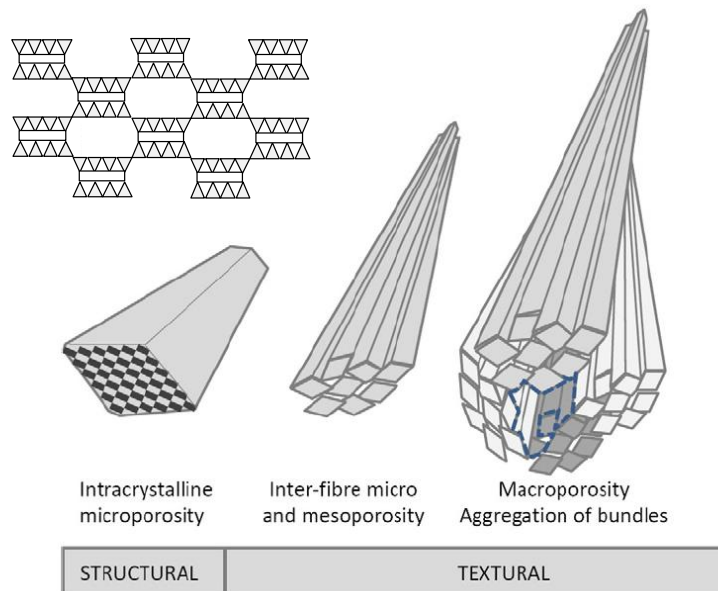


Figure 8. Schematic representation of the hierarchical distribution of pores in palygorskite from the intracrystalline and structural microporosity to the textural mesoporosity and macroporosity caused by the aggregation of bundles of fibres (after Suárez and García Romero, 2012)

The occurrence of palygorskites and sepiolites in the Spanish Tertiary basins has been reported in Torres-Ruiz et al. (1994), Friend and Dabrio (1996), Galán and Pozo (2011) and references therein. Nowadays, two main deposits of palygorskite are being exploited (IGME, 2010). One of them is in Bercimuel (Duero Basin, Segovia) exploited by MYTA (Mining and Technology of Clays, SA) with a total production of 20-25 kt/year. The other one is in Torrejón el Rubio (Cáceres) by MITOSA, where although the mineral is not currently extracted, a small production is maintained (< 2 kt/año). Other small non-exploited deposits, composed by a mixture of palygorskite and sepiolite clay minerals are: Campo de Calatrava (Manchegan Basin, Ciudad Real), Lebrija (Guadalquivir Basin, Sevilla), Tabladillo (Altomira Basin, Guadalajara), Esquivias (Madrid Basin, Madrid) and Mara deposit (Calatayud Basin, Zaragoza).

Although a lot of studies have been performed in these deposits about the genesis, mineralogy, properties and crystallochemistry of the palygorskite clay minerals (see Galán and Pozo, 2011), a general program of research on the characterization and physico-chemical, textural and structural properties based on both experimental and theoretical studies is still incomplete. In this work, a comprehensive characterization on palygorskite samples from Torrejón el Rubio (Cáceres) based on X-Ray diffraction (DRX), Infrared spectroscopy (FTIR), thermogravimetric analysis coupled with calorimetry (TG-DSC), X-Ray fluorescence (XRF), Scanning electronic microscopy (SEM) and chemical analyses join together with theoretical DFT (density functional theory) calculations was performed. The objectives were: 1) to analyse the composition, crystallinity and physico-chemical and thermal properties of the palygorskite; 2) to investigate the isomorphous octahedral cation substitution and water content in this type of clay; and 3) to identify this type of clay minerals at atomic level in order to study its crystallochemical microstructure.

2 Materials

2.1 Geological setting

In Spain, the most important Tertiary continental basins are along the Tajo, Duero, Ebro and Guadalquivir rivers (Figure 9). Palygorskite and Fuller's Earth clays (mainly a mixture of palygorskite and smectite) deposits are located in these basins. The Torrejón el Rubio palygorskite deposit is located in a small Tertiary fault basin, called Basin of Talaván - Torrejón el Rubio, which is a western continuation of the Tagus Basin (Galán and Pozo, 2011).

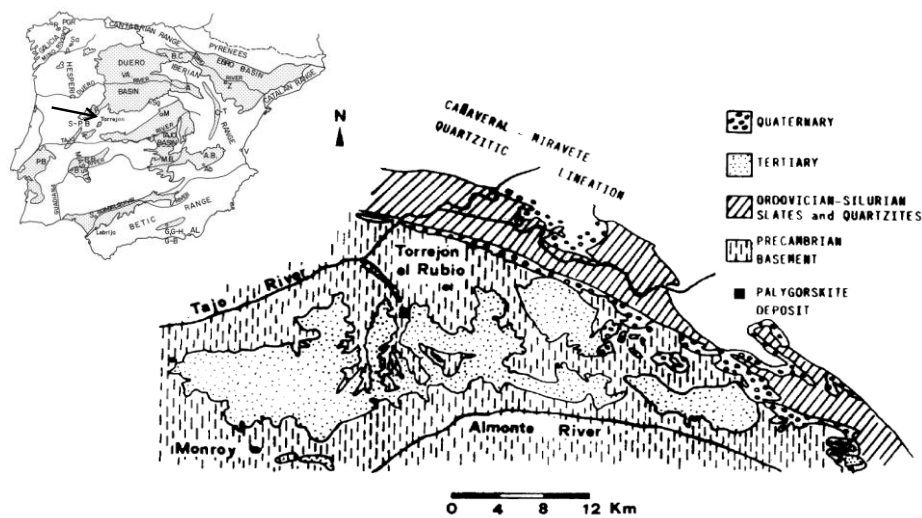


Figure 9. Geographical and geological setting of the Talaván – Torrejón el Rubio Basin (after Galán and Pozo, 2011 and Fernández-Macarro and Blanco-Sánchez, 1990)

The Tagus Basin is an intracratonic basin formed by fragmentation of the Iberian Massif, or Iberian microplate, as a result of differential tectonic strains during the Alpine orogeny. The Tagus basin was filled by a continental sedimentation which extends from the Paleocene to the Quaternary, the materials deriving from the surrounding mountains. During the Pliocene times the basin tilted towards the south-west.

The basin of the Tajo (Tagus basin) can be divided into three sections or sub-basins: the eastern, the central and the western. The Altomira Sierra separates the eastern and the central, and the threshold of Talavera de la Reina (Toledo), separates the western from the central. Towards the south, and separated by the Toledo Mountains, the Tajo basin connects with the Ciudad Real-Daimiel basin (the Manchegan basin); and toward the south-east, it continues along the Albacete basin.

The Tertiary Basin of Talaván – Torrejón el Rubio stands out among the Spanish-Portuguese Tertiary basins, occupies around 250 Km² and, generally, extends east-west with a maximum

length of 37 km and a width of 12 km (Galán et al., 1975). This basin is located towards the south of the Cañaveral Miravete quartzite lineation in the province of Cáceres (Spain) and at the south of the Sierra de las Corchuelas, extending to the west towards the town of Talaván, southward to Monroy and East to Jaraicejo village (Figure 9). From a geological point of view, the base of this basin is made up of Upper Precambrian grauwackes, schists and slates. Its northern and north-eastern limits are composed of the Ordovician and Lower Silurian quartzites and slates (Sierra de las Corchuelas, Sierra de Miravete and Sierra Extranjera) that separate this small basin from the large Tertiary Basin of the Tajo. Its southern and south-eastern limits are two extensive outcrops of Hercynian granites surrounded by aureoles of cornubianites (Fernández-Macarro and Blanco-Sánchez, 1990; Galán and Castillo, 1984). The basement is affected by two systems of Hercynian fractures running NE-SW and SE-NW: Plasencia Fault and the Alentejo-Plasencia Fault, which were active during the Miocene and Quaternary.

The filling of the basin of Tertiary age Talaván-Torrejón el Rubio was performed by means of continental sedimentary alluvial and fluvial systems. There is not paleontological evidence to their dating, although due to the regional context it is considered contemporary with other basins within this sector of the southern plateau, so we should consider its age as Miocene.

Lithologically, three units can be distinguished in the basin of Talaván-Torrejón el Rubio from the bottom to the top (Galán and Castillo, 1984):

- a) The basement, consisting of brownish-pinkish clayey Cambrian slates with disseminated pyrite and small dikes of milky quartz. The slates are composed of quartz, feldspars, micas, and chlorites of the sheridanite-chlorinoclore type, with kaolinite, smectites, goethite and pyrophyllite occasionally present;
- b) The detrital-clayey bed (5-50 m thickness), made up of an alternation of sands and gravels, with clays more or less rich in quartz, feldspar and carbonates. The levels are lens-shaped and of relatively constant thickness.

The sedimentary record of this basin begins with the Arkosic Cycle (Paleocene). Two elements can be distinguished within the Cycle: the arkosic sedimentation itself and the surface on which it rests – a pre-arkosic peneplain. The Paleocene arkosic series is clearly of fluvial origin and two well differentiated sections can be distinguished. The lower section, located exclusively in the depressed area of the pre-arkosic peneplain, consists of two lithological facies consisting of fining upward sequences: a) an upper unit composed by a sandy microconglomerate facies (0.15-1.5 m): feldspathic sands and gravels (Arcoses) composed mainly by quartz, feldspar, muscovite, biotite, ilmenite and mica-schists (IGME, Serradilla Sheet 651), and b) a lower clayey unit (0.5-4 m, average thickness of 3 m), lying discordantly over the Precambrian Schist-Greywacke Complex and with a discontinuous

character: lutite-sandy, clay facies, distinguished by the presence of a well-developed columnar structure. Overlying the slate basement, the clay bed contains relictic slate with different grades of alteration. Discontinuous carbonatic levels corresponding to carbonatic crust of clearly edaphic origin appear locally. The top of these sequences is affected by processes of alteration associated with edaphic colonization of paleosols (Fernández-Macarro and Blanco-Sánchez, 1990).

Most of the lower clay units are rich in palygorskite (up to 70 wt.%) with lower amount of illite, and varying quantities of chlorite, smectite (saponite) and sepiolite. The highest palygorskite concentration (75-85 wt.%) is in the centre of the basin. However, in other zones of the basin (Figure 10a), the clay units have a higher illite content than palygorskite with the constant presence of smectites (Galán and Castillo, 1984).

- c) The “raña”, of Late Miocene-Pliocene age and, consequently, subsequent to the process of formation of the Tertiary basins. The raña is a reddish flangomerate mudflow deposit of quartzite pebbles containing angular blocks of rock of all sizes, which appears in the marginal zones of the basin associated to the last filling episode of the basins. The raña occupies the topographically higher levels of the basin and occurs mainly in the southern and south-western borders, creating a mesa. The raña is over a meteorization layer (paleo-alteration) formed at the expense of the Schist-Greywacke basement, which consist in a transformation of chlorites and micas in smectites and kaolinites. The evolutionated reddish soil above the raña in Torrejón el Rubio basin is of kaolinitic type (Villamor et al., 1996).

Two main hypotheses have been suggested for the formation of the authigenic palygorskite in the Cáceres deposit. One of them is related with direct precipitation from silicon, aluminium and magnesium solutions (neof ormation) coming from alteration of the basement chlorite-rich slates (Galán and Castillo, 1984). The other one is related with processes of alteration associated with edaphic colonization of paleosols, which affected to the top of the arkosic sequences causing important micromorphological and mineralogical modifications, and culminated in the palygorskite neof ormation (Fernández-Macarro and Blanco-Sánchez, 1990).

According to Galán and Castillo (1984), the lower bed of the detrital-clay unit (palygorskite deposits) is the result of weathering of the Cambrian slate basement in a lacustrine-palustrine environment (Figure 10b). The fluvial-alluvial conditions would have originated with the exposure of slate areas, previously exposed and weathered as the consequence of movement by the faults limiting the basin. The continuity between slates and palygorskite-rich clays observed at a number of points suggests the formation of palygorskite in association with weathering of the metamorphic rock in acidic environment. Weathering of chlorite contained in the slate

would have provided the necessary input of components required for the formation of palygorskite (Galán and Castillo, 1984; Galán et al., 1975).

However, according to Fernández-Macarro and Blanco-Sánchez (1990), palygorskite deposits are related to the degradation of the arkosic components (feldspar, illite/micas, and chlorite) which gave rise to the neof ormation of smectites, the clay paragenesis of the palygorskites. The process would reflect a complex series of reactions in which, on one hand the detritic micas and chlorites, feldspars, and smectites (both detritic and neof ormed) and, on the other hand, the magnesium-rich solutions intervene in the palygorskite paragenesis. The final product was the formation of the palygorskite by reaction of the smectites with the magnesium circulating in the area under arid climatic conditions. The source of magnesium would be precisely the alteration of arkosic componets of the sediment. In the vertical profiles of the quarries studied in the palygorskite deposit at Torrejón el Rubio, it was observed that paleosols more confined and evolve caused massive palygorskite formation, whereas in upper paleosols the edaphic activity gave rise the formation of smectites from the original arkosic components on a stable alluvial plane (Fernández-Macarro and Blanco-Sánchez, 1990).

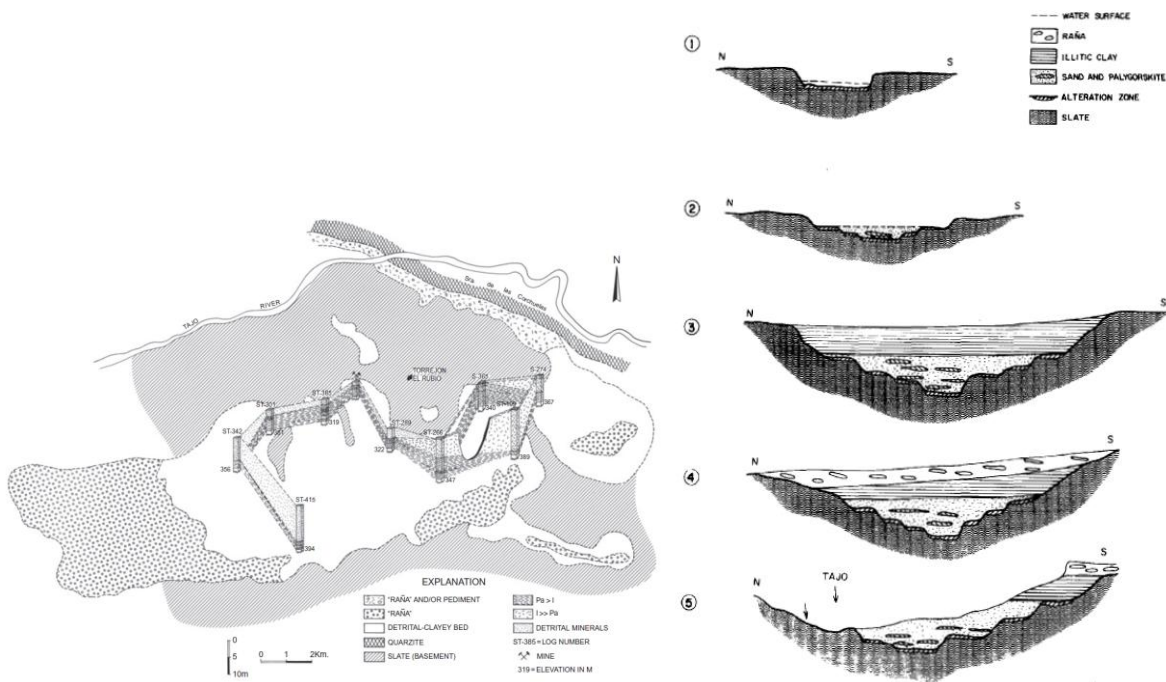


Figure 10. a) Geological map and correlation of cores from the Torrejón el Rubio Basin according to Galán and Castillo (1984); b) Schematic representation of Torrejón El Rubio palygorskite deposit (1: weathering substrate, 2: clayey sand sedimentation and early diagenetic (vadose) magnesium-rich attapulgite, probably related to sedimentation, 3: silting up sedimentation, 4: alluvial fan or “raña” deposits, 5: fluvial network trenching (Galán and Castillo, 1984)

2.2 Palygorskite sample selection

Palygorskite samples were obtained from La Cierva deposit exploited by Minas Torrejón, SA (MITOSA), a subsidiary company of the TOLSA group, which is located in the zone called Olives Hill in between Talaván and Torrejón el Rubio (Cáceres, Spain) inside the Tertiary Basin of Talaván - Torrejón el Rubio. The palygorskite global production is between 2000 and 3000 metric tons per year, the minimum exploitable reserves being around 300,000,000 Tm. The deposit was discovered in 1957, although have been used locally as whitewash since ancient times. The existence of the deposit was studied by Alvarez Estrada and Sánchez Conde (1967), Galán et al. (1975) and Fernández-Macarro and Blanco-Sánchez (1990).

The Palygorskite deposit contains Paleogene palygorskite-rich marls overlying the basement made of Cambrian slates. The deposit has a stratiform morphology with variable power lenticular layers, and it is characterized by its intense white color. The detrital-clay unit has two mineralized beds of which only the lower one (0.5-4 m thick) is exploited (a front of 100 meters length and 5 m high). This two facies (sandy and clay facies) are repeated cyclically. The cycles may have repeating powers between 2 and 4 m. The sandy facies consists of a very coarse grained, microgranulometrics with white and greenish gray tones. Locally erosive scars may appear forming conglomerates with songs of up to 5 cm maximum size that can be described as filling channel facies. The other facies are composed by clays, almost exclusively palygorskite and chlorite.

For this study, palygorskite samples were collected from the white massive outcrop after removing superficial material (Figure 11).



Figure 11. a) *La Cierva* Palygorskite deposit from Torrejón el Rubio (Cáceres), b) Detail of the palygorskite sample collection

3 Methodology

3.1 Experimental methodology

Samples were homogenized, ground and sieved to a particle size smaller than 250 μm prior to mineralogical and chemical characterization.

The mineralogical analysis of the raw and clay fraction samples was performed by X-Ray diffraction (XRD) by using a Philips X'Pert-MPD diffractometer using anticathode $\text{CuK}\alpha$ at 45 kV and 40 mA and a graphite monochromator. The random-powder samples were obtained by mixing 1 g of sample and 0.25 g of α -corundum (internal standard) to analyse the d(060) reflection. The fine fraction of less than 2 μm size fraction was obtained by suspension and sedimentation (Stoke's law) in deionized water. Afterwards, the separation of the < 0.5 μm size fraction was performed by centrifugation at 3000 rpm (20°C) for 5 min. A clay paste was used for the preparation of smear slides with preferred orientation in air-dried state (AO), ethylene glycolated (EG) and heated at 550°C (Moore and Reynolds, 1989). The random-powder specimens were scanned from 2 to 80° 2 θ at a scan speed of 0.02° 2 θ /2 s, whereas a range from 2 to 30° 2 θ was used for the oriented aggregates. Semi-quantitative estimation of minerals was based on their relative XRD peak intensities with respect to the internal standard and areas, as well as based on the reflecting powder (Schultz, 1964): total phyllosilicates 0.15 if > 50 wt.% or 0.1 if <50% wt.%, quartz 1.5, cristobalite 0.6, palygorskite 0.67, and carbonates, K-feldspars and plagioclases 1. In the oriented aggregates the reflecting powders used were: kaolinite 2 at 7.1 Å, chlorite 2 at 7.0 or 14 Å, illite 1 at 10 Å, smectite 4 at 17 Å, vermiculite 3 at 14 Å, sepiolite 1 at 12 Å, and palygorskite 0.75 at 10.5 Å.

Particle morphology and textural characteristics were obtained by scanning electron microscopy (SEM) by using a JEOL microscope, operating at 20 kV and equipped with a Link System energy dispersive X-ray microanalyser (EDX). Prior to SEM examination, freshly surfaces of representative samples were dried at 40°C in an oven and coated with Au under vacuum. The structural formula of palygorskite was obtained from isolated particles and calculated on the basis of 21 oxygens per unit cell (e.g. Newman and Brown, 1987). All Fe present was considered to be Fe^{3+} .

Chemical composition of the < 2 μm clay fraction was obtained by XRF analyses on an Axios spectrometer from Panalytical equipped with a rhodium X-ray tube (stimulation power: 1 KW) using molten pellets. The powdered and homogeneously ground sample (> 0.2 g) was prepared as pressed pellets onto boric acid. 0.1 g of sample were mixed with wax as binding agent. The mixed sample was pressed at 200 kN onto boric acid (40 mm thickness) for 1 min. by using the

sandwich method for obtaining a cylindrical pellets 10 mm diameter and a thickness which depends on the density of the sample.

Fourier transform (FT) IR spectra were obtained in the mid-range infrared (Mid-FTIR) region (4000-400 cm^{-1}) and near-IR (NIR) region (10000-4000 cm^{-1}) by using a Nicolet 6700 with a DTGS KBr detector (spectral resolution 4 cm^{-1} , 32 scans recorded) on KBr-pressed discs in transmission technique. The system was continuously purged with a Parker Balston FTIR purge gas generator, which supplies a H_2O - and CO_2 -free air environment. For Mid-FTIR measurements, two milligrams of powdered sample were dispersed in 200 mg of KBr and subjected to a pressure of 10 ton/ cm^2 to obtain a clear disc (pellet); whereas for NIR measurements the KBr pellets were obtained by mixing 25 mg of sample and 200 mg of KBr.

The thermogravimetric and calorimetric (TG-DSC) experiments were performed on a Setaram Setsys Evolution 16 instrument. The samples were placed into alumina crucibles and heated under argon atmosphere (20 mL/min) at 10°C/min from room temperature to a final temperature of 1100 °C.

Total CEC was measured with 0.01 M copper triethylenetetramine, $[\text{Cu}(\text{trien})]^{2+}$, solution according to Ammann et al. (2005). 200 mg of clayey sample ground in an Agatha mortar were weighed in a 60 mL centrifuge tubes. 25 mL of deionized water were added and the suspension was dispersed by ultrasonic treatment for 5 min. Then, 10 mL of 0.01 M $[\text{Cu}(\text{trien})]^{2+}$ were added and allowed to react by end-over-end shaking for 1 hour. After this procedure, a complete exchange of the $[\text{Cu}(\text{trien})]^{2+}$ complex with the exchangeable cations is guaranteed. Afterwards, the suspensions were centrifuged at a constant rotation speed of 15500 rpm for 20 min. The supernatant solution was filtered through a 0.45 μm syringe-filter. 3 mL of the clear blue solution were filled into 1 cm optical glass cuvettes and the adsorption of the solution was measured spectrophotometrically at a wavelength of 578 nm by using a Spectroquant UV-Vis spectrophotometer from Merck and deionized water as a blank solution. Prior to the tests, a calibration curve to calculate the Cu-Trien concentration was determined from a series of dilute Cu(II)-triethylenetetramine solutions (0.003 M; 0.002 M; 0.001 M; 0.0003 M; 0.0001 M).

The determination of the cation Exchange population was performed by using Cs as index cation (Sawhney, 1970). Solid samples were equilibrated at 1:4 solid to liquid ratio (0.25 kg/L) with 0.5 M CsNO_3 at pH 8.2. After phase separation by centrifugation at 15500 rpm for 20 min, the supernatant solutions were filtered through 0.45 μm and the concentration of the major cations was analysed.

The major and trace cations were analyzed by Inductively Coupled Plasma-Atomic Emission Spectrometry (ICP-AES) in a Jobin Yvon JY48+JY38 spectrometer. Sodium and potassium

were determined by flame atomic emission spectrometry, FAES, in a Perkin Elmer 2280 spectrometer.

To obtain the external BET surface area, classical nitrogen adsorption/desorption isotherms were obtained on a discontinuous volumetry sorptometer, Micromeritics ASAP 2020 V3.02 H. Approximately 2-4 grams of total sample were ground in an agate mortar. Prior to the nitrogen adsorption, the samples were out-gassed by heating at 90°C for 12 hours using a mixture of helium and nitrogen under a residual vacuum of 100 mmHg. Before the heating phase, the material was subjected to a previous vacuum of 10 µmHg for 6 hours. The tests were performed at the boiling point of liquid nitrogen (77 K) considering a molecular cross section area of 0.162 nm for the nitrogen molecule (Gregg and Sing, 1982). External surface areas were calculated using the standard N₂-BET method, using a series of data points over the P/P₀ range of 0.02 to 0.25 on the nitrogen adsorption isotherm. The presence of micropores in the sample was assessed using the t-plot method (de Boer et al., 1966). Pore volume distribution as a function of pore size in the mesopore and low macropore size range was attained using the BJH method by reducing isotherm data (adsorption or desorption) between about 0.05 P/P₀ and saturation (Barrett et al., 1951). The micropore analysis was performed following the Horvath-Kawazoe and DFT (Density Functional Theory) methods (Webb and Orr, 1997).

In order to obtain the *Total specific surface area (SA)*, water vapour gravimetric adsorption measurements were performed by Keeling's hygroscopic method (Keeling, 1961) by storing the samples at a constant 75% relative humidity atmosphere in a chamber over-saturated in NaCl solution for 1 month. Prior to the tests the samples were dried at 110 °C during 24 hours. The weight changes of the samples as the adsorbed amount of water were measured and related with the total surface area, SA.

In contrast to nitrogen, which is only adsorbed at the external surface of the stacks of the layers, water molecules can be adsorbed on the whole surface, including both the internal (interlayer) and external surfaces of the clay minerals. The total amount of adsorbed water of each sample with its specific mineralogical composition stands in equilibrium with the relative humidity. The amount of adsorbed water at the interlayers depends on the type of adsorbed cations.

The equilibrium pH was measured in distilled water, 0.01 M CaCl₂ and 1M KCl suspensions at 1:20 solid to liquid ratio.

The gravimetric water content, *w.c.*, is defined as the ratio between the weight of water and the weight of dry solid expressed as a percentage. The weight of water was determined as the difference between the weight of the sample and its weight after oven drying at 110°C for 24 hours (weight of solid).

The specific gravity, γ_s , of the solid particles is defined as the relation between the weight of the solid and the volume occupied by it. Specific gravity has been determined by using a Micromeritics helium gas pycnometer AccuPyc II 1340, which apply the gas displacement technique to measure the volume of a solid material.

3.2 Crystal simulation methodology: Density Functional Theory (DFT)

The palygorskite model was built in between the two polymorphs that exist in nature (orthorhombic and monoclinic) from the geometry published by Giustetto and Chiari (2004) with orthorhombic symmetry. The structure has a pleated 2:1 layered structure consisting of continuous (Si, Al)₂O₅ sheets which are linked by octahedral ribbons (Mg, Al, Fe³⁺) having cationic substitutions of Al³⁺ and Fe³⁺ by Mg²⁺, as it was described in the previous section. Because of lack of knowledge about the experimental hydrogen positions of palygorskite, a crystal cell model was built adding hydrogen atoms to attain a neutral structure. Hydrogen atoms that were situated on octahedral hydroxyl oxygen's, these positions being fully optimized.

Due to palygorskite normally have variable water content, no so much zeolitic water and fully hydrated, we have considered three models containing zero, eight and sixteen water molecules per two unit cells (Figure 4a). Zeolitic water was situated inside the edges of the rectangular channels as it was described by Artioli and Galli (1994), while coordinated water was linked bonding to Mg octahedral atoms. Because of the experimental sample contains iron, a model with one isomorphous substitution of Fe³⁺ by Al³⁺ was also described in order to study the effects of the iron atoms inside the palygorskite structure.

DFT calculations for bulk geometry optimization and infrared spectra simulations were also carried out by using the CASTEP code (Clark et al., 2005) with the generalized gradient approximation (GGA) PBE (Perdew Burke Ernzerhof) and the functional RPBE (Revised Perdew Burke Ernzerhof) (Hammer et al., 1999). The ions were described by ultrasoft and non-local norm-conserving atomic pseudopotentials. Brillouin-zone integrations were performed using a 1 x 1 x 2 Monkhorst-Pack (MP) grid (Monkhorst and Pack, 1976) due the big size of the unit cell. A recent work has proved the accuracy of these studies to characterize these materials (Alvarado et al., 2012).

The atoms of the structure together with the additional added water molecules in the unit cell were allowed to relax to the lowest energy configuration. Wave functions were expanded in a plane-wave basis set up to an energy cut-off 400 eV and the total energy was converged to less than 2.0-5.0 eV/Å for the medium threshold of CASTEP code. A second fine threshold was

applied to calculate the infrared spectra with more accuracy by setting the forces to a value of 0.03 eV/Å and the energy to a value of $1.0 \cdot 10^{-5}$ eV/Å.

Vibrational properties were calculated using the linear response density functional perturbation theory (Baroni et al., 2001) implemented in the CASTEP code, where the phonon frequencies at the gamma point of the Brillouin zone were computed using atomic displacement perturbations. The Materials Studio 6.0 software was used to visualize the results (Materials Studio Modelling, 2010).

4 Results and Discussion

4.1 Physico-Chemical Characterization and Textural properties

The mineral of palygorskite from La Cierva deposit in Torrejón el Rubio (Cáceres) is white in color in the whole massive outcrop. The specific gravity determined by helium gas pycnometry was of 2.454 ± 0.002 g/cm³. The main physico-chemical characteristics of this palygorskite are summarized in Table 1. The CEC values were found 5 meq/100g and 7 meq/100g in the total and in the < 2 μm size fractions, respectively. The main exchangeable cation is Mg (55%), containing also Na (24%), Ca (19%), and K (2%). These cations, located in the microchannels, electrostatically balance the excess of charge in the structure of the palygorskite due magnesium (octahedral layer) and possibly to silica (tetrahedral layer) substitutions. The CEC values in palygorskites range between 4 to 40 meq/100g (Galán, 1996), but the higher values are related to impurities of swelling smectites. Therefore, according to the results obtained for Torrejón el Rubio samples this palygorskite is quite pure and smectite particles are not present, as it is seen in the glycolated oriented aggregates by XRD.

Regarding to the textural properties, palygorskite is highly sorptive in its natural form, taking up water (loosely held by Van der Waals forces) rapidly to 200% of its own weight (Haden and Schwint, 1967). The unusually large surface area of palygorskite is a leading factor in its high adsorption. Both the total surface area (fully saturated state) and the external surface areas (dry state) were determined by water and nitrogen adsorption/desorption experiments, respectively. Water, as a polar molecule, can be absorbed in more sites than intracrystalline channels and external surfaces (e.g., solvating interlayer cations), while nitrogen and other non-polar gases cannot. Differences in the nature of sorption may result in different surface area.

For the Torrejón el Rubio bulk palygorskite, the total surface area, determined by water adsorption at a relative water activity of 0.75 (75% R.H.), was of 257 ± 7 m²/g. However, the external specific surface area, calculated by the Brunauer, Emmett and Teller (BET) method (Brunauer et al., 1936) after outgassing at a residual pressure of 10 μmHg for 6 hours and at a

temperature of 90 °C, was 104 m²/g. Here, it is interesting to note that in the case of palygorskites, the total external surface area corresponds to the external faces and the edges of the clay particles, but may also include the filling of the tunnels and cavities if ultra-low relative pressures P/P₀ are used. Therefore, nitrogen and water adsorption may have a similar behavior on the contrary to what occurs in swelling clay minerals where nitrogen doesn't enter to swellable interlayer sites.

The nitrogen adsorption-desorption isotherm (Figure 13a) is of Type I at lower relative pressure (P/P₀: 4.25·10⁻⁷ to 1.83·10⁻³, before the knee), characteristic of a microporous material; and of Type IV at higher relative pressures (P/P₀: 1.83·10⁻³ to 0.99), characteristic of a mesoporous material. The rounded knee indicates the approximate location of monolayer formation. Low slope region in middle of isotherm indicates first few multilayers, on external surface including meso- and macro-pores before the onset of capillary condensation. The curve exhibit a H3 hysteresis loop in the desorption isotherm due to the presence of mesopores and the capillary condensation in these pores formed among different clay mineral particles (interparticle pores), and also it is characteristic of the presence of slit-shaped pores formed by the subparallel arrangement of the fibers in plates (Webb and Orr, 1997).

Table 1. Mineralogical composition and physico-chemical properties of the palygorskite from La Cierva deposit (Torrejón el Rubio, Cáceres)

Mineralogy	Value	Physico-Chemical properties	Value
Total Fraction		CEC (meq/100g) Total fraction	5.27 ± 0.20
Total Phyllosilicates (wt.%)	60	Exchangeable Ca (meq/100g) _{TF}	1.01 ± 0.08
Quartz (wt.%)	26	Exchangeable Mg (meq/100g) _{TF}	2.91 ± 0.16
Cristobalite (wt.%)	1	Exchangeable Na (meq/100g) _{TF}	1.28 ± 0.08
K-Feldspar (wt.%)	12	Exchangeable K (meq/100g) _{TF}	0.11 ± 0.01
Barite (wt.%)	1	Σexch. cations (meq/100g) _{TF}	5.36 ± 0.33
Ilmenite (wt.%)	Traces	CEC (meq/100g) _{< 2 μm Fraction}	7.00 ± 0.10
< 2 μm Fraction		Total S (m ² /g)	257 ± 7
Palygorskite (wt.%)	97 (57)	S _{BET} (m ² /g)	104.1
Muscovite/illite (wt.%)	2 (2)	pH _{H2O} , pH _{CaCl2} , pH _{KCl}	7.9, 7.31, 7.47
Chlorite (wt.%)	1 (1)	Specific Weight (g/cm ³)	2.454 ± 0.002

(*) in parenthesis wt.% regarding total phyllosilicates in total fraction

The BET specific surface areas from Palygorskite from Torrejón el Rubio (Spain) is lower than other values reported for palygorskite samples of other origins (Kuang et al., 2004: 196 m²/g, Barrer and Mackenzie, 1954: 195 m²/g; Serna et al., 1977: 195 m²/g; Suárez Barrios et al., 1995: 186 m²/g), which could be explained by the outgassing temperature that was of 90°C in this

work. It must be taken into account that in palygorskite, the surface area available depends mainly on the nature of the molecules (size, shape, polarity) used as an adsorbate to penetrate the intra- or structural microporosity, the pretreatment (temperature and extent of outgassing), and the method used for adsorption (Cases et al., 1991). Fernández Alvarez (1978) found that the BET specific surface of palygorskite from Torrejón el Rubio (Serradilla, Cáceres) increases progressively with the loss of hygroscopic and zeolitic water from 60 m²/g at 20°C and 110 m²/g at 40°C until a maximum value of around 146 m²/g when this kind of water is eliminated at 75 °C (Figure 12). Further heating produces the loss of crystalline water decreasing the specific surface until 56 m²/g at 175°C due to the loss of microporosity produced by the folding of the structure (Figure 6). The decrease of surface area is the result of the thermal treatment in which open channels of the crystalline palygorskite collapse. As comparison, the total surface area of commercial palygorskite ranges from as high as about 210 m²/g for the colloidal grades to 125 m²/g for the thermally activated sorptive grades, although this depends on the treatment of the samples before BET tests (outgassing temperature, drying, etc.). An abrupt decrease in surface area from 192 to 128 m²/g is reported even at temperatures between 95°C and 115°C (Haden and Schwint, 1967). Therefore, the obtained BET value of 104 m²/g is related to the partial loss of zeolitic water from the palygorskite channels during the outgassing process at 90°C. However, as we are going to see this process only affect to the BET data but not to the whole interpretation of the nitrogen adsorption/desorption test. The low BET specific surface area of palygorskite is also related to less edge surface or fewer imperfections than that observed for sepiolites (around 320 m²/g), and it has been suggested as a degree of crystallinity of this mineral, which is also related with the presence of structural SiOH groups at crystal edge sites (Fernández Alvarez, 1971; Ahlrichs et al., 1975; Serna et al., 1977). Therefore, the presence or not of SiOH groups can also explain the differences in BET surface area values among different palygorskites.

The micro-, meso- and total external specific surface areas were determined according to t-plots (Figure 13b) and Harkins-Jura methods (de Boer et al. 1966). A t-plot analysis of the adsorption isotherms gives a micropore area of 81 m²/g, a micropore volume of 2.28·10⁻² cm³/g and a total external surface area of 135 m²/g (Table 2). These values are similar to those obtained by Kuang et al. (2004) on palygorskite PFI-1 (Florida, USA); and the total external surface area calculated by means the t-plot treatment is similar to reported values for the same palygorskite thermally activated (see above).

Table 2. Parameters deduced from BET and t-plot treatment on the adsorption of N₂ at 77K

Method	C _{BET}	V _m (cm ³ /g)	S _{BET} (m ² /g)	S _{tot} (m ² /g)	V _{tot} (cm ³ /g)	S _{micro} (m ² /g)	V _{micr} (cm ³ /g)	S _{ext micro} (m ² /g)	S _{ext meso} (m ² /g)	V _{meso} (cm ³ /g)
t-plot	-269.1024	3.68·10 ⁻² (l)	104.10	134.62	57.2·10 ⁻³ (l)	80.90	2.28·10 ⁻² (l)	53.73	61.29	1.74·10 ⁻² (l)
DFT	Volume in pores < 4.8 Å (cm ³ /g)		0	Total area in Pores ≥ 4.8 Å (m ² /g)		340.465	Total volume in pores ≤ 449 Å (cm ³ /g)		0.21541	

V_m: monolayer capacity derived from the BET treatment; expressed as liquid (l); S_{BET}: BET Surface area
 S_{tot}: Total surface area derived from the slope of the straight line passing through the origin of the t-plot
 V_{micr}: Liquid micropore volume derived from the ordinate at the origin in the second straight line of the t-plot
 S_{ext micro}: Surface area out of micropores derived from the slope of the second straight line of the t-plot
 V_{tot}: Total pore volume, derived from the amount of nitrogen adsorbed at p/p₀ of 0.98
 S_{ext meso}: Surface area out of mesopores derived from the slope of the third straight line of the t-plot
 V_{meso}: Liquid mesoporous volume derived from the ordinate at the origin in the third straight line of the t-plot
 S_{micro}: S_{BET} - S_{meso} = S_{BET} - (S_{ext micro} - S_{ext meso}): Surface area of the micropores (micropore area)

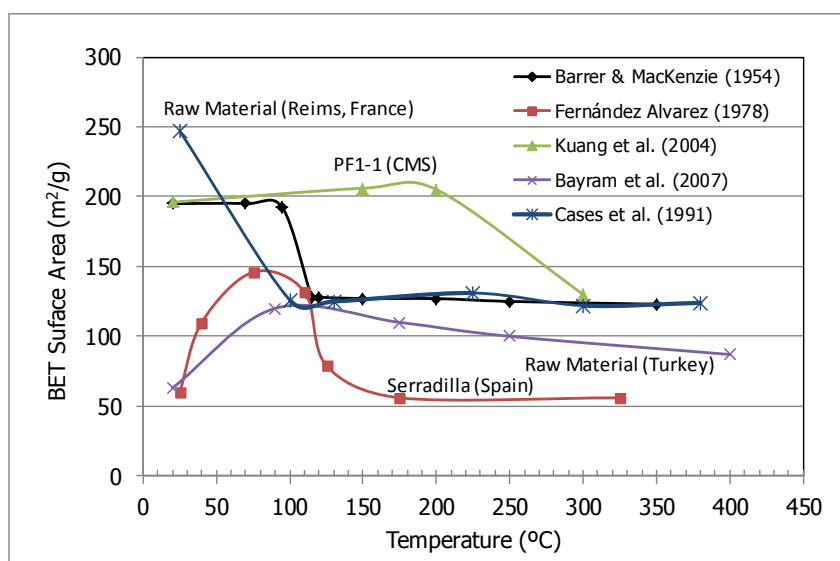


Figure 12. BET surface areas obtained from palygorskite samples as a function of temperature obtained at different experimental conditions (outgassing or drying temperature). After Serratos et al. (1979)

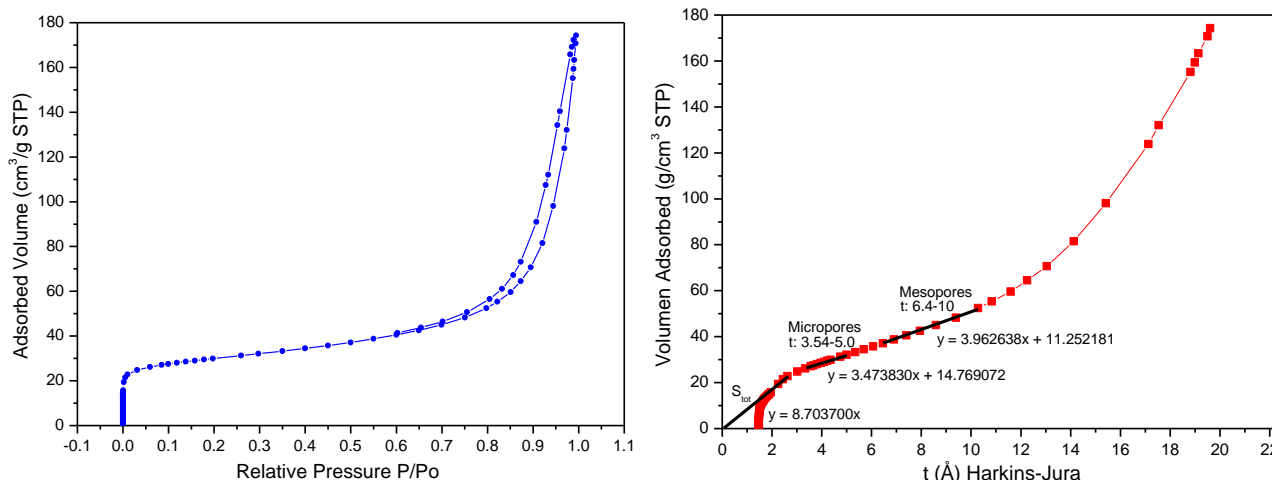


Figure 13. a) Nitrogen adsorption/desorption isotherms at 77 K on palygorskite sample from Torrejón El Rubio (Cáceres), and b) t-plot treatment of the adsorption branch

The pore size distribution was calculated from the nitrogen desorption isotherm by different methods. According to the IUPAC nomenclature (1972), pores are classified according to size into three categories: micropores (pore diameter < 2 nm or 20 \AA), mesopores (pore diameter $2-50$ nm or $20-500 \text{ \AA}$) and macropores (pore diameter > 50 nm or 500 \AA). Nitrogen adsorption-desorption isotherms determines usually pores in the pore diameter range between 15 \AA and 3000 \AA . The BJH method was used for reducing isotherm data between about $0.05 P/P_0$ and saturation, i.e., in the mesopore and low macropore size range (Figure 14a). However, in this work data were also obtained in the ultra low-relative pressure (<0.07) region (micropores), which were analysed by using the Horvath-Kawazoe (HK) and the non-local density functional theory (NL-DFT) methods. The DFT method produces the complete micropore, mesopore and macropore pore size distributions (Figure 14b) and does not require thickness models, i.e., the DFT method applies over the complete range of the isotherm and is not restricted to a confined range of relative pressures or pore sizes (Webb and Orr, 1997).

According to the pore size distribution obtained by the BJH method, four pore size families were found in this palygorskite: one family (4.2%) in the macropore range ($>500 \text{ \AA}$) with a sharp maximum at 582 \AA (58.2 nm) pore diameter, two pore size families in the mesoporous range with maximums at 292 \AA (53.6%) and 91.7 \AA (37.1%); and a family in the microporous range. This microporous range (Figure 14b) was analysed by the NL-DFT method according to the Tarazona model (cylindrical pore geometry), which reproduces the families observed by the BJH method and defines two pore families below 20 \AA (micropore range). One centered at 11.6 \AA (116 nm) and a biggest one centered at 5.2 \AA (52 nm). This last value is in good agreement with the idealized crystallographic structure of palygorskite and the dimension of its tunnels. The differential pore-volume plot of palygorskite obtained from the Horvath and Kawazoe method gave only a sharp maximum at 4.2 \AA . Therefore, the DFT method following the Tarazona model is very useful for sizing this type of materials with substantial micropore volume. However, this model doesn't describe the complete range of pore sizes, only up to 387 \AA . Trying to reproduce the complete pore range from micropores to macropores, the NLDF with density independent weights model (Infinite Slit_NDFT) was used, which assume a slit pore geometry (Figure 15). It is interesting to note that with this DFT model, the mesoporous and macroporous range is only better described than using the Tarazona model, although the two main families in the microporous range are pointed out.

Furthermore, it is interesting to compare the surfaces areas (SA) obtained with both the BJH and the DFT methods. In the BJH method, where only the mesoporous range is described, a total external surface area of around $63 \text{ m}^2/\text{g}$ is obtained. Therefore, the maximum SA is development inside the intracrystalline microporosity. In the Tarazona NLDF model the maximum peak at 5.2 \AA gives a SA of around $212 \text{ m}^2/\text{g}$, which is similar to the total surface area obtained by

water adsorption ($257 \text{ m}^2/\text{g}$). At the end of the main peak (at 6.2 \AA) the SA is $264 \text{ m}^2/\text{g}$. The difference between the surface area developed between the structural porosity and the total microporosity (up to 20 \AA) is $43 \text{ m}^2/\text{g}$, and between the structural porosity and the total textural porosity (i.e., from 6.2 \AA to 500 \AA) is $76.8 \text{ m}^2/\text{g}$. This means that the external surface area is mainly contributed by the structural or intracrystalline porosity. The interfiber micro- and mesoporosity as well as macroporosity (aggregation of bundles) are almost insignificant when the SA values are compared to that obtained from the structural porosity. These data are in agreement with the t-plots data (Table 2). Besides, the surface area obtained with the Infinite Slit_NDFT model, where only mesopores and macropores are better described, the total surface area developed is lower (of $109 \text{ m}^2/\text{g}$) than that obtained with the Tarizona NDFT method ($340 \text{ m}^2/\text{g}$). This lower value is similar to that obtained by the BET method.

Therefore, the high surface area and porosity of this palygorskite are the result of different porosities: micro-, meso- and macro-porosity. There are two types of microporosity: structural or intracrystalline microporosity due to the staggered arrangement of talc ribbons in the fibers (with a pore width of 5.2 \AA); and an interfiber microporosity (with a pore width of 11.6 \AA). The mesoporosity due to interfiber mesopores or to the defect in the arrangement of the structural units, is mainly characterized by pores with a pore size of 292 \AA . A low amount of macropores were also detected with a pore size of $500\text{-}582 \text{ \AA}$ and 1175 \AA . Therefore, the textural porosity of this fibrous material is composed by the interfiber microporosity, the mesoporosity and the macroporosity (Grillet et al., 1988; Suárez and García-Romero, 2012).

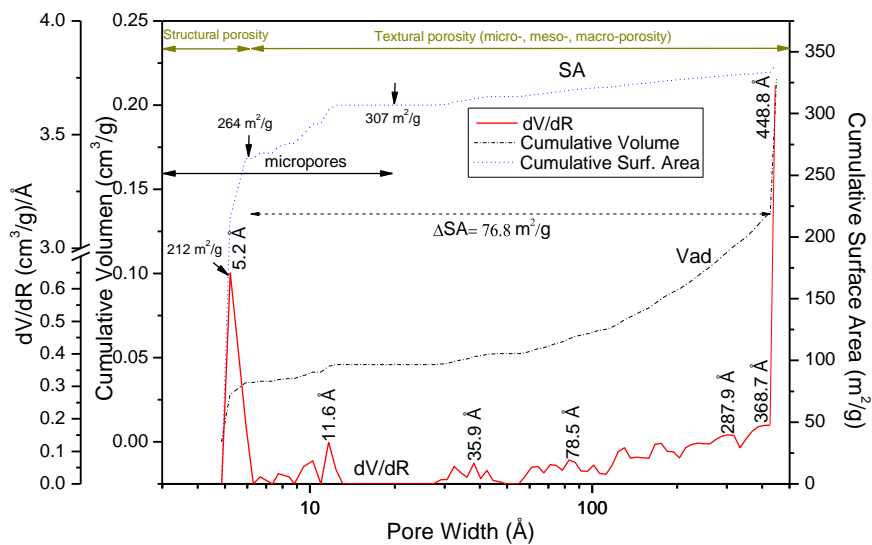
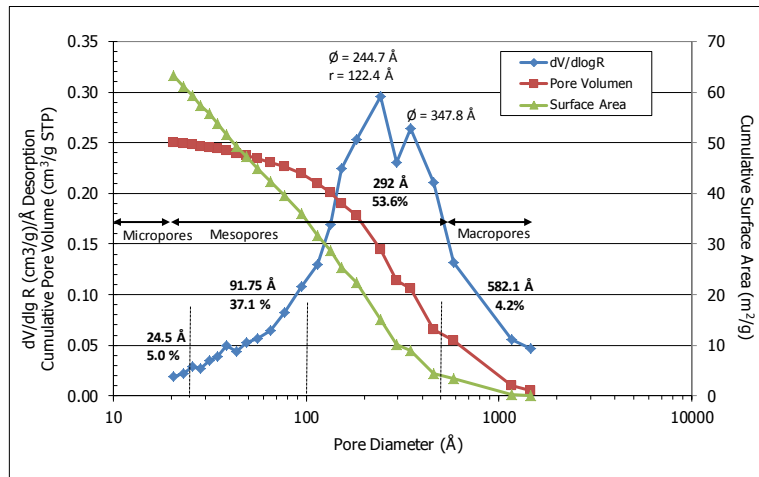


Figure 14. Pore size distribution obtained by the BJH method for macro- and mesopores and by the DFT method (Tarazona model) for micropores in palygorskite sample from Torrejón el Rubio (Cáceres)

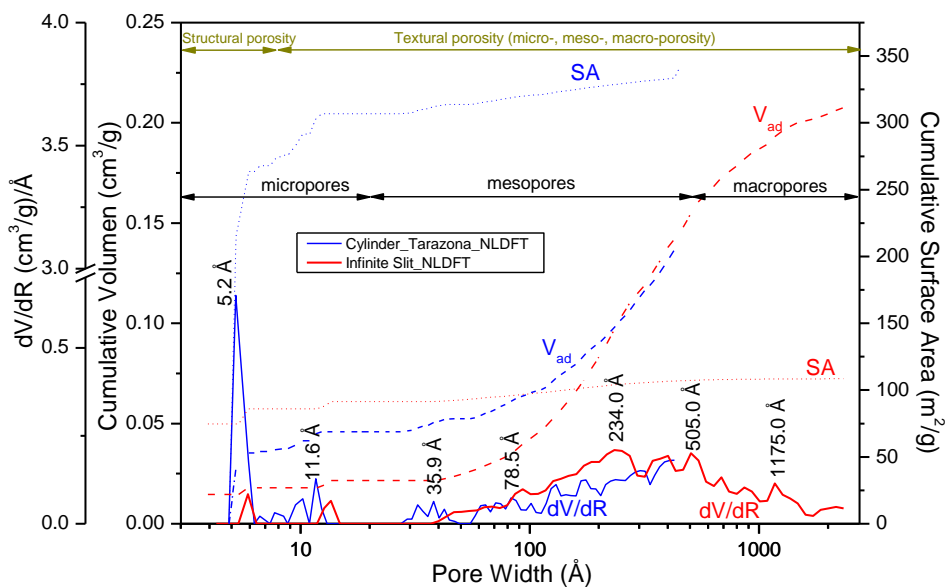


Figure 15. Pore size distribution obtained by the DFT method for micropores in palygorskite sample from Torrejón el Rubio (Cáceres) according to the Cylinder Tarazona NLDFT and the Infinite Slit NLDFT models

4.2 Mineralogical analysis and Crystallographic structure by XRD

The main and accessory minerals in the palygorskite samples from Torrejón el Rubio were analysed by XRD on the total and $< 2 \mu\text{m}$ size fractions.

The analysis of the total mineralogy of the rock reveals the following main mineralogical association (Figure 16, Table 1): palygorskite (57 wt.%), quartz (26 wt.%), K-feldspar (12 wt.%), muscovite/illite (2 wt.%), chlorite (1 wt.%), cristobalite (1 wt.%), barite (1 wt.%), and traces of ilmenite. Calcite/dolomite was not found due to they seem to appear only in the discontinuous carbonatic levels (Fernández-Macarro and Blanco-Sánchez, 1990).

The nature of the clay minerals was also analysed according to the (060) reflection and the oriented aggregated (Figure 17). XRD patterns of the air-dried oriented aggregates show strong diagnostic (110), (200), and (400) palygorskite peaks at 10.34 \AA , 6.35 \AA and 3.18 \AA , respectively (Figure 17). The presence of muscovite/illite and chlorite were indicated by their main d_{hkl} reflections. Upon glycolation, the palygorskite peaks did not shift, as well as the 001 smectite peak did not shift to 17 \AA , indicating that smectite is not present in the sample. Kaolinite was not detected (which was also confirmed by the FTIR spectra). Therefore, the clay fraction (Table 1) is dominated by palygorskite (96 wt.%), with small amounts of detritic components: illite/muscovite (2 wt.%) and chlorite (1 wt.%).

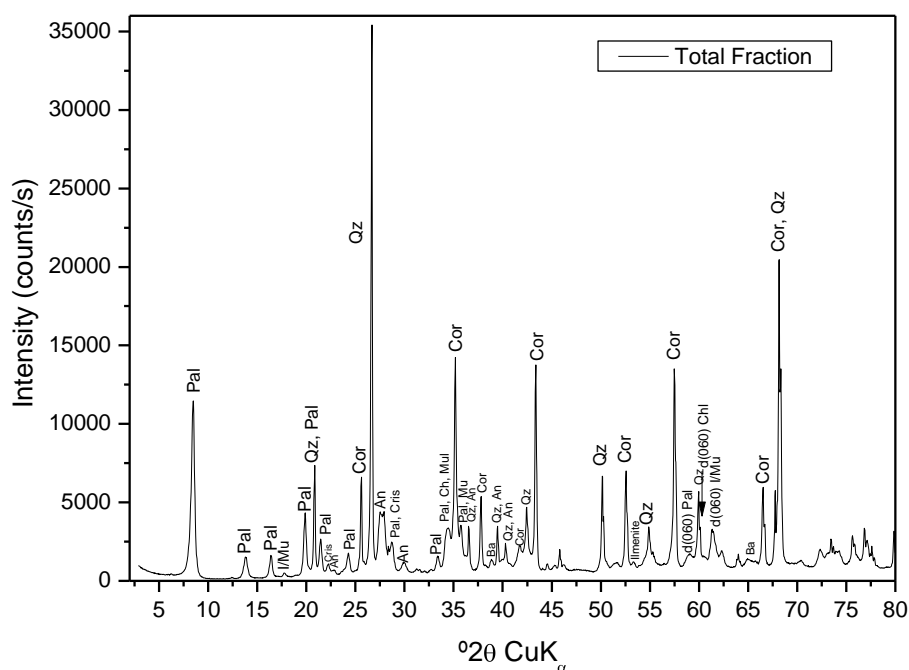


Figure 16. XRD pattern of the raw clay mineral from La Cierva deposit (Torrejón el Rubio, Cáceres). (Pal: palygorskite, I/Mu: illite/muscovite, Cris: cristobalite, An: anorthite, Chl: chlorite, Qz: quartz, Cor: corundum, Ba: Barite)

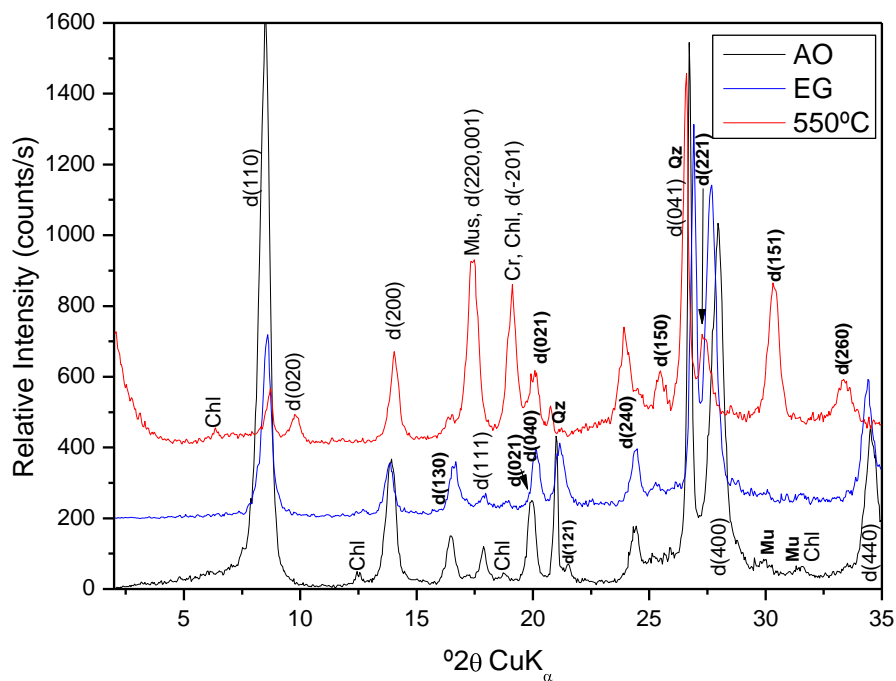


Figure 17. XRD patterns of the < 2 μm clay mineral fraction (AO: orientated aggregate; EG: ethylene glycolated; 550°C: heated at 550°C) from palygorskite from Torrejón el Rubio (Cáceres). d_{hkl} reflexions of palygorskite are shown; Cr: cristobalite, Chl: chlorite, Mu: Illite/muscovite

Regarding the structural model and crystallinity for palygorskite, the refinement unit cell calculations were made by fitting the X-ray diffraction profile by using the X Powder program, after correction of the 2θ angle by using α -corindon as internal pattern, Caglioti FWHM adjustments and removing the $K\alpha_2$ stripping.

The a ($\sim 12.778 \text{ \AA}$) and b ($\sim 17.869 \text{ \AA}$) parameters of the unit cell were calculated by using the d_{200} ($\sim 6.389 \text{ \AA}$) and d_{040} ($\sim 4.467 \text{ \AA}$) reflections. The 200 reflection was used to calculate the a or a $\sin \beta$ parameter ($\approx 2d_{200}$) if an orthorhombic (pbmn) or monoclinic ($C2/m$) phase are considered, respectively. The b parameter was calculated from the 040 reflection ($b \approx 4d_{040}$). c values are of much lower resolution by DRX, due to fibres are oriented along the c -direction and the XRD intensities are biased by this preferred orientation.

Regarding the palygorskite structure two possible space group models were proposed for palygorskite: monoclinic (Bradley, 1940; Drifts and Sokolova, 1971), orthorhombic (Preisinger, 1963), or a mixture of both of them (Christ et al., 1969), which suggested that the variations in symmetry reflect variations in chemical composition, mainly the octahedral Fe content (Weaver and Polland, 1973). Chisholm (1992) showed that some relative intensities of some reflections can be used for discrimination due to each form has some reflections that are not shown by the other. For example, the basal spacings 121 (4.25 \AA) and 321 (3.09 \AA) indicate the presence of orthorhombic palygorskite, while 021 (4.34 \AA) and strong 221 (4.13 \AA , overlapping the 310 of both forms) are indicative of monoclinic palygorskite. In this palygorskite from Torrejón el

Rubio, the 25-30° 2 θ range shows the 321 line (3.10 Å) characteristic of the orthorhombic form, whereas two lines close together near 400 (4.19 Å), which would indicate the presence of the monoclinic form, are non-existent. In the 19-23° 2 θ range, the 121 reflection (4.25 Å) is intense, whereas the 021 (4.33 Å) and strong 221 (4.13 Å) reflections are non-existent. Therefore, it seems that palygorskite from Torrejón el Rubio is orthorhombic with $\alpha \approx \beta \approx \gamma \approx 90^\circ$.

After unit cell refinements, by using the initial orthorhombic pbmn phase JCPDS file 881951 (Chisholm, 1992), the a, b, and c calculated parameters were: $a = 12.7763 \pm 0.0276$ Å, $b = 17.9211 \pm 0.0441$ Å and $c = 5.2013 \pm 0.0161$ Å, with $\alpha = \beta = \gamma = 90^\circ$ and a volume cell of 1190.92 ± 4.48 cm³.

According to Suárez et al. (2007), who studied the dependence of cells parameters on the octahedral composition by high-resolution X-Ray diffraction with synchrotron radiation, the nature of cations in octahedral positions influences in the a cell dimension, i.e., there is a dependency of the a-axis on the [VIAl] or [Mg+Fe³⁺], the d spacing for the 200 reflection ($a \approx 2d_{200}$) being a direct indicator of the aluminic versus magnesium nature of the palygorskite, i.e., their dioctahedral character. According to this work, the number of octahedral vacants for the palygorskite from Torrejón el Rubio, calculated as: $OV = 24.0047 - 3.6065 d_{200}$, would be of 0.97; i.e., there is one octahedral vacant. Besides, the VIAl content, calculated according to the relationship: $[VIAl] = 49.1617 - 7.4401 d_{200}$ (VIAl decreasing when $2d_{200}$ increases), would be of 1.63. Therefore, for the five octahedral positions per half unit cell present in the structure of the palygorskite, one octahedral site is vacant and 1.63 is occupied by VIAl.

Suárez et al. (2007) and García-Romero and Suárez (2010) classified palygorskites regarding its chemical composition and its relationship with d_{200} as: a) Palygorskite Type I or Ideal palygorskite: $[VIAl] > 1.95$ or $d_{200} < 6.35$ Å, i.e., similar contents of Al and Mg and negligible substitutions of Al by Fe³⁺ and/or Mg; b) Palygorskite Type II or Common palygorskite: $1.1 < [VIAl] < 1.95$ or $6.46 < d_{200} < 6.35$ Å. Although Al may be partially substituted, this palygorskite has dioctahedral character; c) Palygorskite Type III or Magnesian palygorskite: $[VIAl] < 1.1$ or $d_{200} > 6.46$ Å, i.e., the most trioctahedral extreme where octahedral cations are higher than 4 and the vacant M1 position is partially occupied; and d) Type IV or Aluminic palygorskite, the most dioctahedral extreme in which $Al^{3+}/Mg^{2+} > 1$ and $Mg^{2+} < 2$, octahedral cations being lower than 4. A category of Fe-rich palygorskite could be used when $Fe > Al$ in the different types described above, such as the Greek samples studied by Gionis et al. (2006), which can be classified as Fe-rich palygorskite Type II.

According to this classification, this studied palygorskite is a Type II Common Palygorskite with $[VIAl] = 1.63$ and $d_{200} = 6.388$, of dioctahedral character and showing partial substitutions of Mg²⁺ (or Fe) for Al³⁺.

The d_{100} basal spacing and other individual reflections of palygorskite (d_{200} , d_{040}) are broad because the presence of small grains, crystallites being inside these grains (peak widths are related to crystallinity and particle size). A crystallite grain size of 20 nm (200 Å) was obtained according to both the Scherrer and Warren-Averbach (Warren and Averbach, 1952) methods by using different order profiles (d_{hkl}) and pseudo-Voigt profiles for fitting.

4.3 Microstructural Analysis (SEM analyses)

The samples show the characteristic fibrous morphology when seen under the scanning electron microscopy (SEM). The fibers occur as bundles of rods consisting of sets of parallel fibers or as aggregates displaying a “bird-nest” texture. Size of fibers is quite variable, ranging from 1 to 10 μm length and 10 to 250 nm thick, occurring mainly in the form of crystal aggregates of individual fibres with a width size between 3 to 50 μm , the texture being very porous containing both mesopores and macropores.

Regarding to composition and mineralogy, apart from palygorskite, other main and accessory minerals were observed, such as quartz, ilmenite and barite. Apart from palygorskite, no other type of clay minerals was found.

4.4 Chemical analysis by FRX and SEM-EDAX analysis

The structural formula of the analysed palygorskite was determined from both chemical analyses obtained by XRF, on the $< 2 \mu\text{m}$ size particle fraction, and by SEM-EDX from isolated particles both on the total and $< 2 \mu\text{m}$ size particle fractions. The results are shown in Table 3. The structural formula was calculated on the basis of $\text{O}_{20}(\text{OH})_2$ per half unit cell (p.h.u.c.), i.e. 21 oxygens (Newman and Brown, 1987). The results are shown in Table 4.

Different authors have studied the chemical composition of palygorskites (e.g., Bradley, 1940; Galán and Castillo, 1984; Weaver and Pollard, 1973; Suárez and García-Romero, 2011). The most widely structural model accepted for palygorskite is that isomorphic substitutions occur both in tetrahedral and octahedral sheets, the sum of octahedral cations being between 3.45 and 4.33 (Drits and Sokolova, 1971) or between 3.76 and 4.64 (Newman and Brown, 1987). The ideal palygorskite have an octahedral sheet that contains mainly Mg, Al and Fe(III) with a R^2/R^3 ratio close to 1 and only four of the five structural positions occupied (2 Mg^{2+} and 2 Al^{3+}), where $R^2 = \sum\text{M(II)}$, $R^3 = \sum\text{M(III)}$ (Galán and Carretero, 1999).

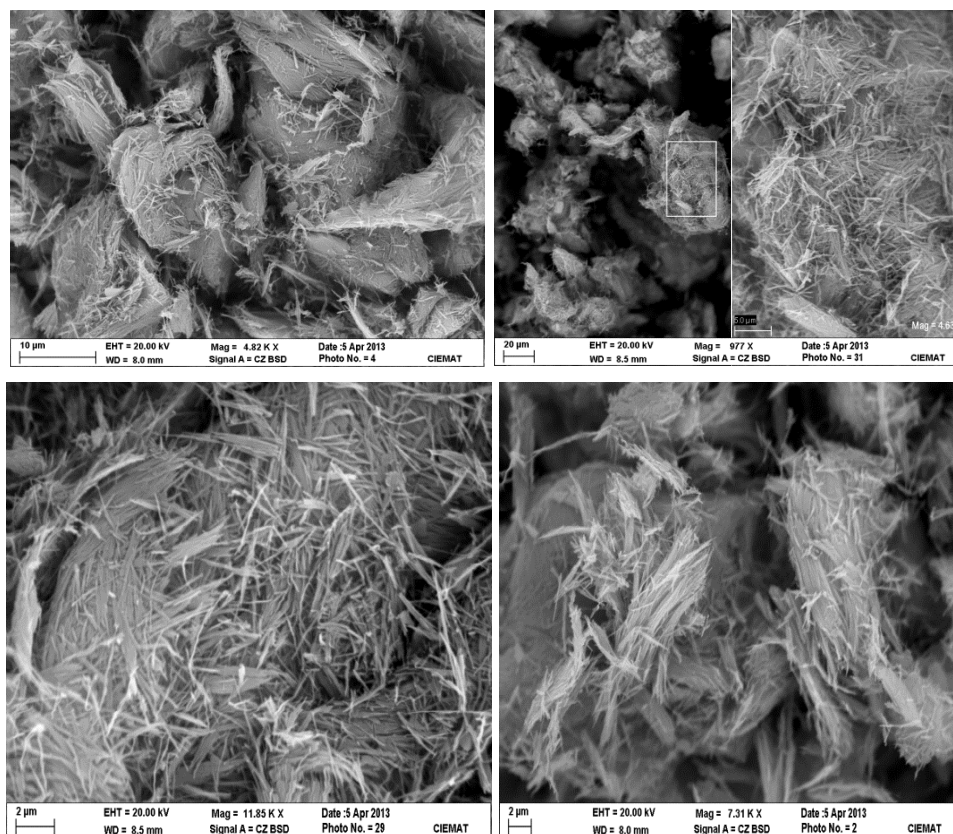


Figure 18. Scanning electron micrograph showing aggregates of palygorskite fibres

Table 3. Chemical composition of palygorskite from Torrejón el Rubio (Cáceres) obtained by FRX and SEM-EDX analyses and their comparison with other data obtained in the literature

Oxides (wt.%)	FRX <2 µm	SEM 1 <2 µm	SEM 2 <2 µm	SEM TF 1	SEM TF 2	1	2	3
SiO ₂	61.79	70.4	69.5	69.38	70.61	51.50	61.82	55.03
Al ₂ O ₃	10.54	12.65	12.52	12.14	13.33	10.03	13.62	10.24
Fe ₂ O ₃	3.73	4.90	4.41	4.31	4.33	2.36	1.87	3.53
FeO	--	--	--	--	--	0.52	--	--
MnO	0.22	-	1.74	--	--	--	--	--
MgO	9.07	11.06	11.44	12.15	11.11	12.28	8.56	10.49
Na ₂ O	0.09	-	-	--	--	0.12	0.13	--
K ₂ O	0.95	1.05	0.93	0.77	1.04	0.13	0.78	0.47
CaO	0.04	--	--	--	--	1.81	1.72	--
BaO	--	--	--	1.69	--	--	--	--
TiO ₂	0.53	0.42	0.35	--	--	--	1.66	--
SO ₃	0.05	--	--	--	--	--	--	--
LOI	12.19	--	--	--	--	--	11.14	--
Total	99.20	99.99	100.45	--	--	--	101.30	99.62
H ₂ O ⁻	--	--	--	--	--	7.36	--	9.73
H ₂ O ⁺	--	--	--	--	--	14.43	--	10.13

1: Galán and Castillo (1975); 2; Álvarez Estrada and Sánchez Conde (1967);

3: Bradley (1940)

Table 4. Structural formulae of palygorskite samples from Torrejón el Rubio (Cáceres) obtained by FRX and SEM-EDX analyses and their comparison with other data obtained in the literature

	Si	^{IV} Al	Στ	Tetrah. charge	^{VI} Al	Mg	Fe ³⁺	Ti	Mn	Σo	Oct. charge	Ca	K	Na	Interl. charge	Al/(Mg+Fe)	Al/Mg	R ³ /R ²
FRX	8.03	--	8.03	0.11	1.61	1.76	0.36	0.05	0.02	3.81	-0.30	0.01	0.16	0.02	0.19	0.76	0.91	1.11
SEM 1	7.93	0.07	8.00	-0.07	1.61	1.86	0.42	0.04	--	3.91	-0.08	--	0.15	--	0.15	0.71	0.87	1.09
SEM 2	7.86	0.14	8.00	-0.14	1.53	1.93	0.38	0.03	0.17	4.02	0.01	--	0.13	--	0.13	0.66	0.79	0.91
SEM TF1	7.90	0.10	8.00	-0.10	1.53	2.06	0.37	--	--	3.97	-0.16	--	0.11	--	0.26 ^(*)	0.63	0.74	0.92
SEM TF2	7.93	0.07	8.00	-0.07	1.70	1.86	0.37	--	--	3.93	-0.08	--	0.15	--	0.15	0.76	0.91	1.11
1	7.60	0.40	8.00	-0.50	1.34	2.70	0.33	--	--	4.37	-0.12	--	--	--	0.62	0.44	0.5	0.62
2	7.75	0.25	8.00	-0.25	1.76	1.60	0.18	0.16	--	3.69	-0.37	0.23	0.12	0.03	0.62	0.99	1.10	1.21
3	7.80	0.20	8.00	-0.20	1.51	2.22	0.38	--	--	4.11	0.11	--	0.09	--	0.09	0.58	0.68	0.85
TOR1	7.91	0.09	8.00	-0.09	1.48	2.25	0.37	--	--	4.10	0.05	0.01	0.02	--	0.04	0.54	0.63	0.79
TOR2	7.88	0.12	8.00	-0.12	1.43	2.28	0.38	--	--	4.09	-0.01	0.01	0.02	--	0.04	0.54	0.63	0.79

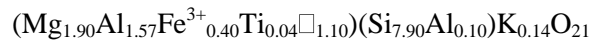
Στ: sum tetrahedral cations; Σo: sum octahedral cations; R²: Divalent cations; R³: Trivalent cations; ^(*) Ba=0.08; TOR1: from Suárez and García Romero (2006); TOR2: from García-Romero et al. (2010)

The M1 site has a trans-OH configuration and is the vacant octahedral site in these layer silicates (Serna et al., 1977). The two M2 sites display a cis-OH configuration with a pair of OH ions being shared between two adjacent octahedral. The two M3 sites have two water ligands and appear at the edges of the octahedral ribbons. The M3 (edge) sites are exclusively occupied by Mg and M2 (cis) sites can be occupied by Al, Fe³⁺, Fe²⁺, Mg and Ti. However, according to Heller-Kallai and Rozenson (1981) from Mössbauer studies, Fe³⁺ can occupy both M3 and M2 sites.

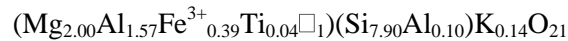
Palygorskite samples from the La Cierva deposit at Torrejón el Rubio have SiO₂ contents ranging between 61.8 to 70.6 wt.%. Al₂O₃ ranges between 10.5 and 13.3 wt.%, and MgO between 9.1 and 12.2 wt.%. All the samples analysed contain a high amount of Fe₂O₃ (3.7-4.9 wt.%), indicating that this studied palygorskite contains a higher amount of Fe(III) than the reference palygorskite sample from Attapulugus (Georgia, USA) according to Bradley (1940). Small amounts of Mn and Ti appear also at octahedral sites.

The calculated structural formulae indicate that most of the samples show a small ^{IV}Al substitution, generating a deficit of charge on the tetrahedral sites, except that obtained by FRX. This could be explained by a small amount of amorphous silica in the < 2 μm fraction as it will be shown in TG-DSC analysis, which is not seen in SEM analysed due to these analyses are performed on an isolated clay particles. These data are in agreement with Woessner (1989) who derived by MAS-NMR ²⁷Al spectra and ^{IV}Al/^{VI}Al relationship in the range of 0.12-1.15. However, Güven (1992) found that tetrahedral substitutions of Al for Si were negligible, all the Al being assigned to [6]-fold coordination in the PF1-1 palygorskite by means of the same

NMR technique. García-Romero and Suárez (2010) also found ^{IV}Al substitution for silica in samples from the same deposit. Besides, a slight higher amount of ^{VI}Al is observed regarding that work, potassium content being also higher. In XRF measurements, K content could be enhanced by the presence of 1 wt.% of muscovite/illite in the bulk samples due to this K contribution was not neglected. However, a similar K content is also measured in isolated palygorskite particles by SEM analyses. According to Table 4, the crystal-chemical formula of the palygorskite samples from La Cierva deposit belong to the dioctahedral Type II Common Palygorskite, with a predominant dioctahedral character and an average divalent to trivalent cation ratio R³/R² of 1.01, a Al/Mg ratio of 0.83, and a high amount of Fe (although Fe<<Al). The average chemical formula per half unit cell of the dehydrated palygorskite, on the basis of 21 oxygens and SEM analyses on < 2 μm fraction would be:



In order to attain the number of octahedral vacants to a value of one (see section 4.2), the chemical formula would be:



The excess of negative charges on tetrahedral and octahedral sheets is compensated by positive charge (+0.14 e/half unit cell) due to K (Ca and Na) interlayer cations. The CEC corresponding to the compensating cations charge ξ (+0.14 e/half unit cell) exhibited by the structural formula above can be calculated by the following equation (Mermut and Lagaly, 2001):

$$CEC = 10^5 \times \frac{\xi}{M}$$

where, M designates the molar mass (678.85 g for the dehydrated clay). The calculated value is 20.6 meq/100 g, which is not in agreement with the CEC data calculated with the Cu-Complex (see section 4.1). Therefore, the potassium content at interlayers may be overestimated, probably due to the presence of illite/muscovite particles. The corrected value will be of around 0.05 per half unit cell for 7 meq/100 g of CEC, which is in agreement for data obtained from TEM analyses by García-Romero and Suárez (2010). However, it is interesting to note that this value is obtained if the isomorphic substitution is only given in the octahedral sheet, i.e., if [^{IV}Si= 8.0]. Therefore, it is probably that in nature, there will be structures with both types of tetrahedral sheets with isomorphic substitutions and non- isomorphic substitutions of Al for Si. Thus, the excess of negative charges is compensated by 0.04 interlayer cations (+0.04 e/half unit cell for monovalent cations) or 0.14 interlayer monovalent cations (or +0.07 e/half unit cell for bivalent cations) if tetrahedral isomorphic substitutions doesn't exist or exist, respectively.

The ^{VI}Al content obtained of 1.57 is similar to that obtained in section 4.2 by using the a crystallographic unit cell parameter or the basal spacing d_{002} ($[^{VI}Al] = 1.63$), but higher than that obtained by García-Romero and Suárez (2010) ($[^{VI}Al] = 1.43$, $[^{VI}Mg] = 2.28$) and lower than that obtained by Alvarez Estrada and Sánchez Conde (1967) ($[^{VI}Al] = 1.76$, $[^{VI}Mg] = 1.60$).

The M2 sites linked to structural OH seem to be predominantly occupied at 98% by trivalent cations (78.5% Al^{3+} and 19.5% Fe^{3+}) and at 2.0% by tetravalent cations Ti^{4+} . On the basis of all octahedral cations occupation percentages determined herein and knowing that palygorskite octahedral sheet contains 10 charges per half-unit cell, a qualitative octahedral cation distribution for the palygorskite from Torrejón el Rubio was determined by considering 5 half units cells, where 10 M3 sites are all occupied by Mg^{2+} , 10 M2 sites are occupied by 8 Al^{3+} and 2 Fe^{3+} , and 5 M1 sites are vacant. If Ti^{4+} is included, the octahedral adjacent to the octahedral occupied with Ti^{4+} must be filled with a bivalent cation (Mg^{2+} or Fe^{2+}) for maintaining 10 charges. Galán et al. (1975) detected $^{VI}Fe^{2+}$ in palygorskite samples from the same deposit (Table 3), and therefore, Mg would only occupy M3 positions. In this configuration, different possibilities were proposed (Figure 19). For 20 half units cells, 40 M3 sites are all occupied by Mg^{2+} , 40 M2 sites are occupied by 32 Al^{3+} , 6 Fe^{3+} , 1 Fe^{3+} (or Mg^{2+}) and 1 Ti^{4+} , i.e. at 90% by trivalent cations (80% Al^{3+} and 15% Fe^{3+}), at 2.5% by bivalent cations Fe^{2+} and at 2.5% by tetravalent cations Ti^{4+} . Thus, the proposed ideal structure for the palygorskite from Torrejón el Rubio would be:



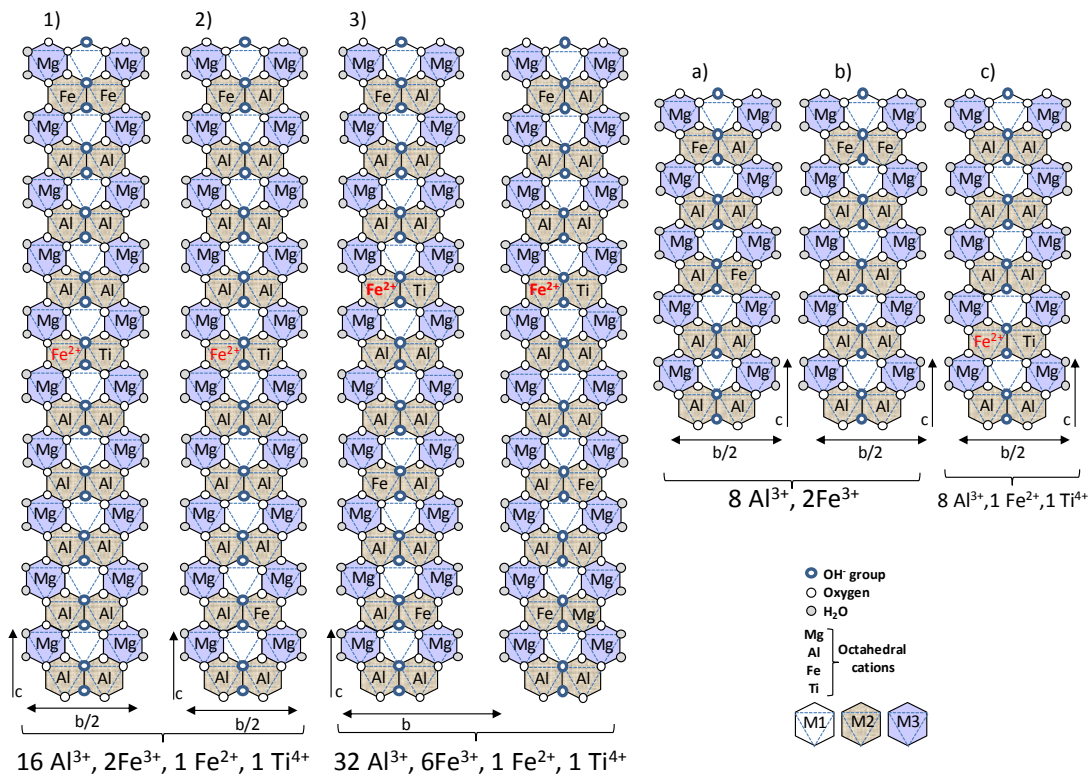


Figure 19. Different schematic distributions of cations in the octahedral sheet of palygorskite from Torrejón el Rubio based on: ten half unit cells (1 and 2); 20 half units cells (3); or of five half unit cells (a, b and c) (projection on the (010) plane), the distributions 3) and a) being possibly the most energetically favorable.

Idealized structural formula for distributions 1 and 2): $(\text{Mg}_{2.00}\text{Al}_{1.60}\text{Fe}^{3+}_{0.20}\text{Fe}^{2+}_{0.10}\text{Ti}_{0.10}\square_1)(\text{Si}_{7.90}\text{Al}_{0.10})\text{K}_{0.10}\text{O}_{21}$;
for distribution 3): $(\text{Mg}_{2.00}\text{Al}_{1.60}\text{Fe}^{3+}_{0.30}\text{Fe}^{2+}_{0.05}\text{Ti}_{0.05}\square_1)(\text{Si}_{7.90}\text{Al}_{0.10})\text{K}_{0.10}\text{O}_{21}$;
for distributions a) and b): $(\text{Mg}_{2.00}\text{Al}_{1.60}\text{Fe}^{3+}_{0.40}\square_1)(\text{Si}_{7.90}\text{Al}_{0.10})\text{K}_{0.10}\text{O}_{21}$;
and for distribution c): $(\text{Mg}_{2.00}\text{Al}_{1.60}\text{Fe}^{2+}_{0.2}\text{Ti}_{0.2}\square_1)(\text{Si}_{7.90}\text{Al}_{0.10})\text{K}_{0.10}\text{O}_{21}$

4.5 Thermal and calorimetric analysis

Thermogravimetric analyses coupled with differential scanning calorimetry were performed on bulk and $< 2 \mu\text{m}$ size fraction palygorskite samples. The mass losses (Figure 20) and heat flow changes (Figure 21) occurring during the heating of this mineral may be classified as: a) loss of water molecules (endothermic); b) dehydroxylation of the lattice (endothermic), c) collapse and transformation of the lattice (endothermic) and d) crystallization of new phases (exothermic). The sizes of the effects obtained for loss of water and dehydroxylation are not only proportional to the amount of water evolved but are dependent on the location of the water molecules and hydroxyl groups in the structure (Martín Vivaldi and Fenoll Hach-Ali, 1970; Jones and Galán, 1988).

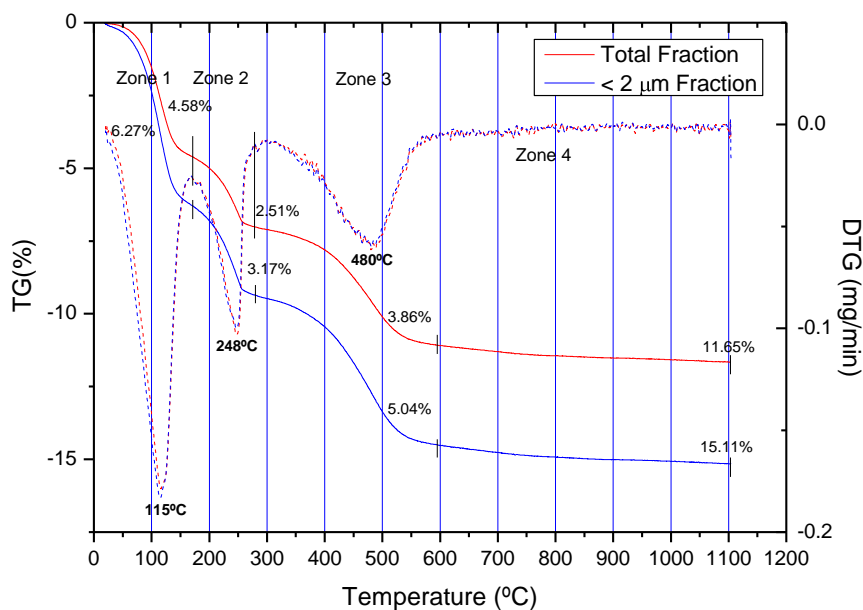


Figure 20. TG and DTG curves of palygorskite performed on the total and < 2 μm fractions

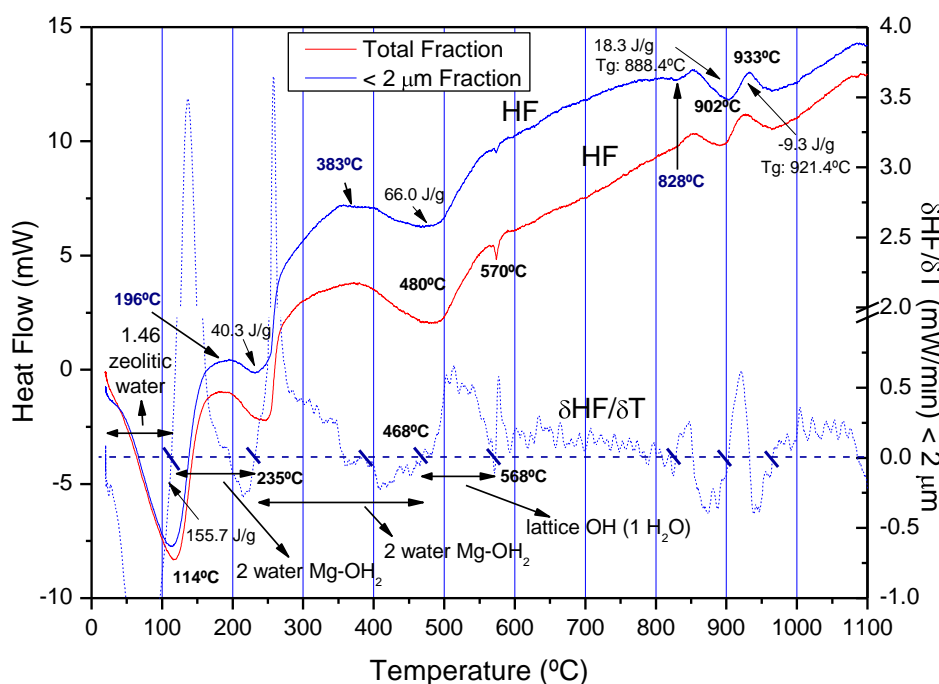


Figure 21. Differential Scanning calorimetric (DSC) curves of palygorskite performed on the total and < 2 μm fractions

The results obtained for both the total and the clay mineral fraction are similar. Two endothermic peaks are observed in the low-temperature region (20-300°C), related to the release of water molecules. The first peak, being larger, is located at 115°C and the second one is located at 248°C. They correspond to weight losses of 6.77% (20-200°C) and 3.04% (200-355°C), respectively on the < 2 μm fraction sample (Table 5). These two peaks are attributed to

loss of held physically water: adsorbed on the surface (physisorbed) and inside the channels (zeolitic water), and to some bound water (weakly bound to the Mg octahedral cations), respectively (Prost, 1975; Serna et al., 1975). The zeolitic water (and of course, the adsorbed water) depends on the relative humidity (R.H.), and therefore, the amount of this water changes from one sample to another (Table 5). The heat associated to these endothermic peaks is of 156 and 40 J/g, respectively (Figure 21).

In the temperature range 300-600°C, an endothermic effect appears which is associated to a large and asymmetric peak located at 480°C. The mass loss of 4.54% is related to the release of : a) bound water (Mg-coordinated OH₂ at M3 octahedral sites), or b) to the remaining coordinated water at M3 sites bounded with a higher energy together with water from hydroxyls groups at M2 octahedral sites (Martín Vivaldi and Cano Ruiz, 1956; Huggins et al., 1962; Frost and Ding, 2003). The heat associated to this endothermic peak is of 66 J/g.

In the high-temperature region (800-1100°C), the DTG curves show insignificant mass changes above 650°C. However, the DSC curves (Figure 21) show the neoformation of different phases. Endothermic effects immediately followed by an exothermic indicate a structural rearrangement as suggested by Huggins et al. (1962).

The endothermic peak located at 570°C is assigned to the transformation of low to high Quartz. This peak is observed in the total fraction but also, although in much lower quantity, in the < 2 µm size fraction. Therefore, some colloidal silica is present after obtaining this clay fraction. The exothermic peak at 828°C (Figure 21) could be related to the recrystallization of quartz to tridimite or to the destruction of the palygorskite anhydride structure with the crystallization of a Mg-Al-silicate phase, such as cordierite (Mg₂Al₄Si₅O₁₈), with high quartz structures (Kulbicki, 1959; Hirsiger et al., 1975; Bayram et al., 2007).

The endothermic effect located at 902°C is due to the destruction of the amorphous structure and the exothermic peak located at 933 °C is concerned to the formation or recrystallization of clinoenstatite and β-cristoballite (Kulbicki, 1959; Preisinger, 1963; Hirsiger et al., 1975). The variation of the size in this latter peak may be due to the variation in the Mg:Al ratio. When this ratio is smaller than one; i.e. for aluminium-rich members of the series, the temperature range of stability is very small, whereas for Mg-rich members the temperature range of stability of clinoenstatite is very wide (Kulbicki, 1959).

According to the results obtained in Table 5, the total amount of water molecules lost is 7 molecules, whereas for an ideal palygorskite is 9 water molecules. Therefore, there is a deficit of 2 water molecules, i.e., there is no agreement between the water percentages calculated experimentally and those derived from the Bradley model, unless this deficit of water can be related to the zeolitic water which depends on the environmental relative humidity. It must be

taken into account that this palygorskite was dried during grinding and sieving. Thus, according to calculations from TG-DSC curves (Figure 20 and Figure 21) for the palygorskite from Torrejón el Rubio (Table 6), there would be 1.69 water molecules as zeolitic water (from 20 to 114°C), 4 water molecules associated to Mg²⁺ cations at M3 octahedral sites (from 114 to 468°C), and 1 water molecule associated to hydroxyls from octahedral cations at M2 sites (from 468 to 568°C). Therefore, the bound water would be released through the three typical stages or zones of the TG curve; not only between 200 and 400°C but also below 200°C and above 355°C. The loss of coordination water starts at 114°C when zeolitic is completely lost and ends when hydroxylation water begins to be lost at around 468°C, i.e., half water coordinated or crystalline water is lost between 114 to 233°C, and the remaining 2 water molecules per Mg²⁺ at M3 octahedral sites (Mg-OH₂) are lost between 233 to 468°C. Therefore, all zeolitic water and one half of the coordination water is lost from around 20 to 250°C. This is in agreement with the results of Van Scoyoc et al. (1979) who found that the four molecules of coordinated water are lost at two stages: a) from 100 to 300°C and b) from 300 to 500°C. At 120°C half of the coordinated water (two water molecules) is removed, and after heating at 300°C, the ~65% of the coordinated water is removed. Continued heating of palygorskite to temperatures of 400 and 500°C results in loss of the remaining coordinated water and the structural hydroxyls.

Table 5. Water losses (%) of the Palygorskite from Torrejón el Rubio (Cáceres) compared with those from Attapulugus (USA) and an ideal palygorskite

Types of waters	Torrejón el Rubio ⁽¹⁾ (Spain)	Attapulugus (USA) ⁽²⁾	Ideal palygorskite ⁽³⁾	
Zeolitic water: < 200°C ⁽⁴⁾	6.77 % (3.16 molecules)	< 200°C: 10.8 %	4 molecules	8.5 %
Bound water: 200-355°C ⁽⁴⁾	3.04 % (1.42 molecules)	250-400°C: 3.6 %	1+3 molecules	8.5 % (2.1+6.4)
Hydroxyl water: 355-568°C ⁽⁴⁾	4.54 % (2.12 molecules)	> 400°C: 4.2 %	1 molecule	2.0 %
Total water	15.13 % (7.06 molecules)	18.6 %	--	19.0 %

⁽¹⁾ PM[(Mg_{1.90}Al_{1.57}Fe³⁺_{0.40}Ti_{0.04}f_{1.10})(Si_{7.90}Al_{0.10})K_{0.14}O₂₀(OH)₂(OH₂)₄·4H₂O] = 840.98 g

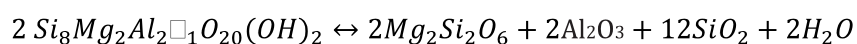
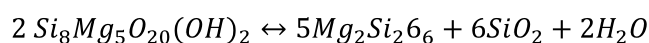
⁽²⁾ Weaber and Pollard (1973); ⁽³⁾ Ideal palygorskite: Si₈Mg₅O₂₀(OH)₂(OH₂)₄·4H₂O (Bradley, 1940)

⁽⁴⁾ Temperature limits defined by the first derivative of the heat flow signal

Table 6. Temperature ranges for the types of water in the Palygorskite from Torrejón el Rubio (Cáceres)

Types of waters	Zeolitic water: 20-114°C	One half of coordinated water: 114-235°C	Two half of coordinated water: 235-468°C	Hydroxyl water: 468-568°C	Si-OH groups: 568-1100°C	Total water
Mass loss (%)	3.63	4.29	4.30	2.13	0.77	15.13
Water molecules	1.69	2	2	1	0.36	7.06

The dehydroxylation water (constitution water) is lost between 468 and 568°C, the DSC and DTA peak being overlapped with the loss of the two half coordinated water. Besides, a remaining mass loss of about 0.3 water molecules (0.62 %) is lost between 600 to 900°C (0.77% up to 1100°C), which could be due to the elimination of water from Si-OH groups, which are broken Si-O-Si bonds at terminal silica tetrahedral on the ribbons that compensate their residual charge by accepting a proton or hydroxyl, and probably generated during the loss of adsorbed water on the external surfaces of the particles (Serratosa, 1979; Ahlrichs et al., 1975; Serna et al., 1977). The deshydroxylation of palygorskite cannot occur between 800 and 900°C because no mass loss is observed in the DTG curves. Therefore, the deshydroxylation of the palygorskite anhydride occurs at lower temperatures, as it was pointed out. The deshydroxylation of the palygorskite anhydride to give clinoestatite can be represented by the following reactions:

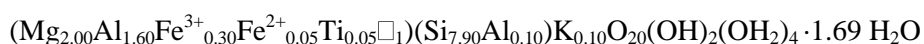


According to the DSC curves (Figure 21), small endothermic shoulders (detected by the $\partial HF/\partial T$ signal) appear at 193°C, 383° and 828°C. These shoulders could be due to changes in the palygorskite structure during the loss of water associated to Mg^{2+} at M3 sites and SiOH groups. As it was observed, bound water molecules are lost in two steps accompanied by reversible structural change similar to sepiolite (Prost, 1975; Serna et al., 1975; Kiyohiro and Otsuka, 1989). In the first dehydration step, during the loss of the first one half coordinated or crystalline water (193°C), the structure transforms uniformly to a more stable folded structure (where opposing ribbons being approaching each other by alternating rotation of continuous structural units around the lines of the linking oxygen atoms, Figure 6a), the rest of water being entrapped in the folded nanochannels. In the second dehydration step (383°C), the rest of bound water (the two half of coordinated water), diffuses out the crystal through the folded channels. The rate of losing the remaining bound water in this second step, as detected in DSC signals, is slower due to the hindrance of these folded channels on the diffusion process, increasing consequently the temperature of hydration. At the end of this second dehydration process the palygorskite is transformed into a palygorskite anhydride (Figure 6b).

There is a disagreement between different authors about if the palygorskite structure changes (altering the unit cell dimensions) only during the loss of one half of coordinated water (Preisinger, 1963; Hayashi et al., 1969) or in all steps of dehydration (Hirsiger et al., 1975; Van Scoyoc et al., 1979; Post and Heaney, 2008). In this work it seems that the two dehydration steps of the palygorskite related to bound water ($Mg-OH_2$) are correlated to structural changes. It seems that at 193°C the folding of the structure begins to occur with the loss of the one half

coordination water, and at 383°C the structure begins to be changed into palygorskite anhydride, being this transformation completed at 468°C. From 828°C the anhydride structure starts to be transformed to other amorphous structures. According to different authors, rehydration after heating of palygorskite to the unfolded structure is possible, even when the reincorporation of both coordination and structural hydroxyls is needed; on the contrary of sepiolite in which rehydration has not proceeded beyond the deshydroxylation temperature. Furthermore, the textural and crystallochemical changes in the palygorskite as a result of the thermal treatments are associated with variations in the micropore system and the surface area (Figure 12). As a consequence of folding, the channel volume is lost and important changes in surface topography (decreasing the surface area) take place (Serratosa, 1979).

The structural formula of hydrated palygorskite from Torrejón el Rubio calculated on the basis of 21 oxygens per unit cell and the experimental amounts of the different amounts of water would be:



In this formula, there is only a deficiency of zeolitic water. There are 1.69 water molecules of zeolitic water instead of 4 per crystal-chemical formula inside the nanochannels.

4.6 Octahedral sheet composition by FTIR analysis

The characteristics vibrations in a IR spectra can be used for determining (Blanco et al., 1989): a) the vibration of structural hydroxyl groups and those of water (physisorbed, zeolitic and coordinated), b) vibrations of Si-O from the tetrahedral sheet with possible replacement Al for Si, and c) vibrations of the octahedral cations (Me-O vibrations, where Me represents Mg, Al, Fe, etc.). Therefore, the octahedral sheet composition determined by chemical analyses can be supported by IR spectroscopy in the near and middle frequency regions (Frost et al., 2001; Gionis et al., 2006). The occupancy of the three octahedral sites (M1, M2 and M3) by Mg, Al and Fe can be resolved by the OH-overtone spectra in the NIR range, i.e, NIR can separate the OH from H₂O modes (Gionis et al., 2006; 2007; Chryssikos et al., 2009; Stathopoulou et al., 2011).

In the near IR region (9500-4000 cm⁻¹), three different regions can be distinguished (Figure 22). In the 7300-6000 cm⁻¹ range, attributed to the first overtones of the hydroxyl (O-H) stretching mode, several sharp features are superimposed with a broad and complex envelope of H₂O overtones. Three well-defined features (M2M2OH overtone triplet) are observed at 7059 cm⁻¹

(overtone $2\nu_{\text{OH}}$ of the dioctahedral structure AlAlOH -stretching mode), 6998 cm^{-1} (dioctahedral $2\nu_{\text{AlFe}_3+\text{OH}}$ or H_2O bound to Al or Mg) and 6939 cm^{-1} ($2\nu_{\text{FeFeOH}}$). The FeFeOH band is shifted from a theoretical value of 6928 cm^{-1} due to a partial dehydration of the sample (Gionis et al., 2006, 2007). The bulk fraction shows also a peak at 7142 cm^{-1} . A possible overtone at 7252 cm^{-1} due to SiOH groups is not observed. Besides, trioctahedral ribbons identified by the Mg_3OH overtone (M1M2M2OH) at 7214 cm^{-1} (Gionis et al., 2007) are not observed. This is confirmed by the second-derivative NIR spectra.

At intermediate frequencies ($5500\text{-}4800\text{ cm}^{-1}$ region), absorption in the NIR is dominated by the water stretching-deformation combination modes of the three types of water: physisorbed, zeolitic and coordinated to edge cations. The samples (bulk and $< 2\text{ }\mu\text{m}$ fraction) show a triplet of sharp bands at 5240 cm^{-1} ($\nu+\delta\text{ H}_2\text{O}$, interaction of coordinated and zeolitic water), and 5196 cm^{-1} ($\nu+\delta\text{ H}_2\text{O}$, interaction of coordinated and zeolitic water).

Finally, in the region $4800\text{-}4000\text{ cm}^{-1}$ the combination modes of the stretching and deformation of the structural hydroxyl groups (M2-M2OH) are resolved. There is a strong mode at 4503 cm^{-1} ($\nu_{\text{OH}}+\delta_{\text{AlAlOH}}$). Weaker sharp bands are observed at 4433 cm^{-1} ($\nu_{\text{OH}}+\delta_{\text{AlMgOH}}$), and 4358 cm^{-1} ($\nu_{\text{OH}}+\delta_{\text{Fe}_3+\text{Fe}_3+\text{OH}}$).

In the MIR region (Figure 23), two main regions can be distinguished: the stretching vibration ($4000\text{-}2000\text{ cm}^{-1}$) region, and the bending or deformation region ($2000\text{-}350\text{ cm}^{-1}$).

In the stretching vibration region of the hydroxyl groups, strong absorption is found from 3800 to 3000 cm^{-1} where three bands appear, with maxima at about 3614 , 3584 and 3550 cm^{-1} . The sharpest band at 3614 cm^{-1} is attributed to stretching vibrations of OH joined to two Al^{3+} cations in octahedral coordination (Al_2OH) and to a stretching vibration of the OH of water coordinated to the Mg of the fibre edges (Blanco et al., 1989). The band at 3584 cm^{-1} is attributed to (Al,Fe)-OH or to (Al,Mg)-OH (Serna et al., 1977, Chachi et al., 2002). However, according to the chemical analyses obtained for the palygorskite from Torrejón el Rubio, this band only can be attributed to a (Al,Fe)-OH vibration due to Mg cannot be in central positions of the octahedrons, i.e., in M2 positions. The band at 3550 cm^{-1} is attributed to (FeFe-OH) vibrations because, for the same reason, the (Fe,Mg-OH) vibration doesn't exist. The absorption band with maxima at 3382 and 3267 cm^{-1} , with an asymmetric absorption at lower frequencies, corresponds to the vibrations of physisorbed water (surface and zeolitic) which interact each other because of the hydrogen bridges. A peak at about 3700 cm^{-1} , attributed to the Si-OH groups situated at the rupture points of the Si-O-Si bonds of the tetrahedral sheet, is not observed.

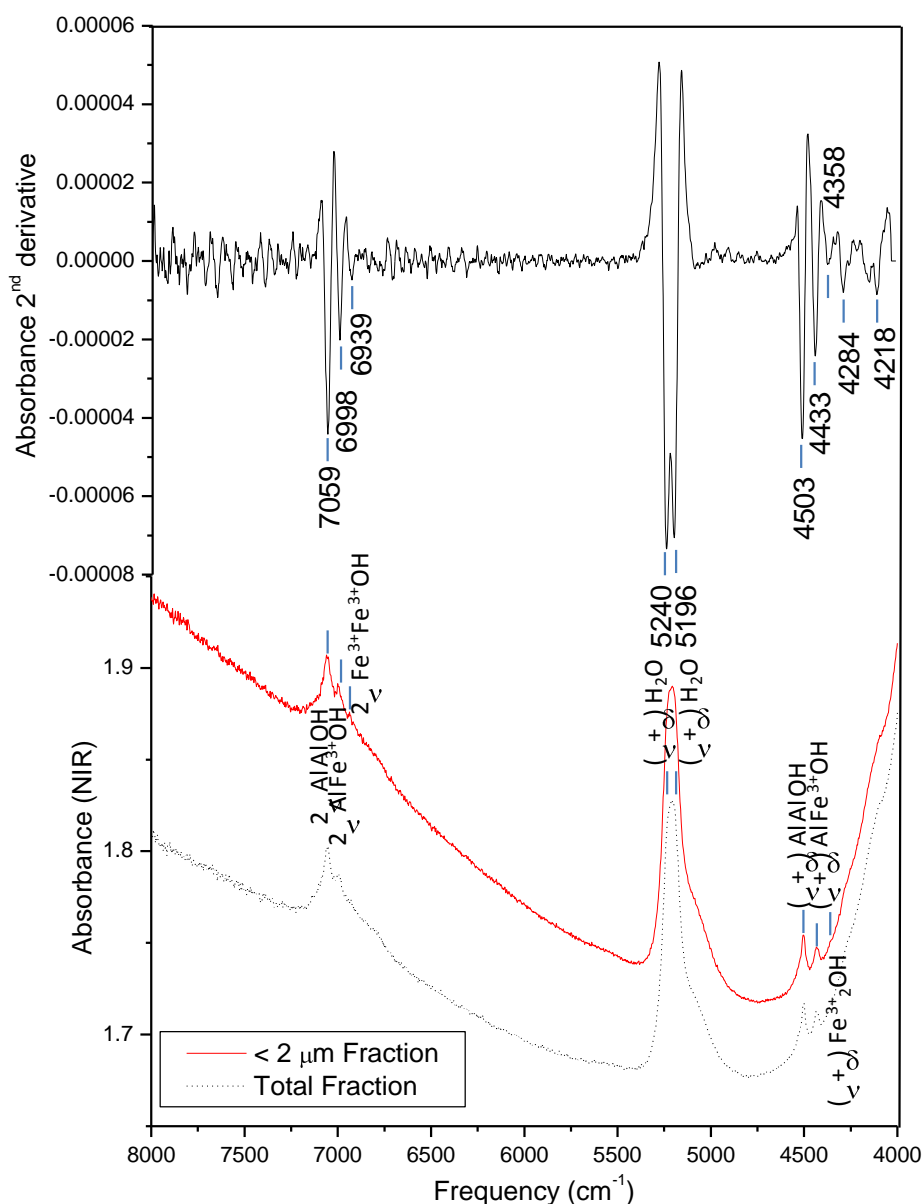


Figure 22. NIR spectra of the palygorskite from Torrejón el Rubio (Cáceres) and its second derivative calculated with the Savitzky-Golay algorithm with 15-point smoothing

The bending vibrations of H₂O appear in a strong band at 1660 cm⁻¹ where the deformation vibrations of coordinated water overlap with those of the zeolitic and surface water, as it is observed in the second derivative MIR spectra (Figure 23).

Regarding the bending band of the structural hydroxyls in the plane, the isomorphic replacements can produce either a widening of the characteristic vibration bands at about 50 cm⁻¹ or a splitting of the original band, in the case of highly ordered structures (Hayashi and Otsuka, 1969; Blanco et al., 1989; Gionis et al., 2006). In these situations is possible to distinguish the following adsorption bands: AlAlOH (~915-950 cm⁻¹), (Al, Fe)-OH (~890-860 cm⁻¹), (Mg,Al)-OH (~840-800 cm⁻¹), FeFeOH and/or MgFeOH (~800 cm⁻¹). In the MIR spectra

(Figure 23), three bands corresponding to isomorphic substitutions can be observed. In the palygorskite from Torrejón el Rubio the AlAlOH band appears at 912 cm^{-1} , the band (Al, Fe)-OH at 868 cm^{-1} , and the FeFeOH at 802 cm^{-1} . The existence of a MgFeOH band is ruled out due to the chemical analysis of the sample. A band at around 685 cm^{-1} characteristic to the bending band of OH joined to the Mg in trioctahedral coordination Mg_3OH (M1M2M3-OH) is not detected.

Regarding the vibrations corresponding to the silicate anion different bands are observed: the stretching of the perpendicular Si-O with absorption at 1195 cm^{-1} , the stretching of the bond in the plane with two strong bands at 1035 and 985 cm^{-1} (the latter being the most intense). The bendings in the plane give rise to two strong bands at about 518 and 486 cm^{-1} due to the octahedral cations.

With respect to the vibrations of the octahedral cations, there is a doublet at 1120 and 1092 cm^{-1} which corresponds to the stretching vibration of Al-O, which confirms the classification of an aluminic palygorskite. Stretching bands at 740 and 660 cm^{-1} indicates that Al not only performs replacement in the octahedral sheet (bands at 912 and 868 cm^{-1}) but also in the tetrahedral one, replacing Si. Other bending vibrations of the octahedral cations are found between 600 and 400 cm^{-1} , overlapping with the tetrahedral cations and OH groups (Blanco et al., 1989; Farmer, 1974).

Therefore, the dioctahedral character of the Palygorskite from Torrejón el Rubio is consistent with the set of assignments established for the deformation, stretching, combination and overtone bands of dioctahedral AlAlOH, $\text{AlFe}^{3+}\text{OH}$ and $\text{Fe}^{3+}\text{Fe}^{3+}\text{OH}$ species. The M3 positions would be only occupied by Mg^{3+} , whereas M2 position would be only occupied by Al and Fe. Apart from replacing Mg at octahedral positions, Al replaces Si in the tetrahedral ones, as observed by chemical analyses.

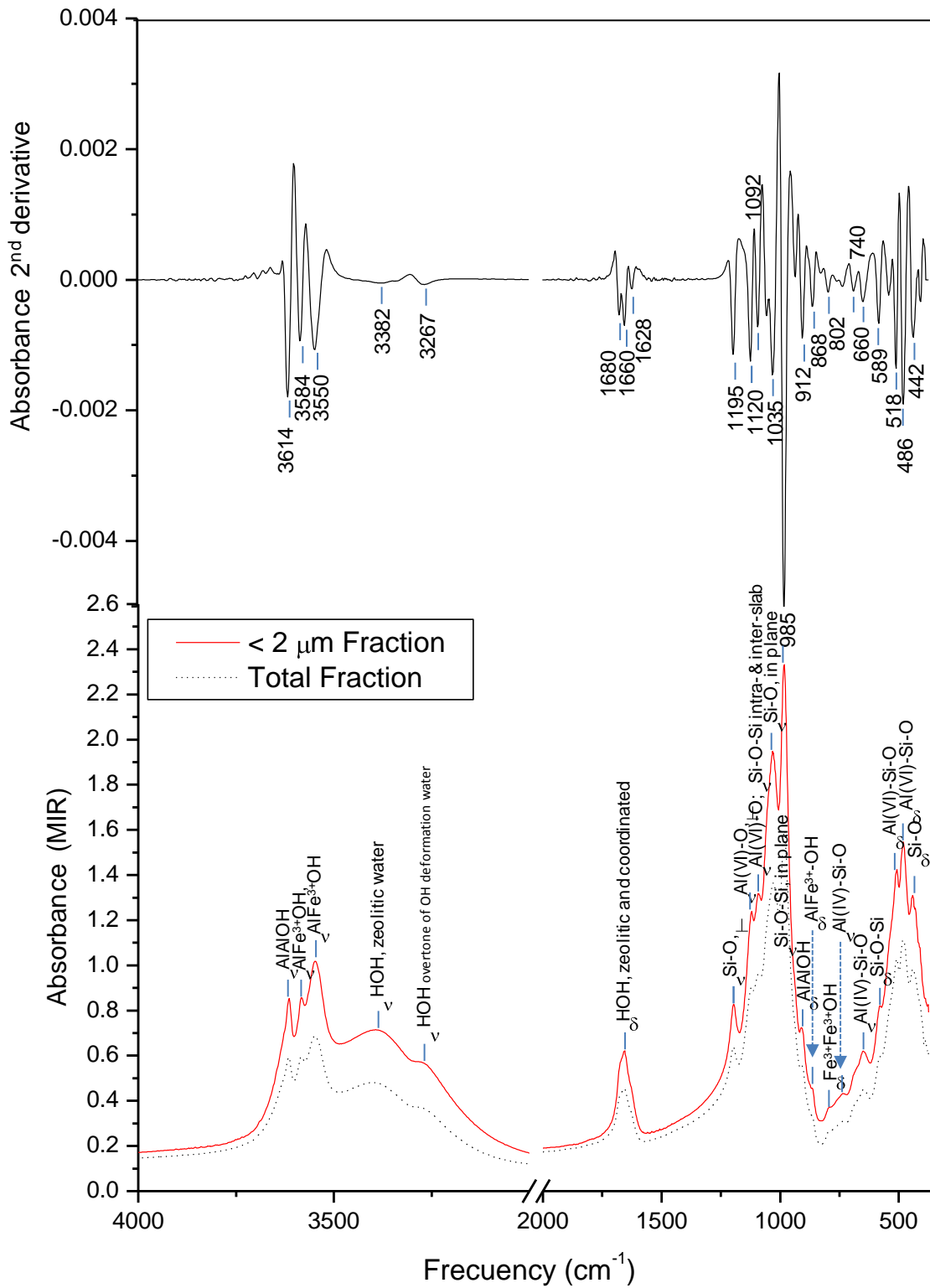


Figure 23. MIR spectra of the palygorskite from Torrejón el Rubio (Cáceres) and its second derivative calculated with the Savitzky-Golay algorithm with 15-point smoothing

4.7 Crystal unit cell structural DFT simulations and X-Ray powder patterns analysis

The unit cell parameters calculated values compare well with the experimentally estimated values as it is shown in Table 7. This good agreement is due to the fact that the interaction is dominated by the electrostatics forces. DFT predicts these structures with reasonable accuracy as shown, for example, in Sainz-Díaz et al., 2002; Timón et al., 2003; Ortega-Castro et al., 2010 and Fernández et al., 1999.

According to the calculations (Figure 24), the palygorskite clay mineral has a layer structure where two types of water molecules (coordinated and zeolitic) inside the channels are distinguished, following the structure proposed by (Bradley, 1940). The model calculations with 8 water molecules per unit cell, P_{w8} and FeP_{w8} , does not agree with the Bradley's model because only four water molecules are coordinated with Mg or MgFe atoms in the models P_{w8} or FeP_{w8} , respectively. The OH_2 is part of the coordination unit around the M3 site along the edges of the octahedral strips, to a distance $d(O_w...Mg)$ around 2.10 Å, far from what is described in literature (Giustetto and Chiari, 2004). This is corrected in the more accurate model, the Mg_2P_{w16} model, which use 16 water molecules, where eight water molecules are coordinate water and the remaining eight water molecules zeolitic water. The presence of zeolitic water promotes an increase the volume of the unit cell respect to models with not zeolitic up to a value of 1200 Å³. This molecular reorganization can be seen in Figure 25. As was described by Giusetto and Chiary (2004), the zeolitic water molecules are situated in the middle of the channels of palygorskite structure (Figure 25). In this case, water oxygen do not interact with basal oxygens because they form a hydrogen bond network of water molecules with distances $d(O_{zw}...O_{zw})$ of 2.9 Å, while between adjacent oxygens of coordinated water $d(O_{cw}...O_{cw})$ is of 2.7. This indicates a weaker absorption of zeolitic water than the coordinate one.

The presence of one structural Al^{3+} inside the octahedral layer substituting the Mg^{2+} atoms to a distance $d(Al..Mg)$ of around 2.87 Å, seems to weaken the water-octahedral oxygen interaction. Aluminium (III) isomorphous substitution by iron (III) promote a decrease in size of unit cell, behaviour that was observed and reported previously in 2:1 dioctahedral phyllosilicates (Sainz-Díaz et al., 2002).

The presence of iron inside the structure promote a serious cell distorsion, which is attributable to the highly distorted nature of Fe^{3+} octahedral as well as happened in similar structures such us ferripyrophyllite (Bickmore et al., 2003).

The presence of an excess of silica on the sample, promote an increase in the crystal size (Table 7) together with a distorting of the crystal morphology. In palygorskite the Si atom distance to the nearest oxygens are 2.31 Å and 3.55 Å. The Si atom prefers to be near the two OH clay

hydroxyl groups to a distance $d(\text{Si}\dots\text{O}_{\text{hydroxyl}})$ of 2.29 Å and 2.56 Å than near the water molecules $d(\text{Si}\dots\text{O}_{\text{water}})$ at 3.25 Å.

The role of water is essential in clays. So we have studied our mineral taking in account that it can contain from nothing to a maximum of 16 water molecules per unit cell. In these systems the role of the Mg ions restricted to the outer sites where they bond to crystalline H₂O as it described by Gionis et al. (2006), and clearly is in concordance with our theoretical model. A theoretical detailed study with bigger super-cells should be necessary in future works.

The crystal structure results were compared with the data obtained from the XRD analysis. The results between the experimental and theoretical results, described in Table 7, Table 8 and Figure 26, are in good agreement. The main reflection $d(110)$ is 10.43 Å in the experimental XRD pattern, whereas the value in theoretical model containing 16 H₂O molecules d_{hkl} is 10.53 Å. These values are far away from the model with 8 water molecules, P_{w8} and FeP_{w8}, which gave d_{hkl} values of 10.27 and 10.31 Å, respectively. Due the the higher narrowness of these principal peaks it can be ensure the crystallinity degree of the sample. Data that was corroborated with the grain size data of 20 nm that was obtained by fitting the X-ray diffraction profile by using the Warren-Averbach method.

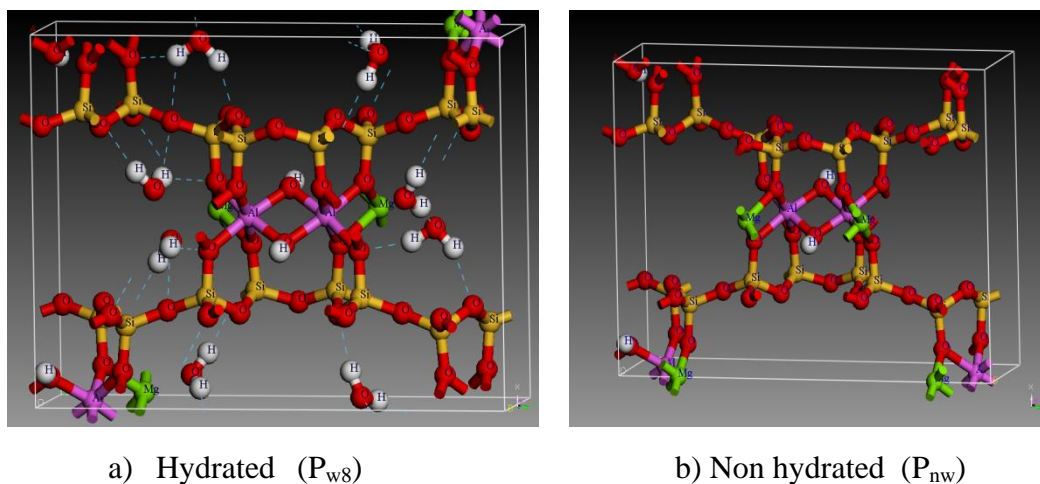


Figure 24. Atomic hydrated and non-hydrated palygorskite optimized structure

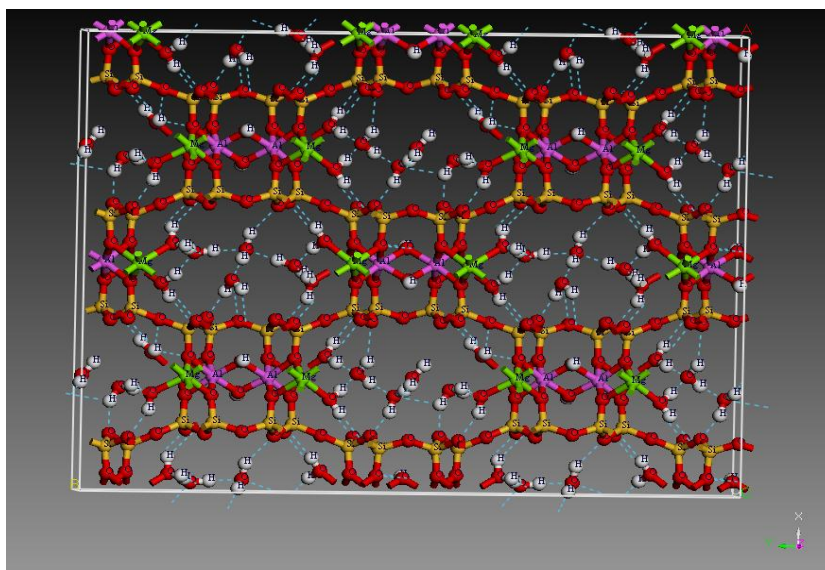


Figure 25. Atomic hydrated Pw16 palygorskite optimized structure. A 2x2 supercell it is shown for clarity

Table 7. Theoretical crystal parameters for all the hydrated and non-hydrated palygorskite systems analysed

Sample	a (Å)	b (Å)	c (Å)	α (°)	β (°)	γ (°)	Volume (cm ³)	Name
P_{nw}	12.77	17.32	5.15	89.9	90.1	89.9	1139.1	Palygorskite No water
Mg P_{w8}	12.80	17.34	5.15	89.8	89.9	90.3	1143.1	Palygorskite 8 Water
Mg₂Pw₁₆	13.16	17.63	5.20	89.6	89.5	89.9	1208.9	Palygorskite 16 Water
MgFe₁Pw₁₆	13.80	17.40	5.16	89.8	87.8	89.6	1238.6	
P_{expt}⁽¹⁾	12.78	17.83	5.24	90.0	95.8	90.0	1189.9	Experimental
P_{expt}⁽²⁾	12.67	17.85	5.24	90.0	90.0	90.0	1185.1	

⁽¹⁾ Bradley (1940); ⁽²⁾ Giustetto and Chiari (2004)

Table 8. Comparison of the theoretical and experimental intensities in each hkl atomic planes (in Å)

Indices d_{hkl}	d_{hkl} experimental	d_{hkl} Model P_{w8}	d_{hkl} Model FeP_{w8}	d_{hkl} Model P_{w16}	Visually* Estimated Intensities
110	10.57	10.27	10.31	10.53	ss
200	6.35	6.40	6.44	6.66	m
040	4.47	4.33	4.32	4.31	ms
130	5.43	5.26	5.25	5.27	m
121	4.25	4.18	4.20	4.19	ms
310	4.15	4.14	4.16	4.30	w
221	3.66	3.64	3.65	3.68	ms
150	3.43	3.34	3.34	3.34	vw
231	3.34	3.30	3.30	3.32	w
400	3.17	3.20	3.22	3.33	w
321	3.10	3.07	3.08	3.13	ms

* ss:very strong, s:strong, ms:medium strong, m:medium, w:weak, vw:very weak

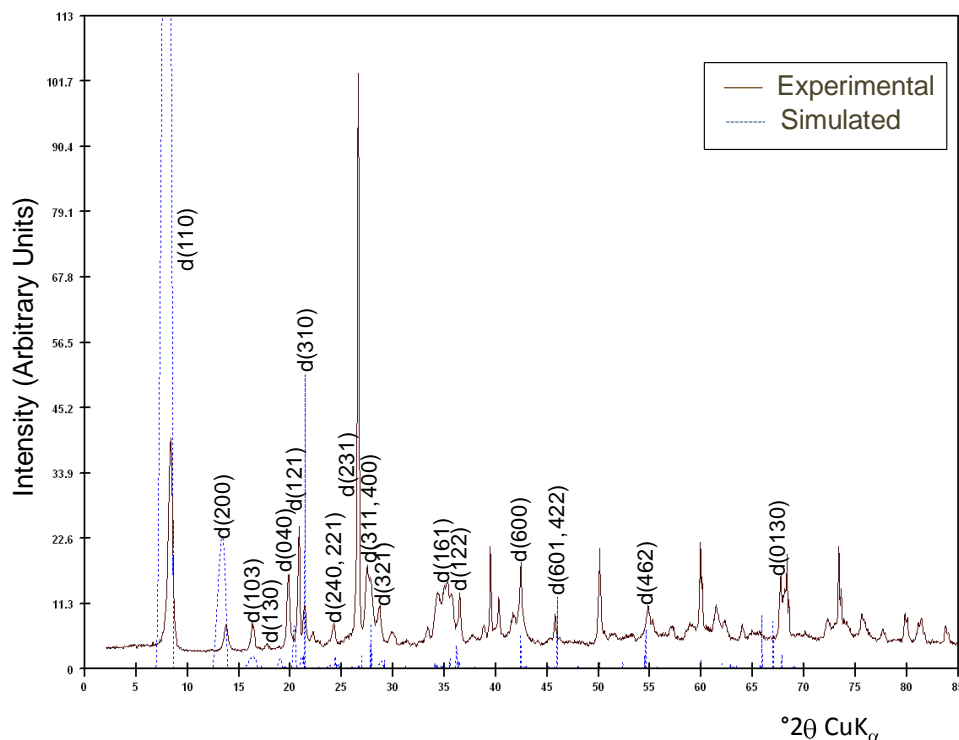


Figure 26. X-ray diffraction patterns of palygorskite total fraction sample from Torrejón el Rubio (Cáceres) and the simulated one

4.8 Infrared spectra: Theoretical analysis of the vibrational modes

Experimental and theoretically calculated absorption IR spectra of the palygorskite clay are assigned in Table 9. According to Figure 27 the experimental and theoretical spectra exhibit many similarities. The assignment being consistent with the accuracy range observed in previous DFT calculations of the vibrational spectrum of hydrous phyllosilicates, which is typically better than 1% for the frequency and 10% for the intensity (e.g., Balan et al. 2005).

The theoretic results were compared in the three frequency ranges of spectral activity discerned in the spectra ($3700\text{-}3000\text{ cm}^{-1}$, $1700\text{-}1500\text{ cm}^{-1}$ and $1300\text{-}400\text{ cm}^{-1}$). The region between $3700\text{-}3000\text{ cm}^{-1}$, attributed to the stretching OH vibrations of H_2O and structural hydroxyls and to the ν_2 bending modes of the various types of H_2O , appear clearly in the theoretical spectra where it is possible to assign it with accuracy. The strong peak at 3611 cm^{-1} corresponding to the $\nu(\text{Al-OH-Al})$ vibration, was obtained in the theoretical spectra at 3683 cm^{-1} in model with no water P_{nw} , decreasing to a value of 3665 cm^{-1} in the model $P_{\text{w}16}$, where the amount of water increases. A weaker peak at 3582 cm^{-1} corresponds to the $\nu(\text{Mg-OH-Fe})$ vibration, showing a similar behavior when the $\text{Fe}P_{\text{w}8}$ theoretical model was used, which gave a value of 3593 cm^{-1} . In this zone the last mid broad and strong peak at 3547 cm^{-1} corresponds to the $\nu(\text{Fe-OH-Fe})$ vibrations (Gionis et al., 2006). The broad experimental peak at around 3393 cm^{-1} is due to the adsorbed and zeolitic water. However, according to the theoretical model the higher frequency corresponds to zeolitic water whereas the lower one to the adsorbed water. As show in Table 9 and Figure 27 four zeolitic water OH-stretching bands are assigned around 3190 cm^{-1} , narrow and prominent bands that are strongly influenced by the surrounding waters. Therefore, the difference with respect that measured it is due the hydrogen bond network created by these waters that are not the same as show in Figure 24.

In the second zone, the bands at ca. 1196 and 650 cm^{-1} were attributed to the asymmetric and symmetric stretching of the Si-O-Si bridges linking the aluminosilicate slabs of palygorskite, as it was described by Tarte et al. (1973). Here the model values differ of that obtained by Gionis et al. (2006). This large frequency difference may be due to large value of this Si-O-Si angle (Chiari et al., 2003; Giustetto and Chiari, 2004), that in model $P_{\text{w}16}$ reach a value up to 156.7° . This value may be related to the distortion in these minerals due the thickening effect on the tetrahedral determined by the $\text{O}_{\text{basal}}\text{-T-O}_{\text{apical}}$ bond angle (τ). In illite and smectite models this calculated parameter is around 111° (Sainz-Díaz et al., 2002). For palygorskite, the $P_{\text{w}16}$ model gave values around 115° .

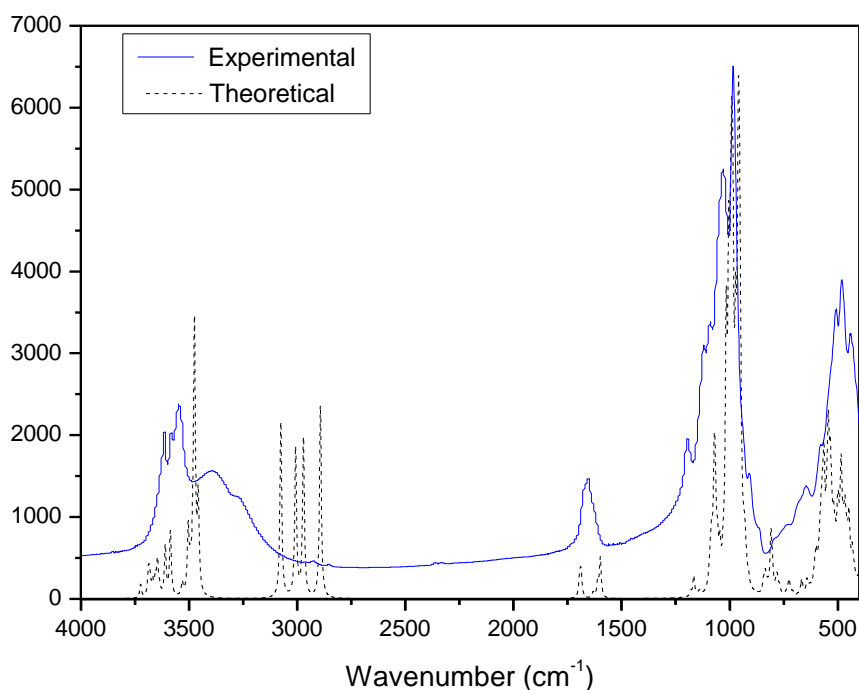


Figure 27. Comparison of the mid-infrared experimental spectra of the palygorskite from Torrejón el Rubio (Cáceres) with the simulated one

In the experimental spectra, a broad and a sharp peak at 1655 cm^{-1} corresponds to the OH deformation of water. The model P_{w16} shows $\delta\text{H}_2\text{O}$ vibration interacting with SiOH at 1688 cm^{-1} and 1684 cm^{-1} , physico-sorbed at 1661 cm^{-1} , coordinated at 1622 cm^{-1} , the zeolitic water having a lower value of 1603 cm^{-1} .

Stretching (between 1200 and 700 cm^{-1}) vibrations of the lattice show a mid intense band at 1120 cm^{-1} that correspond to $\nu(\text{Si-O})$ in plane [112], as well as a broad $\nu(\text{Si-O-Si})$ band at 1031 cm^{-1} . Pronounced and narrow band at 983 cm^{-1} can be also attributed to a Si-O stretching vibration. The weak peak at 797 cm^{-1} is difficult to assign, which can be related to a $\delta(\text{Fe}_2^{3+}\text{OH})$ vibration or to quartz impurity (Farmer and Russel, 1964). The defined AlAlOH deformation band at 911 cm^{-1} (927 cm^{-1} in the model P_{w16}) together with a slight AlMgOH inflexion at 859 cm^{-1} reflect the dominant dioctahedral character of the palygorskite as described by Madejova and Komadel (2001).

Table 9. Summary of the theoretical and experimental mid-infrared assignments

Experimental (cm^{-1})	Model $\text{P}_{\text{w}8}$	Model $\text{MgFe}_1\text{P}_{\text{w}16}$	Model $\text{Mg}_2\text{P}_{\text{w}16}$	Assignment
3681	≈ 3679	≈ 3642	≈ 3690	ν OH
3611	≈ 3650	$\approx 3652/68$	$\approx 3655/70$	ν Al_2OH
-	-	$\approx 3520/52$	$\approx 3520/40$	ν Mg_2OH
3584	-	3593	-	ν $\text{AlFe}^{3+}\text{OH}$
3547	-	-	-	ν $\text{Fe}^{3+}\text{Fe}^{3+}\text{OH}$
3393	≈ 3439	≈ 3427	≈ 3437	ν H_2O physisorbed
3261	-	≈ 3196	≈ 3194	ν H_2O zeolitic
1655	1684	-	-	δ H_2O interacting with SiOH
-	-	-	-	δ H_2O physisorbed
-	-	≈ 1650	≈ 1650	δ H_2O coordinated and zeolitic
-	-	-	-	δ $\text{H}_b\text{-OH}_a$, coordinated
1196	1145	-	-	ν Si-O \perp
1120	1072	1147	1139	ν Al(VI)-O, \perp
1092	-	-	-	ν Al(VI)-O, ν Si-O-Si
1035	1010	1016	1028	ν Si-O, in plane
985	-	-	-	ν Si-O-Si, in plane
911	910	912	916	δ Al_2OH
859	-	-	-	δ AlFeOH
797	811	-	-	δ $\text{SiO}_{\text{quartz}}$
740	-	-	-	ν Al(IV)-Si-O
660	662	-	-	ν Al(IV)-Si-O, ν Si-O-Si
589	586	589	591	δ Si-O-Si
518	509	-	-	δ Al(VI)-Si-O
486	-	-	-	δ Al(VI)-Si-O
442	-	455	456	δ Si-O

5 Conclusions

Palygorskites are of interest since decades because of their sorptive, optical, colloidal-rheological and catalytic physico-chemical properties which are based on the fabric, large surface area, microporosity, crystal morphology, fibrous structure and composition; more than 100 commercial uses being known nowadays (Galán and Singer, 2012).

In the characterization of palygorskites a lot of methods have been used but the combination of both theoretical and experimental techniques are still in an initial stage. In this work, a combination of experimental techniques (XRD, FRX, FTIR, TG-DSC, SEM and chemical analyses) and local geometry optimization by means of the Density Functional Theory (DFT) were used to characterize the palygorskite from Torrejón el Rubio (Serradilla, Cáceres).

This palygorskite is mainly composed by palygorskite (57 wt.%), muscovite/illite (2 wt.%), chlorite (1 wt.%), quartz (26 wt.%), K-feldspar (12 wt.%), cristobalite (1 wt.%), barite (1 wt.%) and traces of ilmenite.

The crystal chemistry formula of this palygorskite per half unit cell formula in its dehydrated has been determined on the basis of 21 oxygens as: $(\text{Mg}_{2.00}\text{Al}_{1.57}\text{Fe}^{3+}_{0.39}\text{Ti}_{0.04}\square_1)(\text{Si}_{7.90}\text{Al}_{0.10})\text{K}_{0.14}\text{O}_{21}$; and for its hydrated state, taking into account the different types of water as: $(\text{Mg}_{2.00}\text{Al}_{1.60}\text{Fe}^{3+}_{0.30}\text{Fe}^{2+}_{0.05}\text{Ti}_{0.05}\square_1)(\text{Si}_{7.90}\text{Al}_{0.10})\text{K}_{0.10}\text{O}_{20}(\text{OH})_2(\text{OH}_2)_4 \cdot 1.69 \text{H}_2\text{O}$. According to this chemical formula calculations, Mg^{2+} atoms at octahedral sites are substituted by Al, Fe and Ti; and silica at tetrahedral sheets is substituted by $^{\text{IV}}\text{Al}$. Although the experimental CEC was of 7 meq/100g, it was analysed that the excess of negative charge on both sheets can be compensated by K, Ca and Na interlayer cations with an interlayer charge variation from +0.05 to +0.14 e/hfuc, which correspond to a CEC between 7 and 20 meq/100g depending on the average tetrahedral substitutions.

This palygorskite has a pronounced dioctahedral character and can be defined as a Type II common palygorskite with a high amount of Fe (although the Fe content is much lower than the Al content). The R^3/R^2 ratio is around 1.01 (Al/Mg ratio of 0.83). This dioctahedral character was confirmed by FTIR by analyzing the vibrations of structural hydroxyl groups both in the MIR and NIR ranges, where only well-resolved bands of AlAlOH, FeFeOH and AlFeOH were observed. No signals of Mg_3OH and Si-OH (silanol groups), characteristics of a trioctahedral character and of broken edge surfaces at tetrahedral sheets, respectively, were found in the spectra. For the five octahedral positions per p.h.u.c., one octahedral site is vacant and 1.56-1.60 is occupied by $^{\text{VI}}\text{Al}$. Inside the octahedral sheet, the inner M1 sites are occupied by vacants, whereas the M2 sites are occupied at 98% by trivalent cations (78.5% Al^{3+} and 19.5% Fe^{3+}) and at 2.0% by tetravalent cations Ti^{4+} , all of them linked to structural 2.0 structural hydroxyls. The

two remaining Mg^{2+} by hfuc occupy edge M3 sites and are coordinated to 2.0 molecules of OH_2 . Channels of this palygorskite are deficient in zeolitic H_2O since they contain only 1.69 water molecules.

The different types of water in the palygorskite were determined by means TG-DSC tests. These curves show that there are three types of water: held physically water adsorbed on the surface (physisorbed) and inside the channels (zeolitic water), coordinated water associated to Mg^{2+} octahedral cations at M3 sites and hydroxyl water associated to octahedral cations at M2 sites. Zeolitic water is lost up to 114°C and the hydroxyl water at M2 sites is lost between 468 and 568°C . The coordinated water at M3 sites is liberated in two different stages: one half of coordinated water is lost between 114 to 235°C and the second half of coordinated water between 235 - 468°C , this latter water being vanished slower due to the hindrance of the folded channels on the diffusion process. 0.3 water molecules are lost between 600 to 900°C due to the elimination of water from Si-OH generated during the thermal treatment in the TG-DSC test. This means that there is a deficit of zeolitic water with respect to that expected for an ideal structure of palygorskite. However, the amount of water molecules for the other types of water is that expected for an ideal structure.

The microstructural and textural properties of the palygorskite were also determined by SEM and water and nitrogen adsorption isotherms. Palygorskite samples show a fibrous morphology (SEM analysis) with a variable size ranging from 1 to $10\ \mu\text{m}$ length and 10 to $250\ \text{nm}$ thick, fibers occurring as bundles of rods or as aggregates displaying a bird-nest texture with meso- and macropores. The total surface area of this palygorskite obtained by water adsorption tests is around $250\ \text{m}^2/\text{g}$, whereas a value of $350\ \text{m}^2/\text{g}$ were obtained by nitrogen adsorption/desorption isotherms using the microporous Tarazona NLDFT model. The study of the lowest relative pressures (microporous range) was necessary to analyse the adsorption properties of the crystallographic structure and inside the channels of the palygorskites, which could not be obtained by using the convectional BJH method. The interpretation of the nitrogen adsorption/desorption tests by using Tarazona and Infinite slit NLDFT models allowed to describe the complete pore size distribution in palygorskite. The palygorskite porosity can be divided in a structural or intracrystalline microporosity and a textural porosity (micro-, meso- and macro-porosity). There are two types of microporosity: structural or intracrystalline microporosity due to the staggered arrangement of talc ribbons in the fibers (with a pore width of $5.2\ \text{\AA}$); and an interfiber microporosity (with a pore width of $11.6\ \text{\AA}$). The textural porosity of this fibrous material is composed by an interfiber microporosity, mesoporosity and macroporosity (calculated from BJH and DFT methods). The mesoporosity due to interfiber mesopores or to the defect in the arrangement of the structural units, is mainly characterized by pores with a pore size of $292\ \text{\AA}$. A low amount of macropores were also detected with a pore

size of 500-582 Å and 1175 Å. The main surface area (around 212 m²/g) is developed in the structural or intracrystalline microporosity, which was determined from the microporous Tarazona NLDFT model. The external specific surface area developed on surfaces and edges (textural porosity) is around 77-104 m²/g.

The data were used to simulate the crystalline structure, calculating the local geometry optimization by means of the Density Functional Theory (DFT) in the Local Density Approximation (LDA) using the gradient corrected LDA developed by Perdew and Wang (GGA). The preliminary simulated structure was compared with the experimental DRX and FTIR spectra and a good agreement was obtained. Modifications on the structure considering a higher amount of unit cells (supercells) and elemental atom changes (Si, Mg, Al, Fe³⁺, Fe²⁺, Ti, etc.) in the octahedral sites should be considered in future works to analyse the most energetic stable configurations. In any case, this study demonstrates the applicability of the mixed theoretical-experimental work to characterize and understand the properties of clay minerals used in technological applications and environmental remediation.

6 Acknowledgments

We gratefully acknowledge support of Prof. Daniel Martín to use the X Powder software and of the Chemical Department from Ciemat. The BET analyses were performed in the Petrophysics Laboratory at CIEMAT. The XRF analyses were performed at CITIUS (Sevilla). Thanks to Prof. Juan Miguel Barrigón Morillas from the University of Extremadura fruitful discussions. This research was supported by the CSIC, UEX, CIEMAT and INTROMAC institute in a research fellowship of the main author during the academic year 2011-2012 in the University of Extremadura (Cáceres, Spain). Thanks also to TOLSA S.A. for providing the clay samples from the deposit.

7 References

- Alvarado, M., Russell, Jr., Chianelli, C., Arrowood, R.M., 2012. Computational study of the structure of a sepiolite/thioindigo mayan pigment. *Bioinorganic Chemistry and Applications* 2012, 1-6.
- Álvarez, A., Santarén, J., Esteban-Cubillo, A., Aparicio, P., 2011. Current industrial applications of palygorskite and sepiolite. In: *Developments in Palygorskite-Sepiolite research. A new outlook on these nanomaterials*. Galán, E. and Singer, A. (Eds). *Developments in Clay Science* 3, 281-298.
- Alvarez-Estrada, D., Sanchez Conde, C., 1967. Estudio y caracterización de una atapulgita. *Boletín de la Sociedad Española de Cerámica (Ciencia y Técnica)*, 6, 717-730.
- Amman, L., Bergaya, F., Lagaly, G. 2005. Determination of the cation exchange capacity of clays with copper complexes revisited. *Clay Minerals* 40, 441-453.
- Ahlich, J.L., Serna, C., Serratos, J.M., 1975. Structural hydroxyls in sepiolites. *Clay and Clay minerals* 23, 119-124.
- Artoli, G., Galli, E., Burattini, E., Cappuccio, G., and Simeoni, S., 1994. Palygorskite from Bolca, Italy: A characterization by high-resolution synchrotron radiation powder diffraction and computer modeling. *Neues Jahrbuch für Mineralogie Monshaft*, 271–229.
- Bailey, S.W., 1980. Structures of layer silicates. In: *Crystal structures of clay minerals and their X-ray identification*. Brindley (G.W.) and Brown, G. (Eds.). Mineralogical Society, London, 2-123.
- Bailey, S.W., Brindley, G.W., Johns, W.D., Martin, R.T., Ross, M., 1971. Summary of National and International Recommendations on Clay Mineral Nomenclature, 1969-1979. CMS Nomenclature Committee. *Clays and Clay Minerals*, 19, 129-132.
- Balan, E., Lazzeri, M., Saitta, A.M., Allard, T., Fuchs, Y., and Mauri, F. (2005) First-principles study of OH stretching modes in kaolinite, dickite and nacrite. *American Mineralogist*, 90, 50.60.
- Baroni, S., de Gironcoli, S., Dal Corso, A., Giannozzi, P., 2001. Phonons and related crystal properties from density-functional perturbation theory. *Reviews of Modern Physics* 73, 515-562.
- Barrer, R.M., Mackenzie, N., 1954. Sorption by atapulgite. I. Availability of intracrystalline channels. *Journal of Physical Chemistry* 58, 560-568.
- Barrett, E.P., Joyner, L.G., Halenda, P.P., 1951. The determination of pore volume and area distributions in porous substances. I. Computations from nitrogen isotherms, *J. Am. Chem. Soc.*, 73, 373–380.
- Bayram, H., Önal, M., Üstünişik, G., Sarikaya, Y., 2007. Some thermal characteristics of a mineral mixture of palygorskite, methalloysite, magnesite and dolomite. *Journal of Thermal Analysis and Calorimetry* 89, 169-174.
- Blanco, C., González, F., Pesquera, C., Benito, I., Medioroz, S., Pajares, J.A., 1989. Differences between one aluminic palygorskite and another magnesian by infrared spectroscopy. *Spectroscopy Letters* 22, 659-673.
- Bradley, W. F., 1940. The structural scheme of atapulgite. *American Mineralogist* 25, 405-410.
- Bickmore, B. R., Rosso, K.M., Nagy, K.L., Cygan, R., Tadanier, C., 2003. Ab initio determination of edge surface structures for dioctahedral 2:1 phyllosilicates: Implications for acid-base reactivity. *Clays and Clay Minerals* 51, 359-371.

- Brigatti, M.F., Galán, E., Theng, B.K.G., 2006. Structures and mineralogy of clay minerals. In: Handbook of Clay Science. Bergaya, F., Theng, B.K.G., Lagaly, G. Developments in Clay Science 1, 19-86.
- Brunauer, S., Emmet, P.H., Teller, E., 1936. Adsorption of gases in multimolecular layers. *Journal of the American Chemical Society* 60, 309–319.
- Cases, J.M., Grillet, Y., Francois, M., Michot, L., Villieras, F., Yvon, J., 1991. Evolution of the porous structure and surface area of palygorskite under vacuum thermal treatment. *Clays and Clay Minerals* 39, 191-201.
- Chahi, A., Petit, S. and Decarreau, A., 2002. Infrared evidence of dioctahedral-trioctahedral site occupancy in palygorskite. *Clays and Clay Minerals*, 50, 306-313.
- Chiari, G., Giustetto, R. Ricchiardi, G., 2003. Crystal structure refinements of palygorskite and Maya Blue form molecular modeling and powder synchrotron diffraction. *European Journal of Mineralogy*, 15, 21-33.
- Chisholm, J.E., 1992. Powder diffraction patterns and structural models for palygorskite. *Canadian Mineralogist*, 30, 61–73.
- Christ, C.L., Hathaway, J.C., Hostetler, P.B., and Shepard, A.O., 1969. Palygorskite: New X-ray data. *American Mineralogist*, 54, 198–205.
- Chryssikos, G.D., Gionis, V., Kacandes, G.H., Stathopoulou, E.T., Suárez, M., García-Romero, E., Sánchez del Río, M. , 2009. Octahedral cation analysis of palygorskite by near-infrared spectroscopy. *American Mineralogist* 94, 200–203.
- Clark, S. J., Segall, M.D., Pickard, C.J., Hasnip, P.J., Probert, M.I.J., Refson, K., Payne, M.C., 2005. First principles methods using CASTEP." *Zeitschrift fur Kristallographie* 220, 567-570.
- de Boer, J.H., Lippens, B.C., Linesen, B.G., Brokhoff, J.C.P., Van der Heuvel, A., Osinga., J., 1966. The t-curve of multimolecular N₂ adsorption. *J. Colloid Interface Sci.*, 21, pp. 405-414.
- De Lapparent, J., 1935. Sur un constituant essentiel des terres à foulon. *C.R.* 201, 481-483.
- Doménech, A., Doménech-Carbo, M.T., Sánchez del Río, M., Vázquez de Agredos Pascual, M.L., Lima, E., 2009. Maya Blue as a nanostructured polyfunctional hybrid organic-inorganic material: the need to change paradigms. *New Journal of Chemistry* 33, 2371-2379.
- Drifts, V.A., Sokolova, G.V., 1971. Structure of palygorskite. *Soviet Phys. Crystallogr.* 16, 183-185.
- Farmer, V. C., Russell J. D., 1964. The infra-red spectra of layer silicates. *Spectrochimica Acta* 20, 1149-1173.
- Farmer, V.C., 1974. *The Infrared Spectra of Minerals. Monograph 4.* Mineralogical Society, London, 539 pp.
- Fernández Alvarez, T., 1978. Efecto de la deshidratación sobre las propiedades adsorbentes de la palygorskita. *Clay Minerals* 13, 325-335.
- Fernández Macarro, B., Blanco, J.A., 1990. The palygorskite-containing Paleosols of the Talaván-Torrejón el Rubio (Cáceres, Spain). *Mineralogical and geochemical evolution. Chem. Geol.* 84, 54-57.
- Fernández, M.E., Ascencio, J.A., Mendoza-Anaya, D., Rodríguez Lugo, V., Jose-Yacaman, M., 1999. Experimental and theoretical studies of palygorskite clays. *Journal of Materials Science* 34, 5243-5255.
- Fersmann, A., 1913. Über die Palygorskitgruppe. *Bull. Acad. Imp. Sci., St. Petersburg* 2, 255.
- Friedel, G., 1901. Termietite et Lassalite. *Bull. Soc. Franc. Min.*, 24, 12-17.

- Friend, P.F., Dabrio, C.J., 1996. Tertiary basins of Spain. The stratigraphic record of crustal kinematics. *World and Regional Geology*. Cambridge University Press.
- Frost, R.L., Ding, Z., 2003. Controlled rate thermal analysis and differential scanning calorimetry of sepiolites and palygorskites. *Thermochimica Acta* 397, 119-128.
- Frost, R.L., Locos, O.B., Ruan, H., Klopogge, J.T., 2001. Near-infrared and mid-infrared spectroscopic study of sepiolites and palygorskites. *Vibrational Spectroscopy* 27, 1-13.
- Galán, E. 1996. Properties and applications of palygorskite-sepiolite clays. *Clay Miner.*, 31, 443-453.
- Galán, E., Singer, A., 2011. Developments in Palygorskite-Sepiolite Research. A new outlook on these nanomaterials. *Developments in Clay Science* 3. Elsevier, Amsterdam.
- Galán, R., Pozo, M., 2011. Palygorskite and sepiolite deposits in continental environments. Description, genetic patterns and sedimentary settings. In: *Developments in Palygorskite-Sepiolite research. A new outlook on these nanomaterials*. Galán, E. and Singer, A. (Eds). *Developments in Clay Science* 3, 125-173.
- Galán, E., Carretero, M.I., 1999. A new approach to compositional limits for sepiolite and palygorskite. *Clays and Clay Minerals*, 47, 399-409.
- Galán, E., Castillo, A., 1984. Sepiolite-Palygorskite in Spanish tertiary basins: genetic patterns in continental environments. In: Singer, A., Galán, E. (Eds.). *Palygorskite-Sepiolite. Occurrences, Genesis and Uses*. *Developments in Sedimentology* 37, 87-124. Elsevier, Amsterdam.
- Galán, E., Ferrero, J.M., la Iglesia, A., Robertson, R.H.S., 1975. The Cáceres palygorskite deposit, Spain. In: 1975. *International Clay Conference, Applied Publ.*, Mexico, 91-94.
- García-Romero, E., Suárez, M., 2010. On the chemical composition of sepiolite and palygorskite. *Clays and Clay Minerals* 58, 1-20.
- García-Romero, E., Suárez, M., Oyarzun, R., López-García, J.A., Regueiro, M., 2006. Fault-hosted palygorskite from the Serrata de Nijar Deformation Zone (SE Spain). *Clays and Clay Minerals* 54, 324-332.
- Gionis, V., Kacandes, G.H., Kastiris, I.D., Chryssikos, G.D., 2006. On the structure of palygorskite by mid- and near-infrared spectroscopy. *American Mineralogist* 91, 1125-1133.
- Gionis, V., Kacandes, G.H., Kastiris, I.D., Chryssikos, G.D., 2007. Combined near-infrared and X-ray diffraction investigation of the octahedral sheet composition of palygorskite. *Clays and Clay Minerals* 55, 543-553.
- Giustetto, R., Chiari, G., 2004. Crystal structure refinement of palygorskite from neutron powder diffraction. *European Journal of Mineralogy* 16, 521-532.
- Gregg, S. J., Sing, K.S.W., 1982. *Adsorption, Surface Area and Porosity*. Academic Press. 303 pp.
- Grillet, Y., Cases, J. M., Francois, M., Rouquerol, J., Poirier, J. E., 1988. Modification of the porous structure and surface area of sepiolite under vacuum thermal treatment. *Clays and Clay Minerals* 36, 233-242.
- Güven, N., Caillere, J.P.E., Fripiat, J.J., 1992. The coordination of aluminium ions in the palygorskite structure. *Clay and Clay Minerals*, 40, 457-461.
- Haden and Schwint, 1967. *Attapulgite. Its properties and applications*. *Industrial and Engineering Chemistry* 59, 59-69.
- Hammer, B., Hansen, L.B., Nørskov, J.K.N., 1999. Improved adsorption energetics within density-functional theory using revised Perdew-Burke-Ernzerhof functionals. *Physical Review B - Condensed Matter and Materials Physics* 59, 7413-7421.

- Hayashi, H., Otsuka, R., Imai, N., 1969. Infrared study of sepiolite and palygorskite on heating. *American Mineralogist* 53, 1969.
- Heddel, M.F., 1879. Pilolite. *Miner. Mag.*, 2, 206-219.
- Hirsiger, W., Müller-Vonmoos, M., Wiedemann, H.G., 1975. Thermal analysis of palygorskite. *Thermochim. Acta* 13, 223–230.
- Heller-Kallai, L., Rozenson, I., 1981. Mössbauer studies of palygorskite and some aspects of palygorskite mineralogy. *Clays and Clay Minerals* 29, 226-232.
- Huang, Y.-J., Li, Z., Li, S.-Z., Shi, Z.-L., Yin, L., Hsia, Y.-F., 2007. Mössbauer investigations of palygorskite from Xuyi, China. *Nucl. Instrum. Methods Phys. Res. Sect. B* 260, 657–662.
- Huertas, F., Linares, J., Martín Vivaldi, J.L., 1970. Clay minerals geochemistry in basic sedimentary environments. *Proceedings Reunión Hispano-Belga de Minerales de la Arcilla*, 211-214.
- Huggins, C.W., Denny, M.V., Shell, H.R., 1962. Properties of palygorskite, an asbestiform mineral. In: *United States Bureau of Mines, Report of Investigation, 6071*, pp. 1-17.
- Ispording, W.C., 1973. Discussion of the occurrence and origin of sedimentary palygorskite-sepiolite deposits. *Clay and Clay Minerals*, 21, 391-401.
- Jones, B.L., Galán, E., 1988. Sepiolite and palygorskite. In: *Hydrous Phyllosilicates (Exclusive of Micas)*, Bailey, S.W. (Ed.), *Reviews in Mineralogy* 19, Mineralogical Society of America, Washington, D.C., 631-674.
- Keeling, P., 1961. The examination of clays by IL/MA: *Transactions of the British Ceramic Society*, 60, pp. 217-224.
- Kiyohiro, T., Otsuka, R., 1989. Dehydration mechanism of bound water in sepiolite. *Thermochimica Acta* 147, 127-138.
- Krekeler, M.P.S., Guggenheim, 2008. Defects in microstructure in palygorskite-sepiolite minerals: a transmission electron microscopy (TEM) study. *Applied Clay Science* 39, 98-105.
- Kuang, W., Glenn, A.F., Detellier, C., 2004. Dehydration and rehydration of palygorskite and the influence of water on the nanopores. *Clays and Clay Minerals* 52, 635-642.
- Kulbicki, G., 1959. High temperature phases in sepiolite, attapulgite and saponite. *Am. Mineral.* 44, 752–764.
- Leguey, S., Martín de Vidales, J., Casas, J., 1984. Diagenetic palygorskite in marginal continental detrital deposits located in the South of the Tertiary Duero basin (Segovia). In *Singer and Galan (Eds.). Palygorskite-Sepiolite: occurrences, genesis and uses. Developments in Sedimentology*, 37. Elsevier, 149-156.
- López-Galindo, A., Viseras, C., Aguzzi, C., Cerezo, P., 2011. Pharmaceutical and cosmetic used of fibrous clays. In: *Developments in Palygorskite-Sepiolite research. A new outlook on these nanomaterials*. Galán, E. and Singer, A. (Eds). *Developments in Clay Science* 3, 299-324.
- Materials Studio Modeling, 2010. Accelerlys Software Inc., San Diego, CA.
- Madejová, J., Komadel, P., 2001. Baseline studies of the clay minerals society source clays: Infrared methods. *Clays and Clay Minerals* 49, 410-432.
- Martín Vivaldi, J.L., Fenoll Hach-Ali, F., 1970. Palygorskites and Sepiolites (Hormites). Chapter 20. In: *Differential Thermal Analysis. Volume 1, Chapter 20*, Mackenzie, R.C. (Ed.), 553-573 pp.
- Martín Vivaldi, J.L., Linares, J., 1962. A random intergrowth of sepiolite and attapulgite. *Clay and Clay Minerals* 9, 592-602.

- Martín Vivaldi, J.L., Cano-Ruiz, J., 1956. Contribution to the study of sepiolite: III. The dehydration process and the types of water molecules. *Clay and Clay Minerals* 4, 177-180.
- Mermut, A.R., Lagaly, G., 2001. Baseline studies of the clay minerals society source clays: layer-charge determination and characteristics of those minerals containing 2:1 layers. *Clay and Clay Minerals* 49, 393-397.
- Meunier, A., 2005. *Clays*. Springer-Verlag, New York, 472 pp.
- Mifsud, A., Rautureau, M., Fornes, V., 1978. Etude de l'eau dans la palygorskite à l'aide des analyses thermiques. *Clay Miner.* 13: 367-374.
- Millot, G., 1970. *Geology of Clays*: Springer-Verlag, Chapman and Hall, London, 429 pp.
- Moore, D., Reynolds, R., 1989. *X-Ray diffraction and the identification and analysis of Clay Minerals*. Oxford University Press, N.Y., 332 pp.
- Monkhorst, H. J., Pack, J. D., 1976. Special points for Brillouin-zone integrations. *Physical Review B* 13, 5188-5192.
- Mumpton, F. A. and Roy, R., 1956. New data on sepiolite and attapulgite: in *Clays and Clay Minerals, Proc. 5th Natl Conf.*, Urbana, Illinois, 1955, Ada Swineford, ed., Natl. Acad. Sci. Natl. Res. Council. Publ. 566, 136-143.
- Murray, H.H., 2006. *Applied Clay Mineralogy. Occurrences, Processing and Application of Kaolins, bentonites, Palygorskite-Sepiolite and Common Clays*. *Developments in Clay Science* 2, 180 pp.
- Murray, H.H., 2000. Traditional and new applications for kaolin, smectite, and palygorskite: a general overview. *Appl. Clay Sci.* 17, 207-221.
- Murray, H. H., 1991. Overview clay mineral applications. *Applied Clay Science* 5, 379 - 395.
- Murray, H.H., Pozo, M., Galán, E., 2011. An introduction to palygorskite and sepiolite deposits. Location, geology and uses. In: *Developments in Palygorskite-Sepiolite research. A new outlook on these nanomaterials*. Galán, E. and Singer, A. (Eds). *Developments in Clay Science* 3, 85-99.
- Neaman, A., Singer, A., 2011. The effects of palygorskite on chemical and physico-chemical properties of soils. In: *Developments in Palygorskite-Sepiolite research. A new outlook on these nanomaterials*. Galán, E. and Singer, A. (Eds). *Developments in Clay Science* 3, 325-349.
- Newman, A.C.D., Brown, G., 1987. The chemical constitution of clays. In: *Chemistry of Clays and Clay Minerals*, Newman, A.C.D. (Ed.). Mineralogical Society, London, 2-128.
- Ortega-Castro, J., Hernández-Haro, N., Timón, V., Sainz-Díaz, C.I., Hernández-Laguna, A., 2010. High-pressure behavior of 2M1 muscovite. *American Mineralogist* 95, 249-259.
- Post, J.E., Heaney, P., 2008. Synchrotron powder X-ray diffraction study of the structure and dehydration behavior of palygorskite. *American Mineralogist*, 93, 667-675.
- Preisinger, A., 1963. Sepiolite and related compounds: its stability and application. *Clays and Clay Minerals*, 10, 365-371.
- Prost, R., 1975. Infrared study of the interactions between the different kinds of water molecules present in sepiolite. *Spectrochim. Acta* 31A, 1497-1499.
- Rhouta, V., Zatile, E., Bouna, L., Lakbita, O., Maury, F., Daoudi, L., Lafont, M.C., Amjoud, M.B., Senocq, F., Jada, A., Aghzzaf, A., 2013. Comprehensive physico-chemical study of dioctahedral palygorskite-rich clay from Marrakech High Atlas (Morocco). *Phys. Chem. Minerals* 40, 411-424.

- Robertson, R.H.S., 1963. Perlite and palygorskite in Theophrastus. *Classical Rev.*, 13-132.
- Rodríguez, J. L., 2003. *Applied Study of Cultural Heritage and Clays*. CSIC publications, 587 pp.
- Ruiz-Hitzky, E., Aranda, P., Alvarez, A., Santaren, J., Esteban-Cubillo, A., 2011. Advanced materials and new applications of sepiolite and palygorskite. In: *Developments in Palygorskite-Sepiolite research. A new outlook on these nanomaterials*. Galán, E. and Singer, A. (Eds). *Developments in Clay Science* 3, 393-452.
- Sainz-Díaz, C. I., Timón, V., Botella, V., Artacho, E., Hernández-Laguna, A., 2002. Quantum mechanical calculations of dioctahedral 2:1 phyllosilicates: Effect of octahedral cation distributions in pyrophyllite, illite, and smectite. *American Mineralogist* 87, 958-965.
- Sánchez del Río, M., Doménech, A., Doménech-Carbo, M.T., Vázquez de Agredos Pascual, M.L., Suárez, M., García-Romero, E., 2011. The Maya Blue Pigment. 453-481.
- Sawhney, B. L. 1970. Potassium and cesium ion selectivity in relation to clay mineral microstructure. *Clays & Clay Minerals* 18, 47-52.
- Schultz, L.G., 1964. Quantitative interpretation of mineralogical composition from X-ray and chemical data for the Pierre Shale. U.S. Geological Survey Professional Paper 391-C, 1-31.
- Serna, C., van Scoyoc., G.E., Ahlrichs, J.L., 1977. Hydroxyl groups and water in palygorskite. *American Mineralogist*. 62, 784-792.
- Serna, C, Ahlrichs, J.L., Serratosa, J.M., 1975. Folding in sepiolite crystals. *Clay and Clay Minerals* 23, 452-457.
- Serna, C.J., VanScoyoc, G.E., 1979. Infrared study of sepiolite and palygorskite surfaces. In: *Proceedings of the International Clay Conference (Oxford, 1978)*. *Developments in Sedimentology*, 27, pp. 197-206. Elsevier, Amsterdam.
- Serratosa, J.M., 1979. Surface properties of fibrous clay minerals (palygorskite and sepiolite). In: *Proceedings of the International Clay Conference (Oxford, 1978)*. *Developments in Sedimentology*, 27, 99-109. Elsevier, Amsterdam.
- Singer, A., 1989. Palygorskite and sepiolite group minerals. In: *Minerals in soil environments*. Dixon, J.B., Week, S. B., (Eds.). Soil Science Society of America. Madison, 829-872.
- Singer, A., 1979. Palygorskite in sediments: detrital, diagenetic or neoformed. A critical review. *Geol. Rund.* 68, 996-1008.
- Singer, A., Norrish, K., 1974. Pedogenic palygorskite occurrences in Australia, *Am. Miner.* 59, 508-517.
- Stathopoulou, E.T., Suárez, M., García-Romero, E., Sánchez del Río, M., Kacandes, G.H., Gionis, V., Chryssikos, G.D. 2011. Trioctahedral entities in palygorskite: Near-infrared evidence for sepiolite-palygorskite polysomatism. *European Journal Mineralogy* 23, 567-576.
- Suárez, M., García-Romero, E., 2012. Variability of the surface properties of sepiolite. *Applied Clay Science* 67-68, 72-82.
- Suárez, M., García-Romero, 2011. Advances in the Crystal Chemistry of Sepiolite and Palygorskite. In: *Developments in Palygorskite-Sepiolite research. A new outlook on these nanomaterials*. Galán, E. and Singer, A. (Eds). *Developments in Clay Science* 3, 33-65.
- Suárez, M., García-Romero, E., Sánchez del Río, M., Matinetto, P., Dooryhée, E., 2007. The effect of the octahedral cations on the dimensions of the palygorskite cell. *Clay Minerals* 42, 287-297.
- Suárez, M., García-Romero, E., 2006. FTIR spectroscopic study of palygorskite: influence of the composition of the octahedral sheet. *Appl. Clay Sci.* 31, 154-163.

- Suárez Barrios, M., Flores González, L.V., Vicente Rodríguez, M.A., Martín Pozas, J.M., 1995. Acid activation of a palygorskite with HCl: development of physico-chemical, textural and surface properties. *Applied Clay Science* 10, 247-258.
- Tarte, P., Pottier, M.J., 1973. Vibrational studies of silicates and germanates-V. I.R. and Raman spectra of pyrosilicates and pyrogermanates with a linear bridge. *Spectrochimica Acta Part A: Molecular Spectroscopy* 29, 1017-1027.
- Timón, V., Sainz-Díaz, C., Botella, V., Hernández-Laguna, A., 2003. Isomorphous cation substitution in dioctahedral phyllosilicates by means of ab initio quantum mechanical calculations on clusters. *American Mineralogist* 88, 1788-1795.
- Torres-Ruíz, J., López-Galindo, González-López, J.M., Delgado, A., 1994. Geochemistry of Spanish sepiolite-palygorskite deposits: Genetic considerations based on trace elements and isotopes. *Chemical Geology*, 112, 221-245.
- Van Scoyoc, E.G., Serna, C., Ahlrichs, J.L., 1979. Structural changes in palygorskite during dehydration and dehydroxylation. *Am. Mineral.* 64, 215-223.
- Villamor, P., Capote, R., Tsige, 1996. Actividad neotectónica de la Falla de Alentejo-Plasencia en Extremadura (Macizo Hespérico). *Geogaceta* 20, 925-928.
- Von Ssaftschekow, T., 1862. Über palygorskite. *Verh. Russ. Kaiserl. Mineral. Ges., St. Petersburg*, 102-104.
- Van der Marel, H.W., Beutelspacher, H., 1976. Atlas of infrared spectroscopy of clay minerals and their admixtures. Elsevier, Amsterdam, 396 pp.
- Van Olphen, H., 1966. Maya blue: a clay mineral-organic pigment?. *Science*, 154, 645-646.
- Warren, B. E., Averbach, B. L., 1952. The separation of cold-work distortion and particle size broadening in x-ray patterns. *Journal of Applied Physics* 23, 497.
- Weaver, C.E., Pollard, L.D., 1973. The chemistry of clay minerals. *Dev. Sedimentology* 15. Elsevier, Sci. Publ. Co., Amsterdam, 213 pp.
- Weaver, C.E., Beck, K.C., 1977. Miocene of the S.E. Unites States: a model for chemical sedimentation in a per-marine environment. *Sediment Geology* 17, 1-234.
- Webb. P.A., Orr, C., 1997. Analytical methods in fine particle technology. Micromeritics instrument corporation, Norcross, USA, 301 pp.
- Woessner, D.E., 1989. Characterization of clay minerals by ²⁷Al nuclear resonance spectroscopy. *Amer. Mineral.* 74, 203-215.
- Yacamán, M.J., Rendon, J., Arenas, J., Puche, M.C.S., 1996. Maya blue paint: an ancient nanostructured material. *Science*, 273, 223-225.

